

THERMAL ANALYSIS OF A MONOPROPELLANT MICROPROPULSION
SYSTEM FOR A CUBESAT

A Thesis
presented to
the Faculty of California Polytechnic State University,
San Luis Obispo

In Partial Fulfillment
of the Requirements for the Degree
Master of Science Degree in Aerospace Engineering

by
Erin C. Stearns
August 2013

© 2013
Erin C. Stearns
ALL RIGHTS RESERVED

COMMITTEE MEMBERSHIP

TITLE: Thermal Analysis of a Monopropellant Micropropulsion System for a CubeSat

AUTHOR: Erin C. Stearns

DATE SUBMITTED: August 2013

COMMITTEE CHAIR: Dr. Kira Abercromby, Assistant Professor
Cal Poly Aerospace Engineering Department

COMMITTEE MEMBER: Dr. Jordi Puig-Suari, Professor
Cal Poly Aerospace Engineering Department

COMMITTEE MEMBER: Dr. Kim Shollenberger, Professor
Cal Poly Mechanical Engineering Department

COMMITTEE MEMBER: Chris Bidy, Vice President of Engineering
Stellar Exploration, Inc.

ABSTRACT

Thermal Analysis of a Monopropellant Micropropulsion System for a CubeSat Erin C. Stearns

Propulsive capabilities on a CubeSat are the next step in advancement in the Aerospace Industry. This is no longer a quest that is being sought by just university programs, but a challenge that is being taken on by all of the industry due to the low-cost missions that can be accomplished. At this time, all of the proposed micro-thruster systems still require some form of development or testing before being flight-ready. Stellar Exploration, Inc. is developing a monopropellant micropropulsion system designed specifically for CubeSat application.

The addition of a thruster to a CubeSat would expand the possibilities of what CubeSat missions are capable of achieving. The development of these miniature systems comes with many challenges. One of the largest challenges that a hot thruster faces is the ability to complete burns for the specified mission without transferring excessive heat into the propulsion tank. Due to the close proximity of the thruster to the tank, thermal standoff options are necessary to help alleviate the heat going through the system, especially while in a thermally extreme environment. This thesis examines the heat transfer that occurs within a CubeSat with an operating hydrazine monopropellant thruster.

Thermal analysis of the system revealed that having a solid stainless steel barrier between the thruster and tank led to increasing temperatures greater than 400K in the propellant tank while in an environment exposed to the sun. This creates a large amount of risk for the CubeSat and its mission. The use of a thermal insulating material or a hollow barrier for the standoff decreased the risk of using this system. This creates a standoff where the heat of the propellant reaction does not reach the propellant in the tank. Therefore, the maximum temperature that the tank reaches is equivalent to the temperature of the external environment while in extreme conditions. These results create the confidence that the thermal standoffs will function as intended to protect the spacecraft and its payload during flight.

Keywords: Micropropulsion, CubeSat, Thermal Analysis, Monopropellant, Hydrazine, FLUENT

ACKNOWLEDGMENTS

There are several people who I would like to acknowledge who have helped to guide me during this thesis process. First and most importantly I would like to thank my advisor, Dr. Kira Abercromby. This process has not been one that was easy for me in any way during this period in my life. Even though there were rough moments, she has always been there for me and motivated me to strive to accomplish better results. I see her as a strong role model who I look up to and her encouragement has driven me through some very tough times.

I would like to thank all of my committee members for putting the time and effort into assisting me when it was needed. I appreciate all of the support that each of you has given to me throughout this process. There were always moments where I was unsure of what direction to go in and you were there to guide me.

Lastly, I want to thank my family and close friends who have been there for me over the past couple years. You have all kept me going when obstacles seemed impossible and I will always be grateful for all of your love and support.

TABLE OF CONTENTS

LIST OF TABLES	ix
LIST OF FIGURES	x
NOMENCLATURE	xiv
1 - Introduction	1
1.1 – Motivation	1
1.2 – CubeSat Background.....	2
1.3 – Micropropulsion Systems.....	3
1.3.1 – Chemical Monopropellant Thrusters	3
1.3.2 – Cold Gas Thrusters	6
1.3.3 – Liquefied Gas Thrusters	7
1.3.4 – Solid Rocket Motors (SRMs)	9
1.3.5 – Bipropellant Thrusters	10
1.3.6 – Electric Propulsion	11
2 –System Configuration	18
2.1 – Thruster Unit Design.....	18
2.1.1 – Thermal Properties of Thruster Materials	20
2.1.2 – Thermal Properties of Propellant and Reaction.....	21
3 – Thermal Analysis	25
3.1 – Calculation Background.....	25
3.1.1 – Compressible vs. Incompressible Flow	25
3.1.2 – Steady State vs. Transient Flow	26
3.2 – Numerical Analysis Prediction.....	27
3.3 – Modeling in ANSYS FLUENT.....	27
3.3.1 – Continuity and Momentum Equations.....	28

3.3.2	– Modeling Compressible Flow	29
3.3.3	– Modeling Heat Transfer.....	29
4	– ANSYS ICEM and FLUENT Setup	32
4.1	– Modeling Low Earth Orbit (LEO) Environment.....	32
4.1.1	– High Vacuum.....	32
4.1.2	– Radiation.....	32
4.2	– ANSYS ICEM Mesh Setup.....	34
4.2.1	– General Problem Setup.....	34
4.3	– ANSYS Fluent Problem Setup.....	37
4.3.1	– General Problem Setup.....	37
5	– ANSYS Fluent Thermal Analysis 2-Dimensional Models.....	40
5.1	– Model 1: Two-Dimensional Simplified	40
5.1.1	– Modeling Assumptions.....	40
5.1.2	– Model Setup for the Simplified Case	40
5.2	– Model 2: Two-Dimensional Realistic	42
5.2.1	– Modeling Assumptions.....	42
5.2.2	– Model Setup.....	44
6	– Results.....	45
6.1	– Model 1: Simplified 2-D Model.....	45
6.1.1	– Model with Stainless Steel Barrier	45
6.1.2	– Model with “Air” Barrier	48
6.1.3	– Model with Alumina Silicate Barrier	49
6.2	– Model 2: Two-Dimensional Complex.....	51
6.2.1	– Model with Reaction in “Heat Source Plates”	51
6.2.2	– Model with Reaction in the Entirety of the Combustion Chamber	52

6.3	– Model 2: Recap of the overall results.....	69
6.4	– Validation of Results.....	71
7	– Conclusion.....	75
7.1	– Future Work.....	77
7.1.1	– Hot-fire Testing of the System.....	77
7.1.2	– Model the System through another Thermal Analysis Program.....	77
	Bibliography.....	78
APPENDICES		
A-	Full Table of Result Values.....	81
B-	ANSYS Input Values.....	83
C-	Stellar Exploration, Inc. Propulsion Module.....	86

LIST OF TABLES

Table	Page
Table 1. Hydrazine Micropropulsion Thruster Performance Comparisons (2).....	5
Table 2. Cold Gas Thruster Performance Comparison (2).	7
Table 3. Micro-PPT Performance Comparison (2).....	13
Table 4. Micro-Ion Engine Performance Comparison (2).....	15
Table 5. Colloid Thruster Performance Characteristics (2).....	17
Table 6. Hot fire test results of a hydrazine monopropellant thruster (9).....	24
Table 7. Simplified Model Results with Maximum Propellant Temperature.....	50
Table 8. Maximum Temperature Comparisons for a Solid Stainless Steel Barrier.....	59
Table 9. Maximum Temperature Comparisons for an Alumina Silicate Barrier.	64
Table 10. Maximum Temperature Comparisons for a Hollow Barrier.	69
Table 11. Overall Results of Burn Times Under Different Conditions.	70
Table 12. Comparison of Test Fire Data and Thermal Analysis Model.....	73
Table 13. Complete Thermal Analysis Results from 2-D Models.....	81
Table 14. Spacecraft Specifications.....	86
Table 15. Thruster Specifications.	86
Table 16. Projected Values for Thruster Performance.....	87

LIST OF FIGURES

Figure	Page
Figure 1. 1U CubeSat System (1).	2
Figure 2. JPL Hydrazine Milli-Newton Thrusters (HmNT) by Parker et al (2).	4
Figure 3. Miniature Hydrogen Peroxide Thruster by Scharlemann et al. (2)	5
Figure 4. VACCO MiPS CubeSat Integration (2).	8
Figure 5. Micromachined Silicon Solid Rocket Motors by Zhang et al. (2)	10
Figure 6. MIT Micro Bipropellant Engine Concept (2).	11
Figure 7. The "Dawgstar" PPT Thruster System (2).	12
Figure 8. (a) VAT Thruster Firing on the JPL Micro-Newton Thrust Stand. (b) VAT PPU Configured for CubeSat (2).	14
Figure 9. JPL Miniature Xenon Ion Thruster (MiXI) (2).	15
Figure 10. ST-7 Colloid Thruster Cluster (2).	17
Figure 11. Propulsion System Unit with Specified Dimensions (in inches).	18
Figure 12. 3U CubeSat Demonstrating Compartment Assignments (3).	19
Figure 13. CAD 3-D Model of Micropropulsion System by Stellar Exploration, Inc.	20
Figure 14. Aluminum 6061-T6 Tank and Lid (3).	21
Figure 15. Platinum/Iridium Catalyst (3).	22
Figure 16. Sample Geometry from ANSYS ICEM Showing Points and Curves.	35
Figure 17. Sample Geometry Taken from ANSYS ICEM Showing Surfaces.	36
Figure 18. Output from a Mesh Check for Quality.	37

Figure 19. ANSYS ICEM Mesh of the Simplified Model.	40
Figure 20. ANSYS ICEM Mesh of the Simplified Model in a Zoom View.	42
Figure 21. ANSYS ICEM Mesh of 2-Dimensional Model.....	43
Figure 22. Contours of Total Temperature with Stainless Steel Walls after 43 seconds of Burn Time. (in K)	46
Figure 23. Close view of Contours of Total Temperature with Stainless Steel Walls after 50 seconds of Burn Time (in K).....	47
Figure 24. Maximum Temperature Value of the Propellant in the Tank with Stainless Steel Walls. (in K)	48
Figure 25. Contours of Total Temperature with Air Barrier after 43 seconds of Burn Time. (in K)	49
Figure 26. Contours of Total Temperature with Alumina Silicate Walls after 43 seconds of Burn Time. (in K)	50
Figure 27. Contours of Total Temperature with Heat Plates after 40 seconds of Burn Time. (in K)	52
Figure 28. Contours of Total Temperature with Solid Stainless Steel Barrier after 43 seconds of Burn Time in a Hot Environment. (in K).....	53
Figure 29. Zoomed View of Contours of Total Temperature with Solid Stainless Steel Barrier after 43 seconds of Burn Time in a Hot Environment. (in K).....	54
Figure 30. Maximum Temperature of the Propellant throughout the Burn Time in a Hot Thermal Environment. (in K).....	55
Figure 31. Contours of Total Temperature with Solid Stainless Steel Barrier after 43 seconds of Burn Time in a Cold Thermal Environment. (in K)	56

Figure 32. Maximum Temperature of the Propellant throughout the Burn Time in a Cold Thermal Environment. (in K).....	56
Figure 33. Contours of Total Temperature with Solid Stainless Steel Barrier after 43 seconds of Burn Time in a Mid-range Thermal Environment. (in K).....	57
Figure 34. Maximum Temperature of the Propellant throughout the Burn Time in a Mid-range Thermal Environment. (in K).....	58
Figure 35. Contours of Total Temperature with Alumina Silicate Barrier after 43 seconds of Burn Time in a High Thermal Environment. (in K).....	60
Figure 36. Zoomed View of Contours of Total Temperature with Alumina Silicate Barrier after 43 seconds of Burn Time in a High Thermal Environment. (in K)	60
Figure 37. Maximum Temperature of the Propellant throughout the Burn Time in a High Thermal Environment. (in K).....	61
Figure 38. Contours of Total Temperature with Alumina Silicate Barrier after 43 seconds of Burn Time in a Low Thermal Environment. (in K).....	62
Figure 39. Maximum Temperature of the Propellant throughout the Burn Time in a Low Thermal Environment. (in K)	62
Figure 40. Contours of Total Temperature with Alumina Silicate Barrier after 43 seconds of Burn Time in a Mid-range Thermal Environment. (in K)	63
Figure 41. Contours of Total Temperature with Hollow Barrier after 43 seconds of Burn Time in a High Thermal Environment. (in K).....	65
Figure 42. Zoomed View of Contours of Total Temperature with Hollow Barrier after 43 seconds of Burn Time in a High Thermal Environment. (in K).....	65

Figure 43. Maximum Temperature of the Propellant throughout the Burn Time in a High Thermal Environment. (in K).....	66
Figure 44. Contours of Total Temperature with Hollow Barrier after 43 seconds of Burn Time in a Low Thermal Environment. (in K)	67
Figure 45. Maximum Temperature of the Propellant throughout the Burn Time in a Low Thermal Environment. (in K)	67
Figure 46. Contours of Total Temperature with Hollow Barrier after 43 seconds of Burn Time in a Mid-range Thermal Environment. (in K).....	68
Figure 47. Maximum Temperature of the Propellant throughout the Burn Time in a Mid-range Thermal Environment. (in K).....	68
Figure 48. Steady State Heat Transfer through System with Solid Combustion Chamber.....	72
Figure 49. Steady State Heat Transfer through System with Solid Combustion Chamber.....	72
Figure 50. Zoomed View of Steady State Heat Transfer through System with Solid Combustion Chamber.....	73
Figure 51. Model Representing the Hot Fire Test after 2 seconds of Burn Time.....	74
Figure 52. Projected Isp.	87

NOMENCLATURE

Variable	=	Name	-	Unit
A	=	Area	-	m ²
°C	=	Celsius	-	°C
c	=	Speed of Sound in Gas	-	m/s
c _p	=	Specific Heat	-	J/g-K
E	=	Energy	-	J
F	=	Force	-	N
G	=	Universal Gravitational Constant	-	m ³ /kg-s ²
g	=	Earth Gravity	-	m/s ²
h	=	Enthalpy	-	kJ/mol
I	=	Unit Tensor	-	
I _{sp}	=	Specific Impulse	-	seconds
K	=	Kelvin	-	K
k	=	Conductivity	-	W/m-K
M	=	Mach Number	-	
m	=	Mass	-	kg
\dot{m}_p	=	Propellant Mass Flow Rate	-	g/sec
p	=	Pressure	-	Pa
R	=	Universal Gas Constant	-	J/K-mol
S	=	Source	-	
T	=	Temperature	-	°C
t	=	Time	-	sec
u	=	Flow Velocity	-	m/s
v	=	Velocity	-	m/s
W	=	Watt	-	watts
Y	=	Mass Fraction	-	
γ	=	Ratio of Specific Heat	-	
δt	=	Increment of Time	-	sec
μ	=	Molecular Viscosity	-	m ² /s
ρ	=	Density	-	g/cm ³
σ	=	Boltzmann Constant	-	m ² -kg/s ² -K
$\bar{\tau}$	=	Stress Tensor	-	
 Subscript				
c	=	Chamber		
h	=	Heat		
I	=	inlet		

J	=	Species
m	=	Mass
op	=	Operating
p	=	Prop
ref	=	Reference
sun	=	Sun
w	=	Weight

1 - Introduction

The need for an efficient, cost-effective micropropulsion system has significantly increased over the past decade. This is caused by the increased usage and complexity in scope of small satellite missions. Currently various organizations are looking into a propulsion system that can be integrated with these small satellites. Due to the low mass, low power and the extreme close proximity of all of the parts, it has been difficult to find a good solution to this problem.

Stellar Exploration, Inc. has created a CubeSat module that includes a hydrazine monopropellant propulsion system. This system is designed to complete a mission that is proposed by the Georgia Institute of Technology (Georgia Tech). This propulsion system should be able to successfully complete seven pre-determined burns. There are two pre-planned rendezvous maneuvers, one is 43 seconds and the other is 12 seconds. There are two rendezvous cleanup maneuvers of 12 seconds each and three proximity operation burns of 0.5 seconds each.

1.1 – Motivation

The motivation for this thesis is to verify that a CubeSat can thermally withstand the implementation of a hydrazine monopropellant micropropulsion system. While it is beneficial to have propulsion systems that could be purchased off-the-shelf, this system would expand the boundaries for growth in CubeSat missions. The development of chemical micropropulsion systems increases thrust capabilities for future CubeSat missions and users.

This analysis is conducted using the dimensions and design provided by Stellar Exploration, Inc. This analysis is intended to contribute to the progress and development of other micropropulsion systems that will continue to expand CubeSat application.

1.2 – CubeSat Background

The standard CubeSat is a 10cm x 10cm x 10cm cube that is approximately 1kg in mass (1). This standardized unit is termed a 1U and is shown in Figure 1 (1). These standardized units are capable of being combined into 2 or 3 units, which are then termed 2U or 3U, respectively. Originally, CubeSats were used solely as experiments for college or university students to complete a system that was capable of being sent into space. These original CubeSats were designed to be acceptable for the strict safety requirements present in the university environment.



Figure 1. 1U CubeSat System (1).

Budget cuts across the Aerospace industry are causing an increasing need to utilize cost-efficient CubeSats to complete scientific research and space missions. The addition of a propulsion system allows for CubeSats to perform flight maneuvers. This

includes orbit change and raising, formation flying, proximity operations, fine attitude control, drag make-up and de-orbit. These increased capabilities will allow the aerospace industry to utilize CubeSats to complete missions that otherwise would have to cost exponentially more with a standard-size satellite.

1.3 – Micropropulsion Systems

Various systems have been considered in this search to find an ideal solution to adding propulsion capabilities to a CubeSat. These systems have included chemical, electrical and propellant-less thruster options. Each of these propulsion options includes advantages and disadvantages. At this time, none of them are actually flight proven in this capacity and there is no proven thermal analysis available for these systems.

1.3.1 – Chemical Monopropellant Thrusters

Monopropellant thrusters are generally utilized due to their simple design. The setup of this system typically includes an injector, catalyst bed and a converging-diverging nozzle. Successful miniaturization of these thrusters would offer increased specific impulse and delta-v capability, while providing thrust levels required for rapid orbit transfer. A couple benefits of these thrusters include their ability for multiple restarts and their high reliability. The two propellants most considered for a monopropellant microthruster are hydrazine and hydrogen peroxide.

At present, there are hydrazine thrusters being designed and manufactured in smaller scale. These are typically used for attitude adjustments on larger satellites. However, they could be converted for use as a main propulsion system on a CubeSat. The biggest issue with hydrazine is the potential for explosion. This is particularly sensitive in

a university setting where there is not the experience with safe handling of hydrazine that is present in the aerospace industry.

The Jet Propulsion Lab (JPL) developed the Hydrazine milli-Newton Thruster (HmNT) that could meet some of the requirements of the system. However since it was designed for attitude control on large spacecraft, the valves use more power than what would be available on a small spacecraft (2). The HmNT is shown in Figure 2.

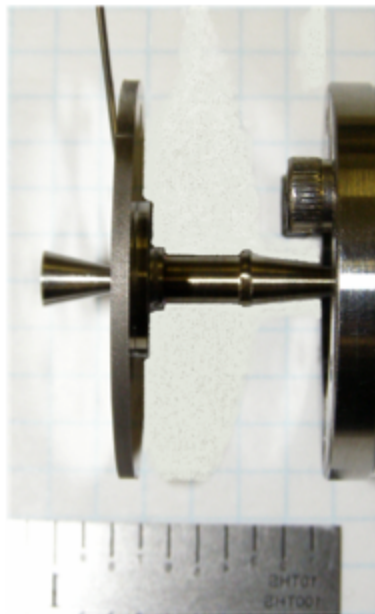


Figure 2. JPL Hydrazine Milli-Newton Thrusters (HmNT) by Parker et al (2).

The specifications for the HmNT are similar to those of the system that Stellar Explorations, Inc. has designed and manufactured. These small hydrazine thruster performance metrics are compared in Table 1. This shows the tradeoff that Stellar Exploration, Inc. can provide a Newton of thrust, but at over twice the mass of the thruster. However, the Stellar Exploration, Inc. thruster also has lower power requirements to operate the valves and fills a smaller volume of the spacecraft.

Table 1. Hydrazine Micropropulsion Thruster Performance Comparisons (2).

Parameter	JPL HmNT	Stellar Exploration, Inc.
Thrust (mN)	129	1000
Isp (sec)	150	210
Volume (cm ³)	8	3.18
Power- Open Valve (W)	8	0.5
Mass (g)	40	95

Hydrogen Peroxide Monopropellant thrusters have recently become reconsidered for university use because of the non-toxic nature of the propellant. However, certain storability concerns come along with using hydrogen peroxide. Hydrogen peroxide begins decomposing when heated or exposed to a catalyst- where almost any organic material acts as a catalyst (2). This decomposition can lead to over-pressurization of the tanks. However, using higher purity hydrogen peroxide can help to reduce the rate of decomposition (2). Measured thruster prototype performances by Scharlemann et al. show thrust capability of 100 to 800 mN and an ambient specific impulse of approximately 100 seconds (2). This thruster prototype is shown in Figure 3.

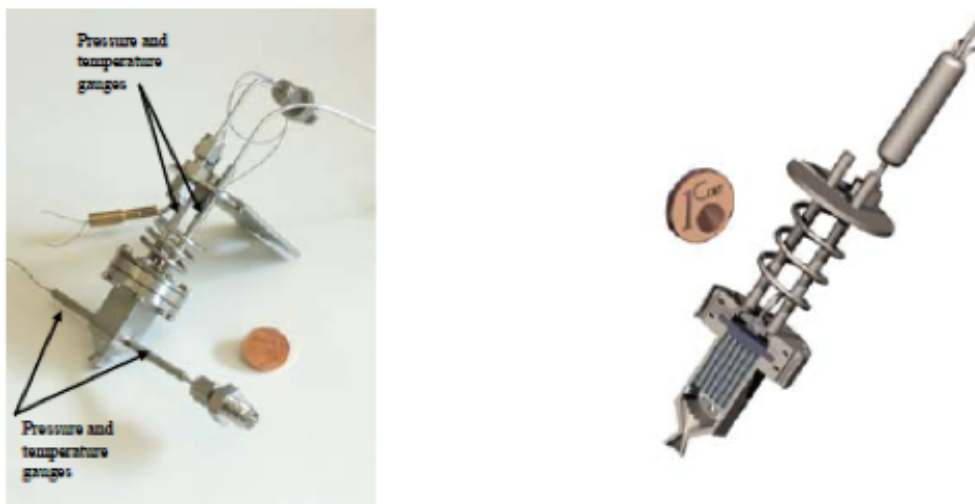


Figure 3. Miniature Hydrogen Peroxide Thruster by Scharlemann et al. (2)

NASA Goddard Space Flights Center (GSFC) initially developed a hydrogen peroxide thruster based on Microelectromechanical systems (MEMS) (2). This MEMS based device contained a planar catalyst bed and nozzle that was entirely MEMS fabricated and machined into silicon. This MEMS technology is being considered for a variety of micropropulsion systems that are being developed (2).

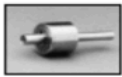
1.3.2 – Cold Gas Thrusters

Cold gas systems are being considered for use as a micropropulsion system due to their degree of simplicity. These thrusters offer low impulse bits and can utilize non-toxic propellant. In addition to this, the propellant is contamination free to help protect sensitive spacecraft. While these components are not currently designed with a microspacecraft application, the hardware is very small and light weight. This makes it compatible to integrate with CubeSat systems. Moog makes a variety of these systems that are available off-the shelf. These systems weigh as little as 9 grams and are as small as 12x35 mm, however utilize power levels that range from 10W to 40W. This is more power than what current CubeSat systems are capable of producing. (2) There is one thruster being developed that is an exception to this level of power usage. Marotta has developed a thruster that pulls in less than 1 Watt of power, at the cost of a thruster mass of around 70 grams (2).

In general, the high-pressure tanks needed to store the gas require a heavy weight tankage system. The large storage pressure also creates a risk of leakage across the valves, especially after an extended life period. Even with these setbacks, there are still various companies working on the miniaturization of these parts. Cold gas thruster

performance values are displayed in Table 2. This shows the correlations that as the size of the thruster increases, the amount of the thrust produced increases.

Table 2. Cold Gas Thruster Performance Comparison (2).

							
Manufacturer	Moog	Moog	Moog	Moog	Marotta	Moog	Moog
Model	58X125A	58E143 58E144 58E145 58E146	58E142	58E151	Cold Gas Micro-Thruster	58-118	50-820
Propellant	N2	N2	N2	N2	N2	N2	N2
Thrust (N)	0.0044	0.016 - 0.040	0.12	0.12	0.05 - 2.36	3.6	52-105
Mass (g)	9	40	16	70	<70	23	430
Size (mm)	11.9x34.7	13.97x57.2	14x20.3	19.05x 40.87		6.6x25.4	98.2x104.1
Valve Power (Open) (W)	10	10	<35	10.5	<1	30	47
Valve Power (Hold) (W)		1					
Isp (sec)	65	>60	>57	65	65	65	65
Operat. Pressure (psia)	0-50	0-36	50-300	0-400	100-2240	230	215-2515
Proof Pressure (psia)	300	290	600	1015	3360	1115	3765
Burst Pressure (psia)		508	1200	1615	5600		6265
Response (Open) (ms)	2.5	2.5	3.5	5	5	<4	<10
Response (Close) (ms)	2.5	2.5	3.5	3	5		<10
Minimum Ibit (mNs)					<44		
Life (No. of Cycles)	>15,000	500,000 - 2,000,000	20,000	1,000,000		>10,000	>6,000
Status	Flight Qual	Flight Qual	Flight Qual	Flight Qual	Flight Qual	Flight Qual	Flight Qual
Comments	Brilliant Pebbles, SAFER, Pluto Fast Flyby	CHAMP, GRACE	SIRTF	SIRTF	Developped for GSFC Nanosats, ST-5	SCIT, SAFER, Pluto Fast Flyby	COMET, Pegasus Cluster of 3 thrusters: 2 @ 52N, 1 @ 105N

1.3.3 – Liquefied Gas Thrusters

Liquefied gas thrusters have many of the benefits of the simplicity of a cold gas thruster, while additionally utilizing lower pressure within the tank construction.

Liquefied gas thrusters use propellants such as butane or ammonia, which is stored in liquid form. The propellant undergoes a phase transfer into gas during expansion. This means that the propellant can be stored in pressure ranging from 40-100psia, which allows for a much lighter tank configuration than cold gas thrusters (2). The lower pressure tank also helps to reduce concerns of propellant leakage during the mission.

In order to maximize the effectiveness of this design, a plenum is used to allow the propellant to completely expand and vaporize. The JPL Micro-Inspector

multifunctional tank design concept was one of the first to capitalize on this addition. This system had a delta-v capability of 15m/s, however required more power than is currently available on a CubeSat.

VACCO Industries developed a similar design using piezovalue technology called the Micro Propulsion System (MiPS), which dramatically decreased the power needed. This also eventually led to the joint development with Boeing of the Palomar design. This system provided a higher level of performance and increased capabilities, but at a much higher mass of over 1,300g.

The MiPS system was the first butane propulsion system designed specifically for CubeSats. The self-contained unit includes all of the system components and the butane fuel. This allows for a clean and simple integration with a CubeSat bus by attaching it on its side, as shown in Figure 4. This is one of the few CubeSat thrusters that is currently available off-the-shelf and ready for use, however with limited propulsive capabilities (2).

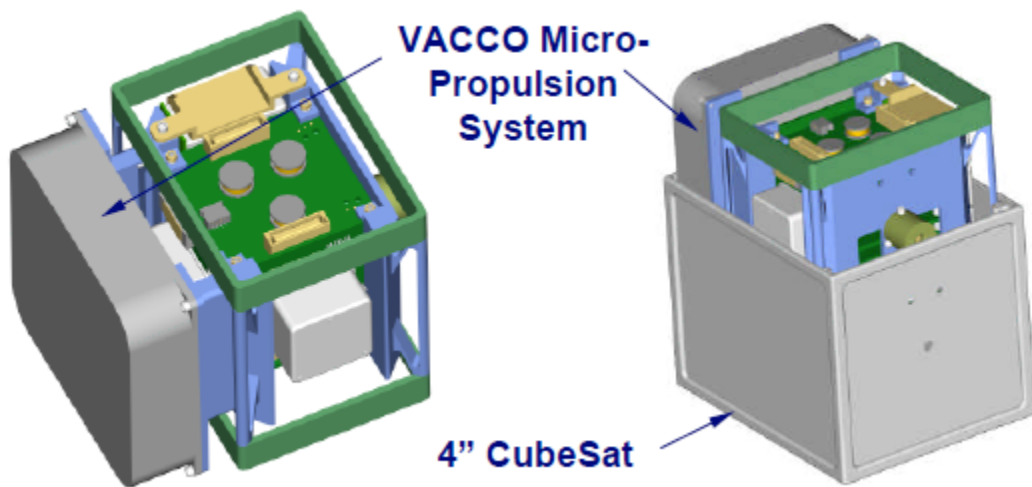


Figure 4. VACCO MiPS CubeSat Integration (2).

The demonstrated performance and easy integration of these butane systems makes them an ideal candidate for CubeSat application. They perform with low pressure storage, small power usage, and provide low delta-v, which is suitable for CubeSat missions and attitude control. As a trade-off they only offer limited specific impulse and delta-v capability.

1.3.4 – Solid Rocket Motors (SRMs)

Solid rocket motors can be considered for various spacecraft propulsion applications. This is largely due to their compact size and ease of integration into different spacecraft. In addition to this, they require no valves and can be external of the CubeSat mass and volume constraints. Some of the disadvantages of these systems is that they usually only have a one-time burn and they lack the accuracy of valve-controlled thrusters. These inaccuracies thrust and total impulse uncertainties require orbit trimming. These motors also provide a large thrust over a small amount of time which would create accelerations that are excessive, and possibly damaging, for a CubeSat. There are several end-burning SRMs that are an exception to this and produce 169N of thrust over a 21 second burn at a specific impulse of 250 seconds (2). In addition to these developments, several organizations have continued to minimize the size and force of these motors (2). However, this technology continues to pose numerous costly problems when it comes to system integration. An example of micromachined solid rocket motors is shown in Figure 5.

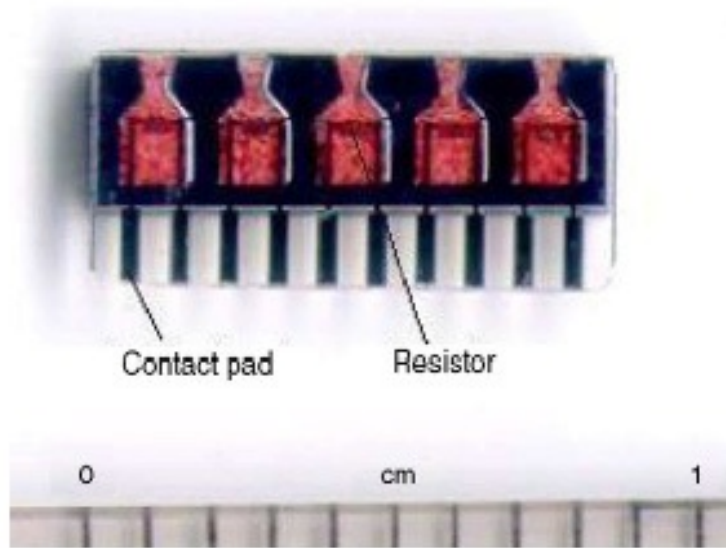


Figure 5. Micromachined Silicon Solid Rocket Motors by Zhang et al. (2)

1.3.5 – Bipropellant Thrusters

Chemical bipropellant thrusters are sometimes preferred as a primary thruster over monopropellant thrusters due to their higher performance. However, this added performance comes at the cost of more complexity and more dry mass. These systems must also remain pressure regulated and require a pressurization system composed of a tank and additional components. These added complexities are enough to make a bipropellant thruster less practical for CubeSat missions- where cost, mass and integration become extremely critical.

Regardless of the restrictions of bipropellant thrusters, several organizations have made developments in this area. However, many of these designs utilize a gaseous oxidizer, which is unrealistic for an actual spacecraft and would lead to similar issues experienced from the cold gas thruster. The miniaturization of this system has been best achieved at MIT, where they have developed an entirely MEMS-microfabricated bipropellant rocket engine assembly machined from silicon or silicon carbide. This

complex engine construction allows for a thrust of 2.7N at 300-second vacuum Isp to be obtained at a chamber pressure of 30 atmosphere (2). This engine concept is shown in Figure 6.

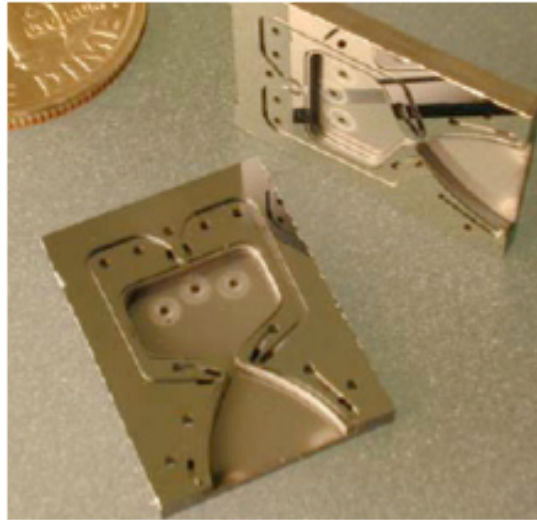


Figure 6. MIT Micro Bipropellant Engine Concept (2).

1.3.6 – Electric Propulsion

There are varying options of electric propulsion that are being considered for CubeSat application. Some of these systems are on the verge of being flight ready and available off-the-shelf, while others still have considerable development necessary.

Due to their proven operation, small impulse bits and modularity, Pulsed Plasma Thrusters (PPTs) were one of the first propulsion systems considered for microspacecraft application. The focus of this miniaturization of technology was mass reduction in the power electronics, specifically developing lighter capacitor designs. These designs range in size and this technology started with the “Dawgstar” PPT. This was originally designed for a system that was slightly larger than a CubeSat can be seen in Figure 7 (2).

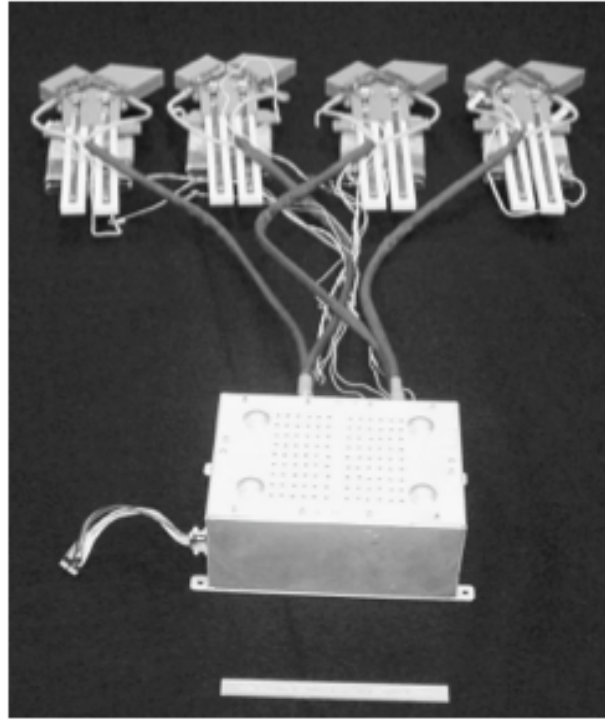


Figure 7. The "Dawgstar" PPT Thruster System (2).

Micro-PPTs continue to be developed with modifications such as coaxial fuel rod in place of the spring-loaded fuel rods. In a 2-electrode rod, a conductive center rod is surrounded by an annulus of Teflon, which is contained inside an outer conductive rod. Many of these developments to technology included failures along the way. This development is important to CubeSat propulsion since these systems are flight-proven on a larger 100kg micro-satellite and engineers see an easy transfer to CubeSat application. A comparison of Micro-PPT system performance is shown in Table 3. This comparison shows that while the mass ranges from 10 grams to 4000 grams, the amount of power needed always remains within a capable level for a CubeSat.

Table 3. Micro-PPT Performance Comparison (2).

Parameter	Dawgstar	AFRL μ PPT	ARCS μ PPT	MILIPULT
Ibit (μ Ns)	60	2	2-25	0.4 – 0.6
Thrust (μ N)	61-264	2-30		
Isp (sec)	266			
Mass (g)	4200 (system)	500 (system)	30 (5 g propellant)	13.5
Total Impulse (Ns)	1000			
Power (W)	15.6 - 36	1-20	0.5 – 4 (est.)	
Discharge Energy per Shot (J)	4.9	2.25		0.018 – 0.22
Capacitance (μ F)	1.3 (per module)	0.42	2-6	0.937
Voltage (kV)	2.8	2.45 – 5.36		0.2 – 0.7
Frequency (Hz)	1-2			
Efficiency (%)	1.8			
Life (pulses)	1.7			
Propellant	Teflon	Teflon	Teflon	Water
Reference	[52]	[6], [51]	[54]	[55]

Even in optimal performance, the total impulse of these systems is limited and it operates in a pulsed mode, making it suitable for precision pointing and small delta-v maneuvers (2).

The Vacuum Arc Thruster (VAT) design is similar to the PPT, with the difference of utilizing metal electrodes. This process involves applying high voltage between two electrodes which results with plasma generation in an arc discharge. There are various cathode materials that can be utilized and the impulse bits vary with the electrode material that is chosen.

Overall the VAT has the benefit that its models were designed specifically for CubeSat application. A CubeSat VAT module was developed by the Alameda Applied Sciences Corp.(AASC) and is shown in Figure 8 (2).

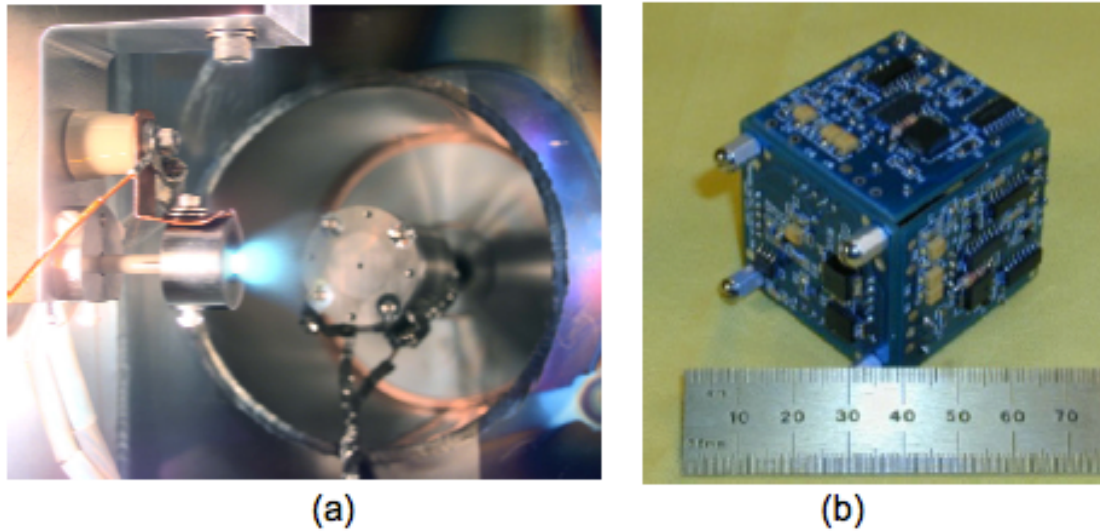


Figure 8. (a) VAT Thruster Firing on the JPL Micro-Newton Thrust Stand. (b) VAT PPU Configured for CubeSat (2).

The other advantages of this system include its low impulse bits and solid propellant storage allowing for compact and modular design. Unfortunately, this propulsion system is suitable for very few maneuvers due to the limited total thrust values and the fact that it inherently functions in pulsed mode. This makes it an ideal thruster for precision pointing and attitude control purposes.

Miniature ion thrusters have recently been developed, although not originally with the intention of being used for CubeSat applications. Instead these were developed for formation flying applications in environments that have sensitive optical surfaces and that are sensitive to rugged acceleration. Several companies, including JPL, have worked to microfabricate the components needed for this technology. Through their Ion Thruster on a Chip (ITOC) concept, JPL was able to develop a 3-cm diameter version which was termed the Miniature Ion Xenon Thruster (MiXI) and is shown in Figure 9 (2).



Figure 9. JPL Miniature Xenon Ion Thruster (MiXI) (2).

The miniaturization of an RF-ion engine is appealing since no internal cathode is required in the system. Small versions of this technology have been under development since as early as 1972 (2). The majority of these thrusters were designed and tested with Xenon as the propellant; however Argon testing has also been conducted. The performance characteristics of these miniature ion thrusters are displayed in Table 4. With this technology, there are still concerns with high power usage over 10 W and low thrust outputs below 1mN. This comparison shows that the Argon engine outputs less thrust than the Xenon engine at a very high specific impulse.

Table 4. Micro-Ion Engine Performance Comparison (2).

	MiXI	μ NRIT-2.5	MRIT
Thrust (mN)	0.01 – 1.5	0.05 -0.6	0.001 – 0.06
Isp (sec)	2500 - 3200	2861	5480
Power (W)	13-50	13-34	
Electrical Efficiency (%)	> 40	4 - 47	15
Mass Utilization (%)	> 70	15 - 52	
Dia (cm)	3	2.5	2
Mass (g)	200	210	
Propellant	Xenon	Xenon	Argon

Extending miniature ion engine technology to apply to CubeSats would result in many advances for the small satellite industry. These engines would not only provide the delta-v capability for orbital change and extended drag make-up, but potentially the mission flexibility to allow CubeSats to explore beyond Earth's orbit. Before missions of this scope can be achieved, there are several areas that require significant development for miniaturization. This requires reduction of the engine size, including the feed systems and PPU. These modifications would allow for the integration of this engine into a 3U CubeSat architecture.

Development for colloid thrusters has taken place since the 1960s, when they were studied extensively in several different companies within the United States. Over the years, interest in these small thrusters dwindled as spacecraft size increased (2). The need for a micropropulsion system sparked up interest in this past technology. Colloid thrusters have the advantage over ion engines since they do not require a plasma discharge. Instead, these thrusters emit ions or charged droplets directly from the emitter tip and into an electric field. Once this electric field is intensified, ions are broken up into charged liquid droplets (2).

Due to the sub-millimeter sizes of emitter tips and the compact nature of the thruster, these systems are easily miniaturized. In the early 2000s, further development was made on these thrusters by NASA and a colloid cluster, shown in Figure 10, was flown in several missions (2).



Figure 10. ST-7 Colloid Thruster Cluster (2).

While this cluster is too large to integrate onto a CubeSat, it is composed of nine individual emitters. This technology could be customized to meet the needs of CubeSat applications with the development of a dedicated feed system and PPU. The range of performance characteristics for this cluster technology can be seen in Table 5. Utilizing individual emitters would result in the feasible power usage of 2W per emitter and would decrease the already low mass.

Table 5. Colloid Thruster Performance Characteristics (2).

Parameter	Demonstrated Performance
Thrust (μN)	5 – 35.8
Thrust Noise (μN)	<0.01
Isp (sec)	240
Mass (kg)	15
Power (W) - Max	24.6 (all thruster heaters at max at 2 W each)
Power (W) - nominal	16
Beam Divergence (Half Angle) (degree)	<23

While most of these technologies have potential for advancement within micropropulsion, this section has described why some of these propulsion types are currently more feasible than others. This is based on the thruster performance capabilities and the current availability of resources for CubeSat missions.

2 –System Configuration

Stellar Exploration, Inc. chose to design a hydrazine monopropellant thruster.

This design decision was made due to higher delta-v performance than a cold gas thruster and larger thrust values than an electric propulsion system. This allows for the system to be ideal for orbit transfer application. This section will talk specifically about the configuration of the system that is being modeled. This is shown in Figure 11 with mass values.

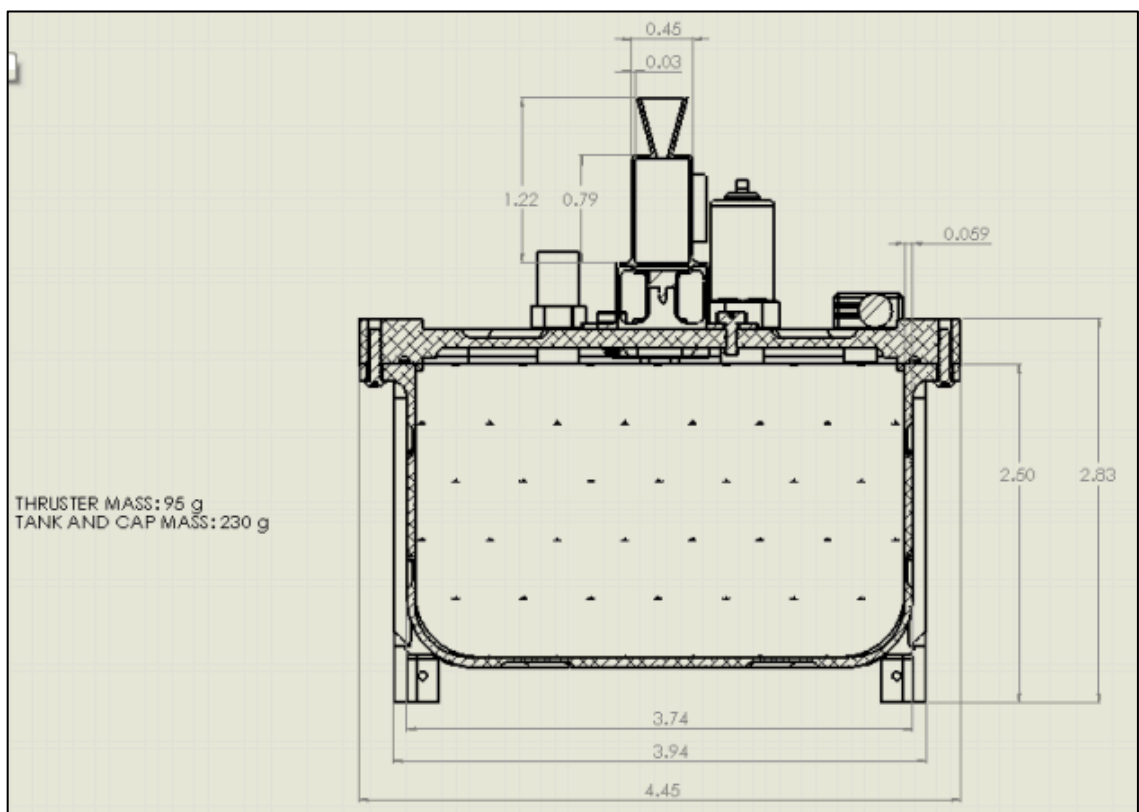


Figure 11. Propulsion System Unit with Specified Dimensions (in inches).

2.1 – Thruster Unit Design

The 1U propulsion system concept by Stellar Exploration, Inc. is designed to be integrated into a 3U system. The other units would include the electronics section and a

payload section, as shown in Figure 12. This entire system meets the requirements for integration with the standard CubeSat launching mechanism, known as the Poly-PicoSatellite Orbital Deployer (P-POD) (1).

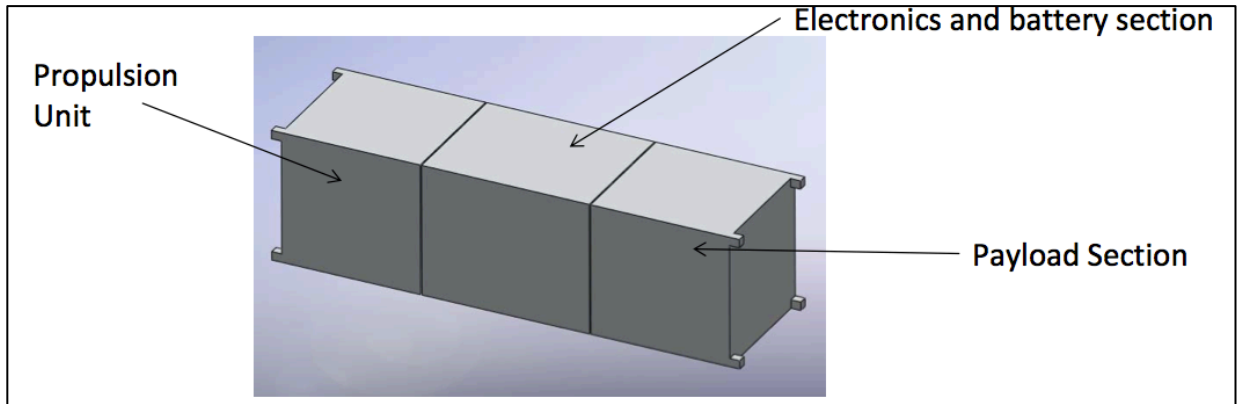


Figure 12. 3U CubeSat Demonstrating Compartment Assignments (3).

Hydrazine was selected as the propellant for this system due to its mature technology. Piping and instrumentation for hydrazine are manufactured and proven to survive with this propellant, which is not the case with newer “green” propellants. A monopropellant system is less complex than a bipropellant system due to fewer valves required for only one type of propellant. Monopropellant systems utilize less volume and mass in the spacecraft than the bipropellant system, with the tradeoff of slightly lower performance. After numerous iterations, Stellar Exploration, Inc. decided to use a design that included one thruster located along the centerline of the tank, as opposed to multiple thrusters on the corners of the tank. The final thruster design is shown in Figure 13.

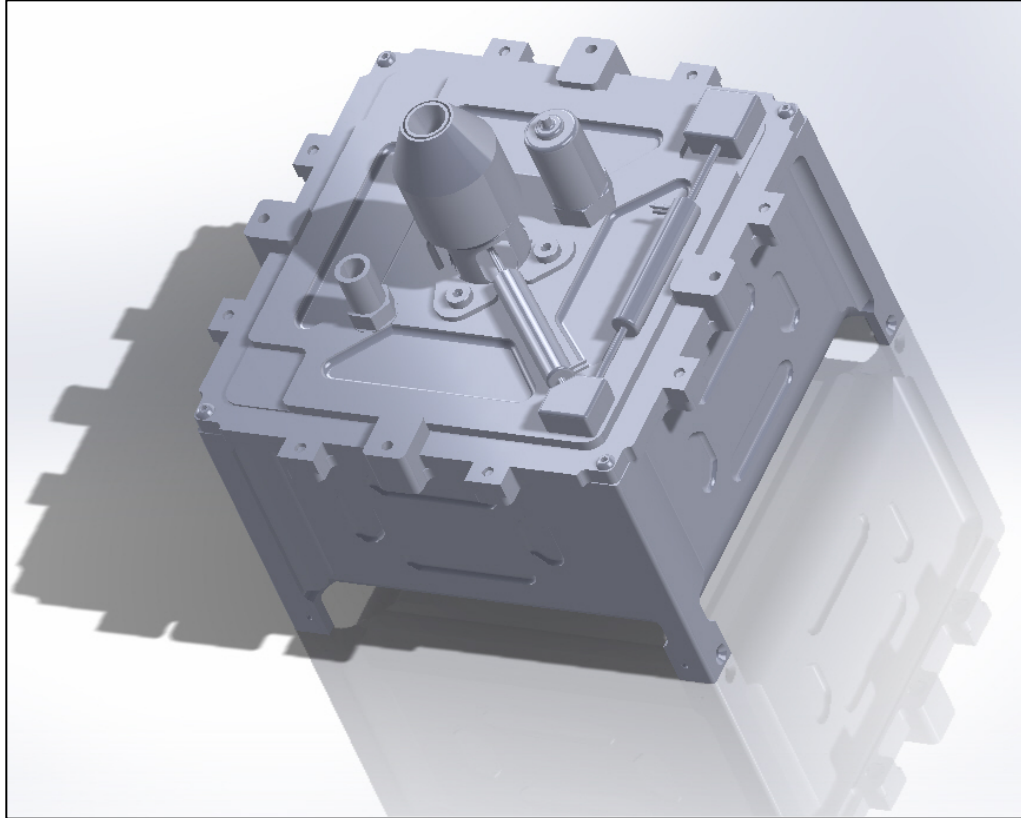


Figure 13. CAD 3-D Model of Micropropulsion System by Stellar Exploration, Inc.

2.1.1 – Thermal Properties of Thruster Materials

The thruster is designed similar to a typical spacecraft and uses flight-proven materials. The majority of the thruster and thruster components are made from 316 stainless steel. This includes the thruster body, solenoid valves, pressure transducer, transition tube manifold and 45-degree manifold. 316 stainless steel has a density of 8.03 g/cm^3 , a specific heat of $0.50 \text{ kJ/kg}\cdot\text{K}$ and a thermal conductivity of $16.2 \text{ W/m}\cdot\text{K}$ at 100°C through $21.4 \text{ W/m}\cdot\text{K}$ at 500°C . The melting range is from 1399°C to 1454°C and the maximum temperature which it can be exposed continuously without appreciable scaling is 899°C (4).

The drain fill valve in the system is made with aluminum alloy 2024. Aluminum 2024 has a density of 2.78 g/cm^3 , a specific heat of $0.875 \text{ kJ/kg}\cdot\text{K}$ and a thermal conductivity of $121 \text{ W/m}\cdot\text{K}$ at 100°C . The melting range is from 502°C to 638°C and its solution temperature is 256°C (5). Lastly, the propellant tank and cap are CNC machined from aluminum 6061-T6 with P-POD rails integrated into the tank structure. Aluminum 6061-T6 has a density of 2.7 g/cm^3 , a specific heat of $0.896 \text{ kJ/kg}\cdot\text{K}$ and a thermal conductivity of $167 \text{ W/m}\cdot\text{K}$ at 100°C . The melting range is from 582°C to 652°C and its solution temperature is 529°C (6). The machined propellant tank and lid are shown in Figure 14. The tank to cap interface is sealed with EDPM O-ring, which can be seen along the lid edge (3).

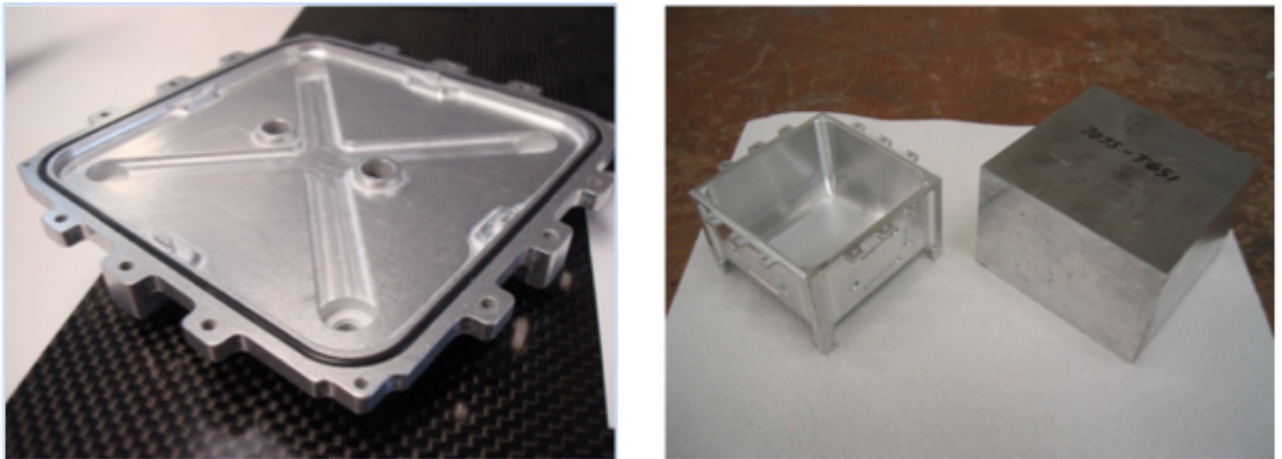


Figure 14. Aluminum 6061-T6 Tank and Lid (3).

2.1.2 – Thermal Properties of Propellant and Reaction

Hydrazine (N_2H_4) can be an extremely toxic and unstable propellant if not handled properly. Years of using this product in the aerospace industry have created safe handling and storage procedures. In a hydrazine monopropellant thruster, the hydrazine is passed by a catalyst causing it to quickly decompose. For this thruster, the catalyst is a

platinum-iridium alloy “screen” that is made with a ratio of 80% platinum to 20% iridium. These screens are stacked together and held in place by a stainless fastener shown in Figure 15 (3).

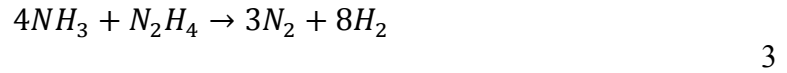
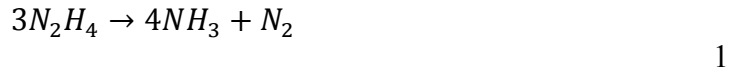


Figure 15. Platinum/Iridium Catalyst (3).

In order to achieve the reaction, the catalyst heater is brought to a temperature of 250°C. This heater consists of a NiCr wire embedded in a cast ceramic cylinder around the thruster body and it dissipates around 5W to 10W. The system includes double redundant solenoid valves in order to meet range safety requirements. These utilize 0.5W to open the valve for propellant flow.

Due to the unstable qualities of hydrazine, it should be stored at approximately 15°C. The auto ignite temperature of this fuel is anywhere between 25°C and 270°C. Due to the setup of this problem, Stellar Exploration, Inc. will allow for the propellant temperature to reach up to 200°C before being considered critical. In order to ensure that the reaction starts, the heater at the combustion chamber is heated to 250°C to begin the reaction. The actual reaction temperature of hydrazine is 800°C. This reaction allows the

hydrazine to decompose into ammonia, nitrogen gas, and hydrogen gas through equations 1, 2, and 3 (7).



Due to the first two equations being extremely exothermic, the combustion chamber can reach its reaction temperature of 800°C in milliseconds. Shortly thereafter, it reaches its steady state temperature of 845°C (7). This quick jump to the steady state temperature allows modeling of the heat transfer completely at the steady state. This can be done while still achieving an accurate representation of the thermal conditions.

Based on values given from Stellar Exploration, Inc., steady state temperature at the pressure for this thruster will be modeled as 845°C. Other samples of test fire data can be found that verify this value as the steady state temperature (8; 9). A study on hydrazine monopropellant rocket engines conducted by the Air Force Rocket Propulsion Lab, found a steady state temperature of 760°C from the outside of the chamber. This Thermal Design Verification Test (TDVT) was done for a 100 second burn to determine the steady state temperature of the walls of the chamber (8). Another study was conducted by the Korea Advanced Institute of Science and Technology using multiple inlet pressures. Based on our chamber pressure of 80 psi (5.51580583 bar), their tests indicate that our steady state chamber temperature should be between 734°C and 770°C. The comparative results for the variable inlet pressures are shown in Table 6 (9).

Table 6. Hot fire test results of a hydrazine monopropellant thruster (9).

P_i , bar	P_C , bar	T_c , °C	SST, N	I_{sp} , s	\dot{m}_p , g/s
4.42	3.1	728	0.99	211.52	0.48
4.47	3.0	734	1.00	223.45	0.46
6.99	4.6	770	1.51	218.14	0.71
7.69	5.0	792	1.67	220.29	0.77
7.94	5.1	803	1.68	241.90	0.72
17.13	9.8	880	3.28	223.14	1.50
17.43	9.9	888	3.42	226.61	1.54
24.00	12.8	889	4.51	230.99	1.99
26.40	14.0	887	4.64	227.42	2.08
26.48	13.9	894	4.76	227.01	2.14

3 – Thermal Analysis

A need for efficient ways to validate thruster performance increases as demand grows for more diverse monopropellant systems. The testing performed to validate the system becomes very costly and risky as the thrusters complexity increases. Some of this cost and risk can be alleviated by providing more efficient and accurate computational analysis with numerical simulations. This leads to a more efficient development process while eliminating the need to run numerous repetitive tests during the preliminary design phase. The study of these hydrazine reactions has been conducted from as early 1949 at the California Institute of Technology's Jet Propulsion Lab (9). Throughout the years, mathematical models of general thruster performance have been continuously improved and validated against test data.

3.1 – Calculation Background

There are several factors that must be considered to determine the appropriate setup of a thermal analysis problem to properly represent the heat transfer in the system. These factors will be described along with the reasoning for why decisions were made in this specific analysis process.

3.1.1 – Compressible vs. Incompressible Flow

The subsonic velocity area and supersonic velocity area coexist within a thruster. Therefore any equation needed to fully represent the flow must cover both the compressible and incompressible flow regimes as the flow develops.

If a flow is compressible, the density is a non-constant function of other properties, which includes the temperature, material composition, and pressure. An incompressible flow is an idealized case, where the variations of pressure and

temperature encountered by a particle cause zero change in the density of the particle. In an incompressible flow, there is no change with respect to time in the specific volume, and therefore density, of each particle of fluid. Thus, the density is constant along any given particle path line defined as the curve traced out over time by a given particle (9).

Compressible flows can be characterized by the value of the Mach number

$$M \stackrel{\text{def}}{=} u/c \tag{4}$$

where u is the flow velocity and c is the speed of sound in the gas, defined as

$$c = \sqrt{\gamma RT} \tag{5}$$

where γ is the ratio of specific heats (c_p/c_v), R is the universal gas constant and T is the absolute temperature. As the Mach number approaches and exceeds 1.0, the effects of compressibility become important to the calculation (10).

Typically a compressible flow equation is not efficient for solving incompressible flow because the pressure term increases as $1/M^2$ decreases compared to the convective term. Therefore, a stabilized modification of the compressible flow equation is used to allow for a wide range of Mach numbers. ANSYS FLUENT models the flow as both incompressible and compressible in the computational heat transfer analysis (10).

3.1.2 – Steady State vs. Transient Flow

Steady state flow occurs when the magnitude and direction of flow is constant with time throughout the entire domain. Conversely, transient flow is when magnitude and direction of flow change with time. Steady state means that the amount of fluid within the domain stays the same, and that the amount of fluid that flows into the system, is the same amount that flows out of the system. Modeling a steady state flow is

significantly easier than modeling a transient flow since time is no longer an independent variable. Transient flow will be utilized to allow for a more accurate representation of propellant flow over time.

3.2 – Numerical Analysis Prediction

Equations 6, 7, 8 are used for predicting analysis results and to set the initial values for the simulation. These equations are based on the curve data that was collected from hot-fire tests of similar micro monopropellant hydrazine thrusters using iridium as a catalyst (9). These equations allow for the calculation of the chamber pressure and temperature using the initial pressure (in bars) in the following equations (9)

$$T_c [^{\circ}\text{C}] = 0.017P_i^3 - 1.287P_i^2 + 33.293P_i + 604.936 \quad 6$$

$$P_c [\text{bar}] = 0.494P_i + 1.021 \quad 7$$

$$\dot{m}_p [\text{g/s}] = 7.434 \times 10^{-2} P_i + 0.213 \quad 8$$

Equations 6, 7, and 8 were calculated with the pre-determined inlet pressure of 80psi, which is 5.51580583 bar. This value was determined by Stellar Explorations and should produce results of a chamber temperature of approximately 752.2706°C (1025.42K), chamber pressure of approximately 3.5691 bar and propellant mass flow of 0.623 g/s. These values were used to validate that the temperatures being produced through the computational thermal analysis provide similar results to test data of similar systems (9).

3.3 – Modeling in ANSYS FLUENT

ANSYS FLUENT provides the ability to do steady state or transient analysis with various models of incompressible and compressible, laminar and turbulent fluid flow. In

addition to fluid flow through complex geometries, ANSYS FLUENT can perform computational heat transfer through conduction, convection and radiation (11).

3.3.1 – Continuity and Momentum Equations

For all flow modeling, ANSYS FLUENT solves conservation equations for mass and momentum. The general form of the equation for the conservation of mass is as follows

$$\frac{\partial \rho}{\partial t} + \nabla \cdot (\rho \vec{v}) = S_m \quad 9$$

where ρ is the density, ∂t is an increment of time, \vec{v} is the velocity and S_m is the source of mass added to the continuous phase and any user-defined sources (10). This general equation is valid for both incompressible and compressible flows.

Conservation of momentum in an inertial reference frame is described by

$$\frac{\partial}{\partial t} (\rho \vec{v}) + \nabla \cdot (\rho \vec{v} \vec{v}) = -\nabla p + \nabla \cdot (\bar{\tau}) + \rho \vec{g} + \vec{F} \quad 10$$

where p is the static pressure and $\rho \vec{g}$ and \vec{F} are gravitational body force and external body forces, respectively (10). The external body forces also contain any other model-dependent or user-defined sources. Lastly, $\bar{\tau}$ is the stress tensor and is defined by

$$\bar{\tau} = \mu [(\nabla \vec{v} + \nabla \vec{v}^T) - \frac{2}{3} \nabla \cdot \vec{v} I] \quad 11$$

where μ is the molecular viscosity, I is the unit tensor and the second term on the right hand side is the effect of volume dilation (10).

3.3.2 – Modeling Compressible Flow

Compressible flows are described by the standard continuity and momentum equations that are solved in ANSYS FLUENT. Therefore you do not need to activate any specific model in order to achieve compressible flow results. Within ANSYS FLUENT, the energy equation must be indicated if solving heat transfer cases. This ensures that the flow velocity is correctly coupled with the static temperature (12). For compressible flow in ANSYS FLUENT, the ideal gas law is modeled as

$$\rho = \frac{p_{op} + p}{\frac{R}{M_w} T}$$

12

where p_{op} is the operating pressure that is defined by the user, p is the local static pressure relative to the operating pressure, R is the universal gas constant and M_w is the molecular weight from the material. For this equation, the temperature, T , will be computed from the energy equation (10).

3.3.3 – Modeling Heat Transfer

Heat transfer is defined as the flow of thermal energy from matter occupying one region in space to matter occupying a different region in space. Heat transfer is the primary focus in this thesis and occurs through conduction, convection and radiation. ANSYS FLUENT is capable of solving all of these methods from the simplest conduction problem through advanced natural convection models. Based on the methods of heat transfer that are specified, ANSYS FLUENT will solve the correct variation of the energy equation (10). These models are activated by including relevant physical

models, supplying thermal boundary conditions, and inputting material properties that govern the heat transfer.

ANSYS FLUENT allows for the heat transfer within fluid, as well as solid regions in the model. This allows the modeling of the thruster system and tank, as well as the propellant flow through the system. Due to modeling the propellant in the vacuum conditions of space, the propellant can actually be modeled as a solid to allow for simpler calculation of the heat transfer across the system (10).

In ANSYS FLUENT, the energy equation is solved in the following form

$$\frac{\partial}{\partial t}(\rho E) + \nabla \cdot (\vec{v}(\rho E + p)) = \nabla \cdot \left(k_{eff} \nabla T - \sum_j h_j \vec{J}_j + (\bar{\tau}_{eff} \cdot \vec{v}) \right) + S_h \quad 13$$

where k_{eff} is the effective conductivity and \vec{J}_j is the diffusion flux of species j (10). The first three terms that are on the right hand side of the equation represent the energy transfer due to conduction, species diffusion and viscous dissipation. These terms are eliminated as the model is simplified for the necessary heat transfer. Also, S_h includes the heat of reaction or any other heat sources that are defined by the user (10). In the energy equation provided

$$E = h - \frac{p}{\rho} + \frac{v^2}{2} \quad 14$$

where sensible enthalpy h is defined for incompressible flows as

$$h = \sum_j Y_j h_j + \frac{p}{\rho} \quad 15$$

In this equation, Y_j is the mass fraction of species j and

$$h_j = \int_{T_{ref}}^T c_{p,j} dT$$

16

where T_{ref} is 298.15K (10).

The energy equation differs in solid regions and has the following form

$$\frac{\partial}{\partial t}(\rho h) + \nabla \cdot (\vec{v}(\rho h)) = \nabla \cdot (k \nabla T) + S_h$$

17

In this equation, ρ is density, h is sensible enthalpy, k is conductivity, T is temperature, and S_h is volumetric heat source. The second term on the left hand side represents convective energy transfer due to rotational motion of solids and is therefore not utilized in our model. The velocity field \vec{v} would be computed from the motion specified for the solid zone. On the right-hand side of the equation, the terms are heat flux due to conduction and volumetric heat sources within the solid (10).

4 – ANSYS ICEM and FLUENT Setup

Using the background equations that are provided and calculated in the previous section, this problem is now entered into ANSYS software. Prior to conducting heat transfer, a mesh is created within the structure of the system. This is done using ANSYS ICEM. Once the mesh is developed to a high enough quality, then the system is exported to ANSYS FLUENT where heat transfer can be modeled.

4.1 – Modeling Low Earth Orbit (LEO) Environment

4.1.1 – High Vacuum

Pressure in space is typically defined as a vacuum, where in Low Earth Orbit the values range between approximately 3.2×10^{-2} Pa to 1×10^{-9} Pa (13). This is modeled conservatively to allow for no conduction from the walls of the spacecraft into the space environment.

4.1.2 – Radiation

While conduction and convection are not accounted for in the external space environment, the effects of radiation play an important part in the thermal analysis of a spacecraft. This means that the physical properties, especially the optical properties of the external walls, can heavily influence the temperature of the spacecraft (14).

Due to the fact that external heat transfer into the system will be present primarily from radiation, the worst-case environment was considered being in orbit in the sun. Stefan-Boltzmann's law for a black body in sunlight was calculated an approximate temperature with the following equation

$$S_{sun} = \sigma \cdot T^4 \text{ (W/m}^2\text{)}$$

where T is the temperature in Kelvin, σ is Boltzmann's constant

$$\sigma = 5.67 \times 10^{-8} \text{ W}/(\text{m}^2 \text{K}^4)$$

19

and S_{sun} is the power per unit area that is coming in contact with the spacecraft, which is also the solar constant. This is defined as the amount of incoming solar electromagnetic radiation per unit area that would be incident on a plane perpendicular to the rays at a distance of 1 astronomical unit (AU), which is the approximate mean distance from the Sun to the Earth. Satellite observations with the purpose of recalibrating this value have determined a value of (15)

$$S_{sun} = 1,360 \text{ W}/\text{m}^2$$

20

In the end, this produces a nominal maximum external temperature of 394 K in space and in sunlight.

The other factor that has an impact in space is the ambient particle flux. The following dominant particle species are considered for the orbital environment in LEO: oxygen ions, atomic oxygen, molecular oxygen and molecular nitrogen. For each of these particles, the kinetic energy is calculated, leading to the number densities and power fluxes for each particle species. With these values, the power flux of the sum of the particles is still smaller than the power flux of the sun by approximately three orders of magnitude. Therefore the assumption is made that the power flux from the particle species can be neglected and that the heat felt by the spacecraft due to radiation while in the sun is 394K (14).

4.2 – ANSYS ICEM Mesh Setup

4.2.1 – General Problem Setup

This section indicates some of the critical setup procedures and steps that were necessary to produce analysis of this system. It will include any assumptions that were made, as well as the reasoning behind them. Throughout the analysis process, many errors can occur when it comes to creating the geometry and mesh that are needed for the CFD Solver. This section ensures that the model can accurately represent the system.

To get started in ANSYS ICEM, upload a geometry model of the proper file type, or create the geometry from scratch. Due to some of the complications that come from the conversion of the file into the program, it was easier to create a 2-dimensional geometry within ANSYS ICEM.

Before creating a geometry model, it is important to distinguish the boundary conditions of every wall that will be created. It is recommended to identify which walls in the geometry serve as an interface to two or less materials and which walls interface between more than two materials. The first case with two or less can be entered as a wall boundary condition, while an interface with more than two must be entered as an interface boundary condition. Incorrect input of these boundary conditions will create errors while transferring into ANSYS FLUENT. Due to this, it is easiest to name each wall separately and then merge the walls once it is in the solver.

In the case of creating a geometry, it is beneficial to have independent curves and to label them in a way that describes where they are in the system. As the geometry becomes more complex, it becomes easy to overlook a point or curve. A sample geometry showing just the points and curves is shown in Figure 16.

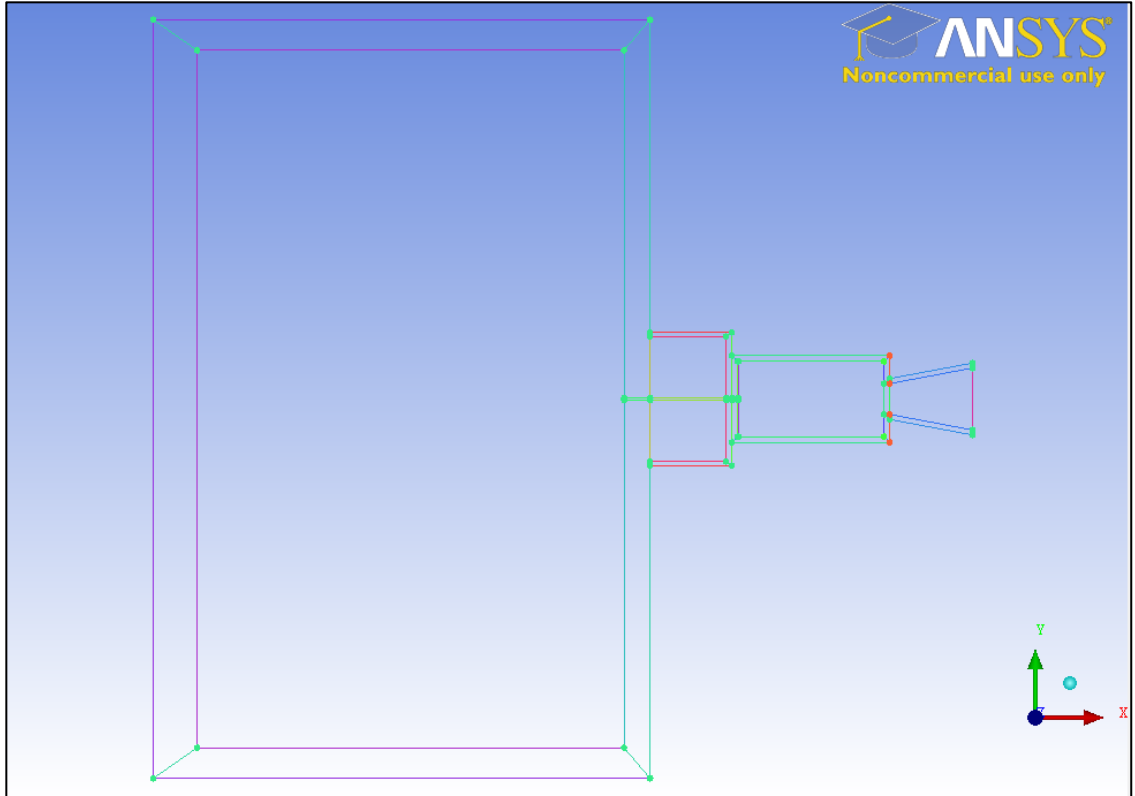


Figure 16. Sample Geometry from ANSYS ICEM Showing Points and Curves.

The next step, and also the most tedious in the thermal analysis process, is the development of the mesh. There are numerous approaches to creating a mesh in ANSYS ICEM based on the complexity of the geometry.

Any 3-dimensional geometry or complex geometry will utilize a step called blocking. This is a process where the geometry is split up into smaller-volume pieces in order to separate the different sections of the system. Once the blocks are created, they are associated to curves of the geometry and then transformed into a mesh.

For 2-dimensional models with primarily straight lines, a simpler type of meshing can be utilized that is called surface meshing. This allows for the user to separate the geometry into surfaces, which are shown in Figure 17. Once these surfaces look accurate, mesh setup can begin and values can be entered for the distance between nodes, height,

height ratio and size of mesh. Once values are entered for all interior sections, then a mesh can be generated. Any slight problem or overlapping section of the geometry will cause the mesh to not fill in properly and leave a mesh that cannot go into a solver. The ANSYS user defines the mesh type between tri and quad-shaped grids. This is determined based on the geometry. In a model with many straight, parallel lines, the quad-dominant mesh will tend to have higher quality.

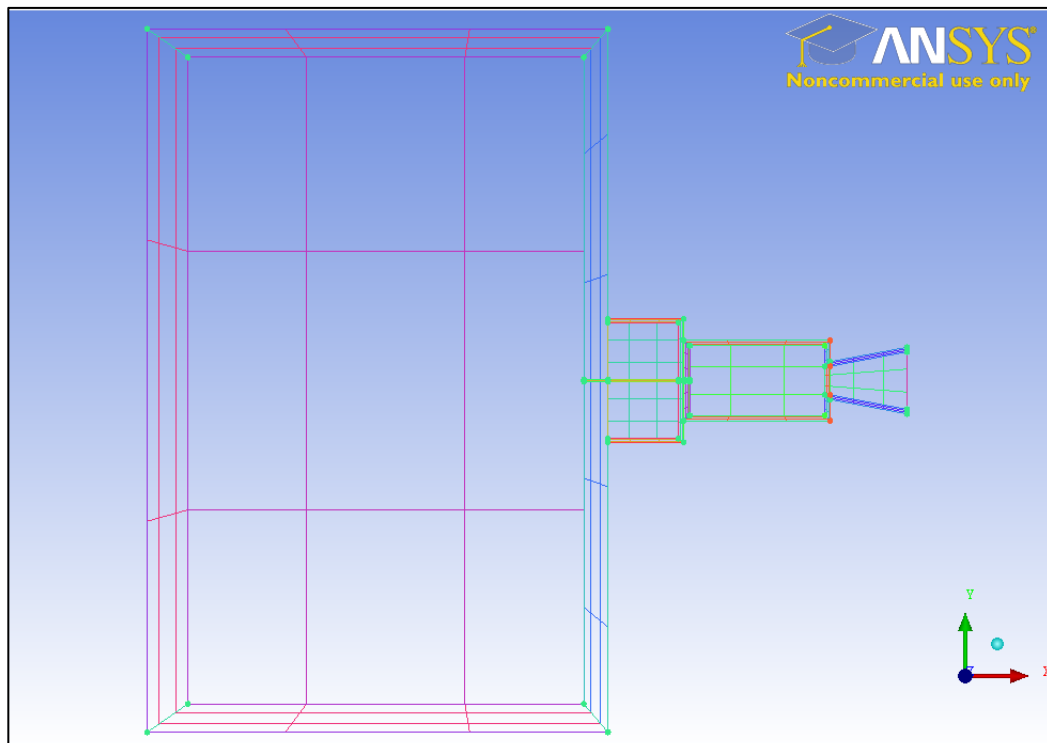


Figure 17. Sample Geometry Taken from ANSYS ICEM Showing Surfaces.

Now that the mesh has been created, it is important to run some checks before trying to continue on with the analysis. In ANSYS ICEM, there are easy ways to check the mesh, fill holes and refine coarse sections. Along with checking the mesh through the ANSYS Mesh Check, it is also good to do a visual check of the mesh for holes or other issues that do not meet standards. Figure **18** shows the output from the ANSYS Mesh

Check function. While checking the mesh, outputs are between 0 and 1 where numbers approaching 1 have the highest quality. This is shown in the histogram where all of the values are greater than 0.5. For a visual check of this mesh, it should appear consistent in shape and size and symmetric across the centerline.



Figure 18. Output from a Mesh Check for Quality.

Once the mesh is generated and it meets the needs of the ANSYS user, it can be output to a solver. With ANSYS ICEM, the counterpart solver for CFD and thermal analysis is ANSYS FLUENT. Before leaving the page it will have the user set the preliminary boundary conditions. This is the last chance to indicate the proper boundary conditions of the walls and surfaces. If everything was done properly, the mesh should have no issues exporting to ANSYS FLUENT.

4.3 – ANSYS Fluent Problem Setup

The next section discusses the setup that is needed to perform the actual heat transfer and thermal analysis through ANSYS FLUENT.

4.3.1 – General Problem Setup

The follow steps are needed to read a mesh in ANSYS FLUENT. These help to set the proper environment, solver and boundary conditions for the analysis.

First, you must determine whether to use a pressure-based solver or a density-based solver. Originally, the pressure-based solver was developed for low-speed incompressible flow, while the density-based solver was used for high-speed

compressible flows. However, now both approaches have been reformulated to operate for a wide range of conditions. This allows for both solvers to be able to accurately solve problems outside of their original purpose.

In the density-based solver, the density field is determined from the continuity equation, while the pressure field is determined by the equations of state. In the pressure-based solver, the pressure field is obtained by solving a pressure equation from manipulating the continuity and momentum equations. In both methods the velocity field is found through the momentum equations.

When choosing the velocity formulation, the formulation that results in most of flow domain having small velocities in that frame is preferred. This helps to reduce the numerical diffusion in the solution, which provides a more accurate solution. Absolute velocity formulation is preferred when flow in the majority of the domain is not rotating. In contrast, relative velocity formulation is used when the majority of the fluid in the domain is rotating.

Due to the nature of propellant flow, we will assume that there is minimal rotation throughout the domain and that the propellant is moving along a straight path line. This results in the use absolute velocity formulation to find the most accurate solution.

While using the two-dimensional solver, ANSYS FLUENT allows you to determine the how the space is set up. Planar indicates that the problem is two-dimensional. Axisymmetric indicates that the domain is axisymmetric around the x-axis. This allows for the 2D axisymmetric form to be utilized in the solver instead of the Cartesian form. Axisymmetric Swirl specifies that the circumferential component of velocity should be included in your axisymmetric model.

Based on the model being solved, we will only be using planar or axisymmetric for our models.

The option of including gravity in the heat transfer model must be specified by the ANSYS user. When modeling the flow of a spacecraft in low Earth orbit (LEO), there is an approximate total gravitational force of 9m/s^2 . LEO is traditionally defined as being 100km to 2,000km above the Earth's surface. We can calculate the gravity as

$$m_{sat}g = \frac{Gm_E m_{sat}}{R^2} \rightarrow g = \frac{Gm_E}{R^2}$$

21

where G is the Universal Gravitational Constant, $6.67384 \times 10^{-11} \text{ m}^3\text{kg}^{-1}\text{s}^{-2}$, $m_E m_{sat}$ is the product of the mass of Earth and the mass of the 3U satellite and R is the distance between the center of the two bodies. The actual values of gravity in LEO ranges from 9.5 m/s^2 to 5.6 m/s^2 at altitudes of 100km to 2000km. ANSYS FLUENT allows for this to be easily changed as an input value of the analysis model.

5 – ANSYS Fluent Thermal Analysis 2-Dimensional Models

5.1 – Model 1: Two-Dimensional Simplified

5.1.1 – Modeling Assumptions

To start off the analysis of the system, a two-dimensional simplified model was created as shown in Figure 19. This model was used to verify that the model and setup for the problem are all entered correctly. The purpose of this preliminary model was to create the most basic version of the system that could guide further analysis. This starting model allowed for the testing of boundary conditions and to have a baseline to ensure that the proper inputs were being utilized.

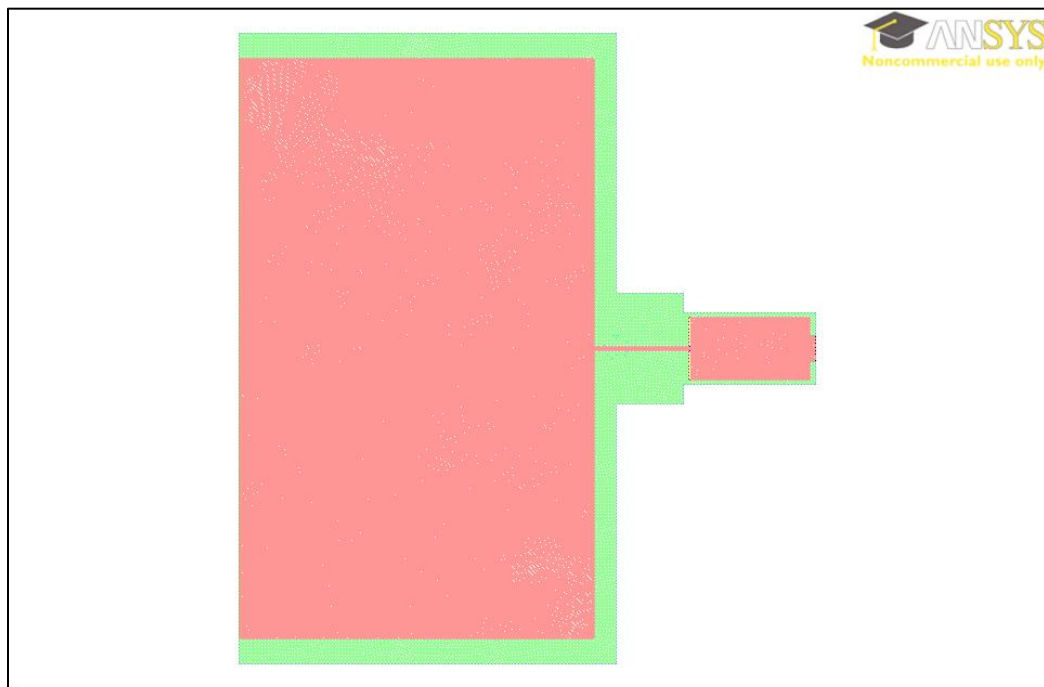


Figure 19. ANSYS ICEM Mesh of the Simplified Model.

5.1.2 – Model Setup for the Simplified Case

This model includes two primary zones, or materials. One of the zones is the propellant, which is modeled as hydrazine. In order to simplify the remaining structure,

there is one external wall that goes around the entire boundary of the system. This merges together the welds that would be present for separate parts, and therefore reduces the number of interfaces. This is possible because the material used in the barrier and combustion chamber is all stainless steel. Overall, this simplifies the model due to the fact that these interfaces are difficult to model. Also, the conduction throughout the interior of the system allows for heat to transfer through those interfaces when they are modeled. This model assumes that the pipe that flows from the tank into the combustion chamber is straight and that it has an inner diameter of 0.025in.

In order to model the reaction of the thruster, two thin plates were put inside the entrance of the combustion chamber and those are used as heat source. They are set to a constant temperature of 845°C. These plates can be seen in the closer view of the mesh in Figure 20.

The model doesn't include the nozzle in this preliminary analysis. The main thermal concern in this system is the temperature of the propellant in the tank in order to prevent accidental reactions. Therefore it is unnecessary to consider the system on the opposite side of the main heat source, which is the combustion chamber.

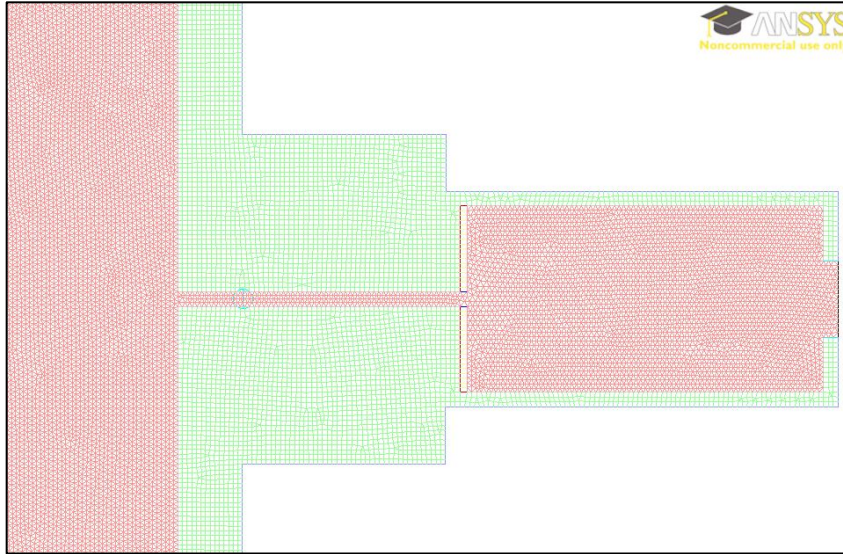


Figure 20. ANSYS ICEM Mesh of the Simplified Model in a Zoom View.

5.2 – Model 2: Two-Dimensional Realistic

This model separates the system into all of the individual zones that are present. This means that every wall and interface throughout the system is modeled individually and therefore can have unique boundary conditions. In addition, the system can now be modeled to represent various design considerations. These include the material used each section of the system, the duty cycle of the burns and the external environment that is being applied across the system.

5.2.1 – Modeling Assumptions

Even with a more realistic model and approach, critical assumptions still need to be made to successfully model this system and environment through the solver. The assumptions that were made for this model include that the representation of the model with no flow out of the nozzle. This allows for the primary heat transfer to be focused on the conduction between the materials. This model allows for no heat transfer out of the system, while still allowing for external effects to enter the system. Another assumption

is that the worst-case scenario for environmental conditions is when the spacecraft is in the sun. This can be modeled by setting the temperature that the external wall feels from the radiation at 398K. Lastly, the entire combustion chamber is set to 845°C (1120K) which is the steady state burning temperature of a hydrazine reaction. This assumes that the heat of the burn instantaneously reaches all of the internal walls of the combustion chamber.

Data from past test-fires of similar thrusters with the same type of catalyst allowed for us to see the time that it takes for hydrazine to reach this temperature (8). The near-immediate jump to this temperature allowed for the Stellar Exploration, Inc. to make the conservative assumption that it can just start at this temperature and burn from there. These assumptions allowed for the system to be modeled to most accurately represent the actual environment through ANSYS FLUENT. This mesh is shown in Figure 21.

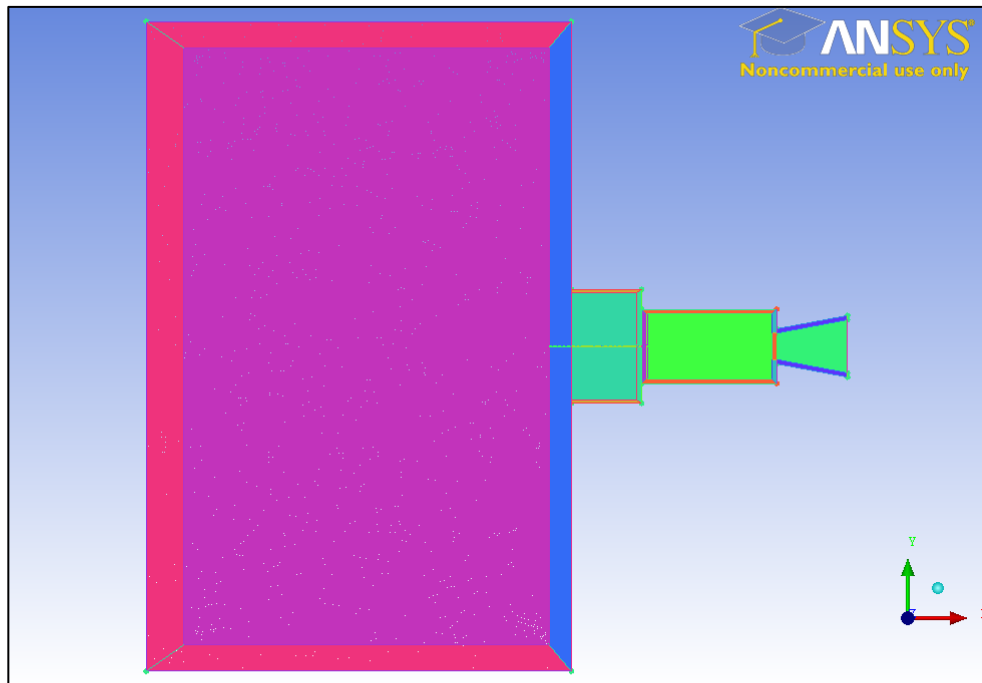


Figure 21. ANSYS ICEM Mesh of 2-Dimensional Model.

5.2.2 – Model Setup

This model setup is more complex throughout the entire process. Due to the fact that numerous walls were overlapping each other, it was necessary to input walls as interfaces and then manually go in and couple those walls together. If these walls were not coupled together properly, then conduction would not occur through them. This is easy to notice by running a sample calculation and ensuring that the heat transfer is not stopping at any particular wall.

For this model, the temperature to represent the heat of radiation was modeled along the exterior walls to provide the worst case scenario. This helps to see all of the impacts that are happening to the system. For this model, different materials were tested for different lengths of burn time. This is done to ensure that the burns needed for the mission can be achieved. Further details regarding the ANSYS Input Values can be found in APPENDIX B- ANSYS Input Values.

6 – Results

This section discusses the different results that have come from the thermal analysis of the hydrazine monopropellant micropropulsion system. These models differ with material, simplicity of design and boundary conditions applied as described in the previous section.

6.1 – Model 1: Simplified 2-D Model

The results of the first model were intended to be utilized as a preliminary design consideration for this analysis. The heat transfer that occurs through the different materials in the basic geometry of the system can be observed. These results determined how much concern there was for potential of excessive heat transfer into the propellant tank.

6.1.1 – Model with Stainless Steel Barrier

The first model that was analyzed was the simplified 2-D model with the exterior wall of the system made of stainless steel. This system is a close representation of what the heat transfer within the system could be if the barrier between the combustion chamber and the propellant tank was made with solid stainless steel. The thermal conductivity of stainless steel is considered to be low. This should reduce the amount of heat transferring into the tank of this system from the reaction in the combustion chamber.

While the lower rate of heat transfer into the propellant tank is beneficial to sustaining the temperatures needed, there are still some critical concerns with this system. Figure **22** demonstrates that even with the low thermal conductivity of the stainless steel, there is still significant heat transfer into the propellant tank through the barrier. At 50

seconds of burn time, temperatures exceed over 800K in the propellant tank. This is beyond the auto-ignite temperature of hydrazine propellant.

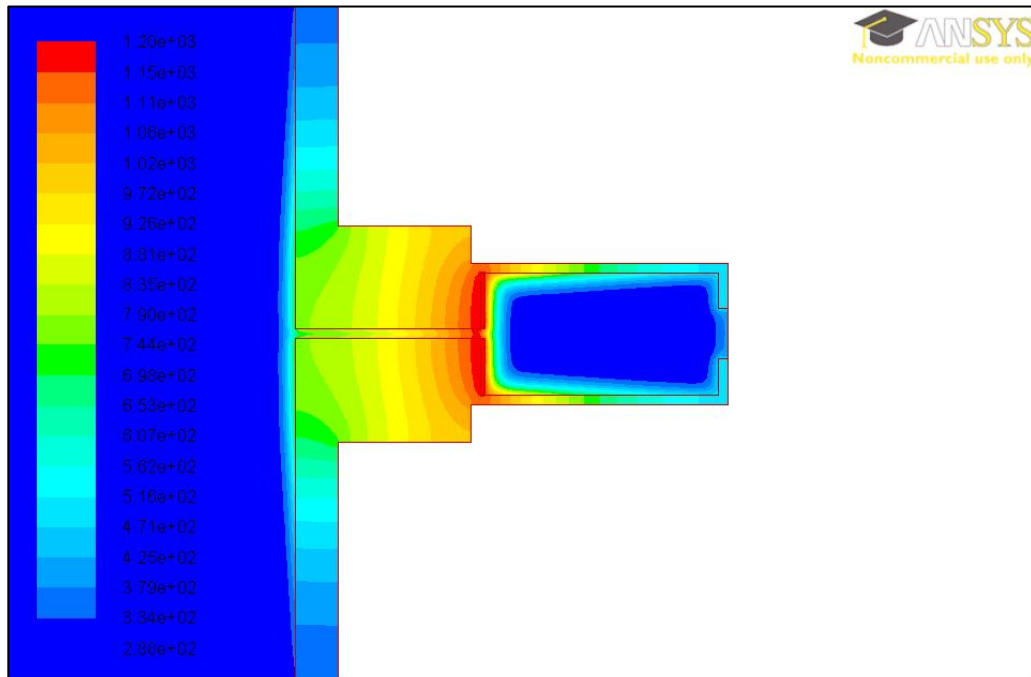


Figure 22. Contours of Total Temperature with Stainless Steel Walls after 43 seconds of Burn Time. (in K)

Figure 23 shows a closer view of the system, focusing on the heat transfer through the barrier. This proves that alternative options need to be investigated, such as having a hollow barrier between the combustion chamber and the propellant tank. This would allow for the space environment to fill that gap and create an environment with essentially no conduction of the reaction heat.

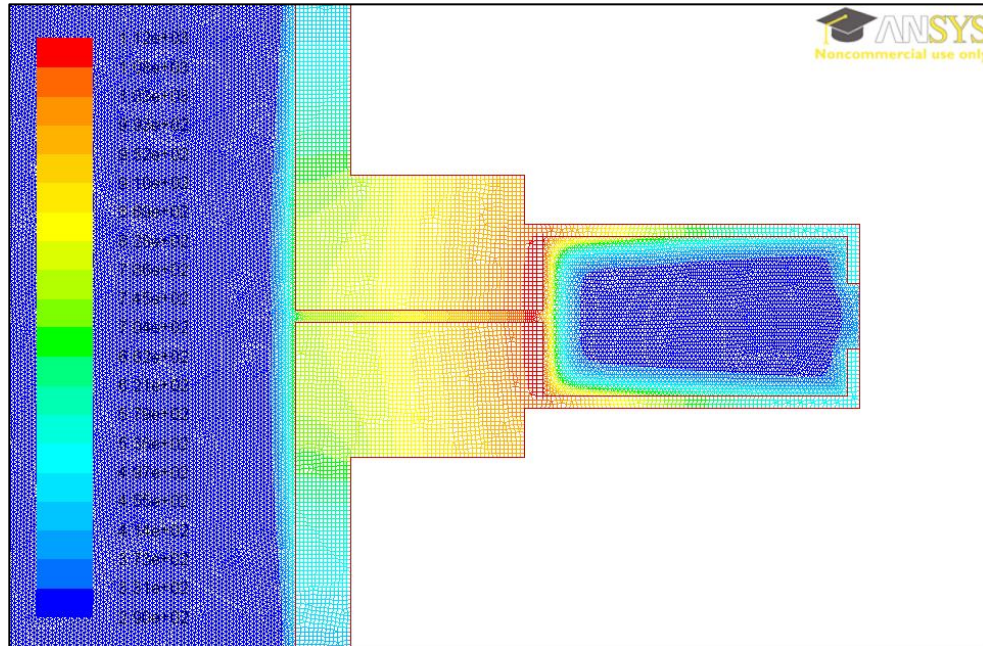


Figure 23. Close view of Contours of Total Temperature with Stainless Steel Walls after 50 seconds of Burn Time (in K).

Figure 24 shows maximum temperature across the interior wall of the propellant tank over time. In this figure, the maximum temperature of the propellant increases continually throughout the burn. The heat of the tank wall is still reaching temperatures of close to 800K at a 50 second burn. Further analysis showed that while having short burns would decrease the temperature of the system, these temperatures would still quickly transfer through the solid barrier and into the propellant tank.

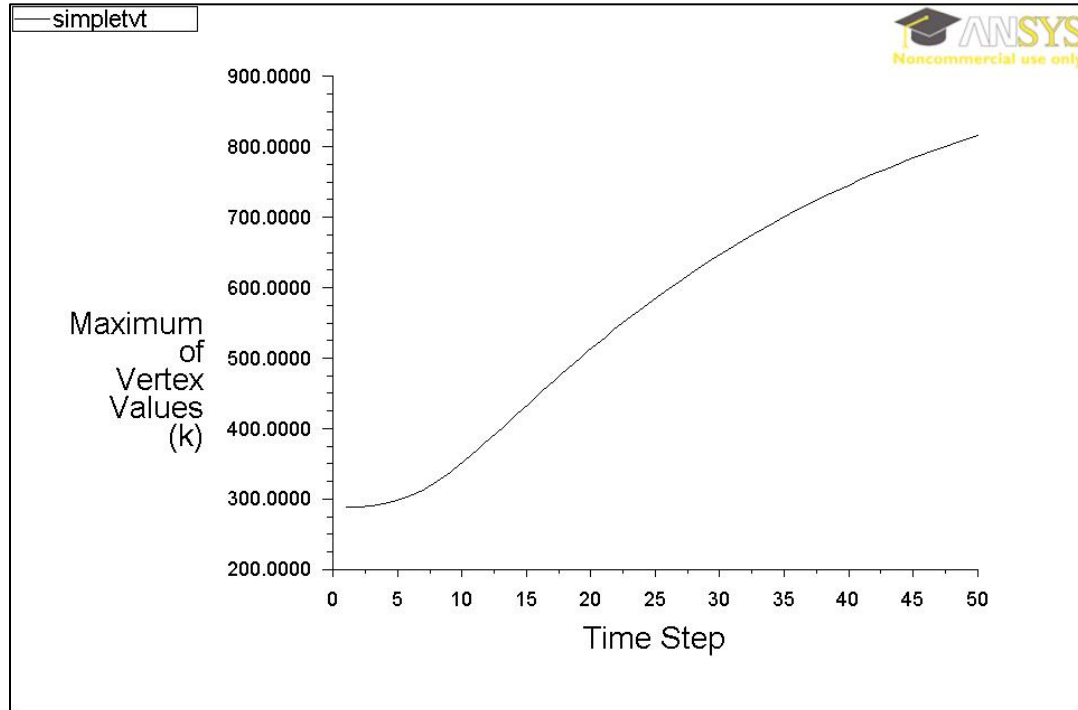


Figure 24. Maximum Temperature Value of the Propellant in the Tank with Stainless Steel Walls. (in K)

6.1.2 – Model with “Air” Barrier

Due to the high level of heat transfer through the solid stainless steel barrier, a non-realistic model was considered to preliminarily examine the impact of a solid barrier versus a hollow barrier. This model took this basic design and replaced the wall with “air” to see the amount of heat transfer that would occur with the minimal conduction that would be allowable. Figure 25 shows the results of this analysis and the total temperatures that were present after a 43 second burn time.

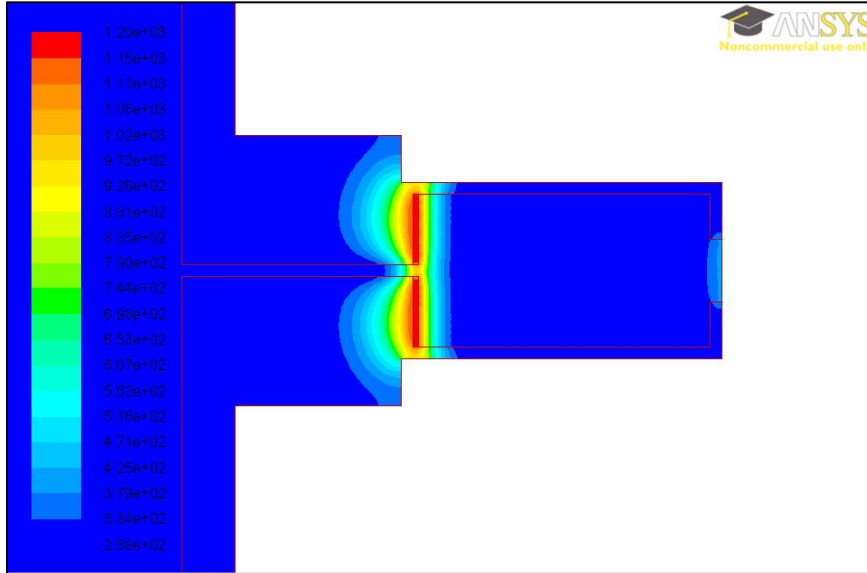


Figure 25. Contours of Total Temperature with Air Barrier after 43 seconds of Burn Time. (in K)

This model shows the dramatic impact of having a portion of the system that has less conduction throughout it. While this is unrealistic and does not allow for the basic stainless steel structures that would still be needed, it shows that the burn is much more achievable under a design that takes this into account.

6.1.3 – Model with Alumina Silicate Barrier

Lastly, the simplified model was used to consider the impact of using a solid thermally resistant material. Alumina silicate was selected as an option due to its resistance to high temperature and its machinability. The contours of this model are seen in Figure 26.

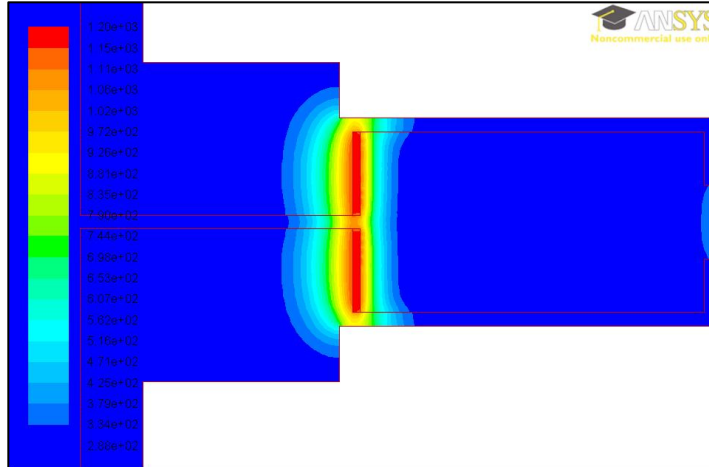


Figure 26. Contours of Total Temperature with Alumina Silicate Walls after 43 seconds of Burn Time. (in K)

The results of the simplified model maximum propellant temperatures in the tank are shown in Table 7. This demonstrates that the tank propellant temperature in the system with stainless steel quickly increased over the auto-ignition temperature of hydrazine. In contrast, the systems with air and alumina silicate have close to no heat transfer into the tank.

Table 7. Simplified Model Results with Maximum Propellant Temperature.

Barrier Material	Model Type	Time of Burn	Max. Propellant Temp.
Stainless Steel	Simplified	1 sec	288.38K
Stainless Steel	Simplified	12 sec	381.90K
Stainless Steel	Simplified	20 sec	512.60K
Stainless Steel	Simplified	43 sec	769.41K
Stainless Steel	Simplified	50 sec	816.83K
Air	Simplified	1 sec	288.16K
Air	Simplified	12 sec	288.16K
Air	Simplified	20 sec	288.16K
Air	Simplified	43 sec	288.16K
Air	Simplified	50 sec	288.16K
Alumina Silicate	Simplified	1 sec	288.16K
Alumina Silicate	Simplified	12 sec	288.16K
Alumina Silicate	Simplified	20 sec	288.16K
Alumina Silicate	Simplified	43 sec	288.16K
Alumina Silicate	Simplified	50 sec	288.16K

Going into the complex model of this system, it was determined that having a material with little to no conduction will dramatically impact the results of the heat transfer. This can either be accomplished with a hollow barrier that can fill with space environment or an insulating material placed between the combustion chamber and propellant tank.

6.2 – Model 2: Two-Dimensional Complex

The next model uses the information from the original simplified models, and creates a more realistic model with all of the correct wall thicknesses throughout the system. This allows for more variation of materials throughout each part of the model. It also allows for the input of correct boundary conditions to make a more realistic model for the conditions that the system will experience in space.

6.2.1 – Model with Reaction in “Heat Source Plates”

This model considers that there is a heat source reaction in very thin plates at the base of the combustion chamber. These heat plates are at the steady state reaction temperature of hydrazine for the duration of the burn. These models utilize liquid hydrazine as the propellant throughout the system, aluminum as the material of the tank walls and stainless steel as the material of all of the other walls within the thruster and barrier.

Figure 27 shows the progression of the heat transfer that occurs throughout the system with thin plates serving as the heat source. The conduction throughout the stainless steel wall of the barrier dramatically impacts the temperatures that are entering into the tank. The heat moving through the wall impacts the air that is in the barrier. In these models, the temperature in the aluminum wall of the propellant tank is maintained

below 300K. This keeps the propellant temperature in a very safe range for storage during flight. However, this model does not take into account the heat that would be added into the system due to radiation while in space. This environmental effect will be added in the next iteration of the model.

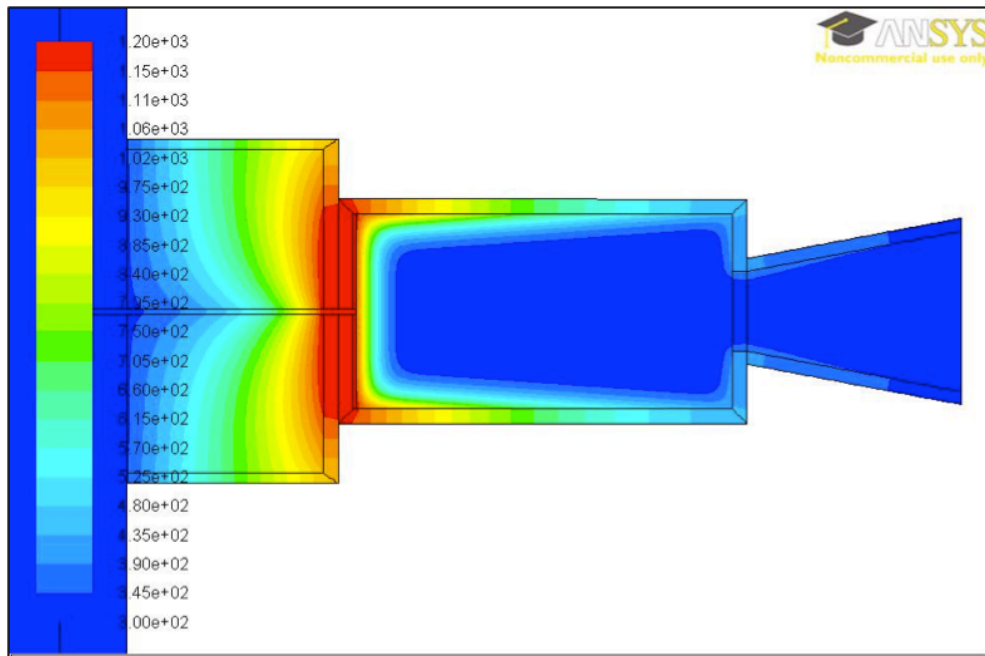


Figure 27. Contours of Total Temperature with Heat Plates after 40 seconds of Burn Time. (in K)

6.2.2 – Model with Reaction in the Entirety of the Combustion Chamber

In order to create a more realistic model, the next model includes the reaction of propellant throughout the entirety of the combustion chamber. The entire chamber will maintain the steady state heat of the reaction throughout the time of the burn. Also, these models now include the impacts of varying external and radiation environments.

Figure 28 shows the design with the solid stainless steel barrier in order to demonstrate the more realistic heat transfer that will occur throughout the system. This demonstrates the heat transfer that occurs when in the most extreme environmental

condition. In this model, the propellant tank is experiencing temperatures reaching up toward 400K. This again demonstrates the extreme heat conditions that are present in this system when in the most extreme environment for heat that was modeled as 398K.

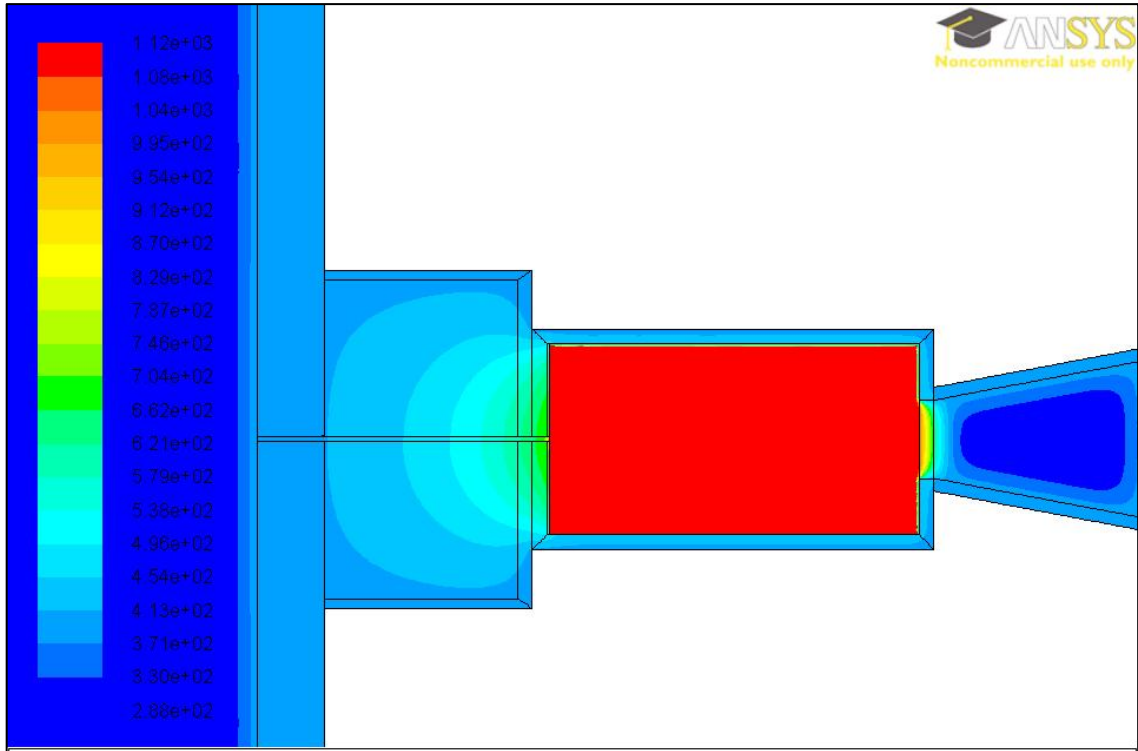


Figure 28. Contours of Total Temperature with Solid Stainless Steel Barrier after 43 seconds of Burn Time in a Hot Environment. (in K)

These contours are shown in greater detail in Figure 29, which zooms into the combustion chamber and propellant feed pipe.

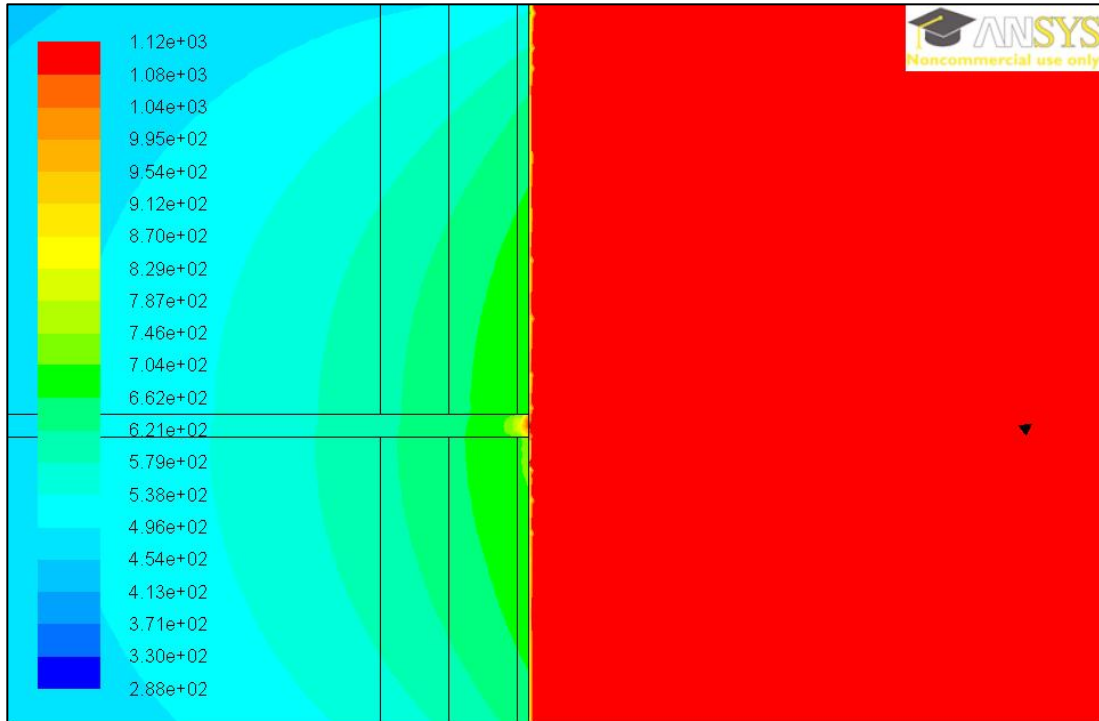


Figure 29. Zoomed View of Contours of Total Temperature with Solid Stainless Steel Barrier after 43 seconds of Burn Time in a Hot Environment. (in K)

Figure 30 shows the maximum propellant temperatures throughout the entire 43-second burn. The temperature increases instantaneously and then continues to grow once the heat of the reaction reaches the tank. This helps to justify that a solid barrier between the source of the heat and the propellant is not an acceptable solution if the burn will be occurring in the highest thermal space environments.

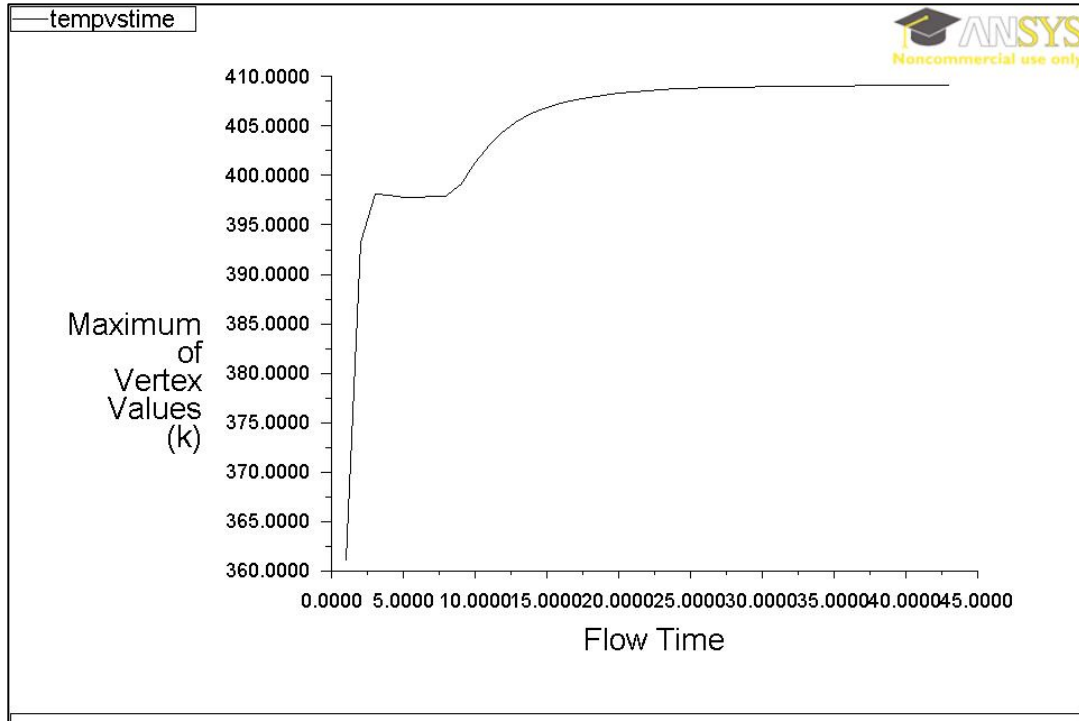


Figure 30. Maximum Temperature of the Propellant throughout the Burn Time in a Hot Thermal Environment. (in K)

Due to the extreme temperatures that were being considered, this analysis was conducted under variable thermal environments. Figure 31 and Figure 32 consider a solid stainless steel barrier during a 43 second burn in the extreme cold space environment which is modeled as 115K (16). These conditions without additional heaters in the propellant tank will cause the propellant to drop down below its freezing temperature of 275K (7).

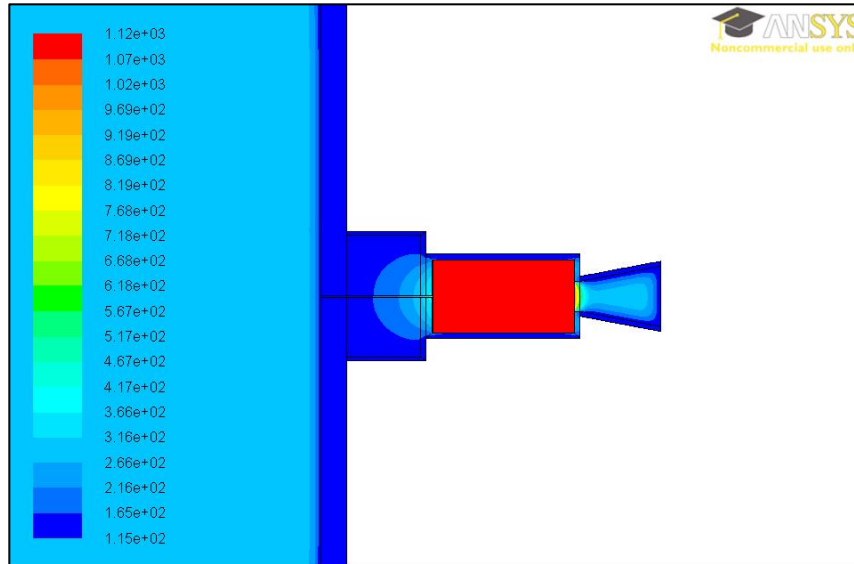


Figure 31. Contours of Total Temperature with Solid Stainless Steel Barrier after 43 seconds of Burn Time in a Cold Thermal Environment. (in K)

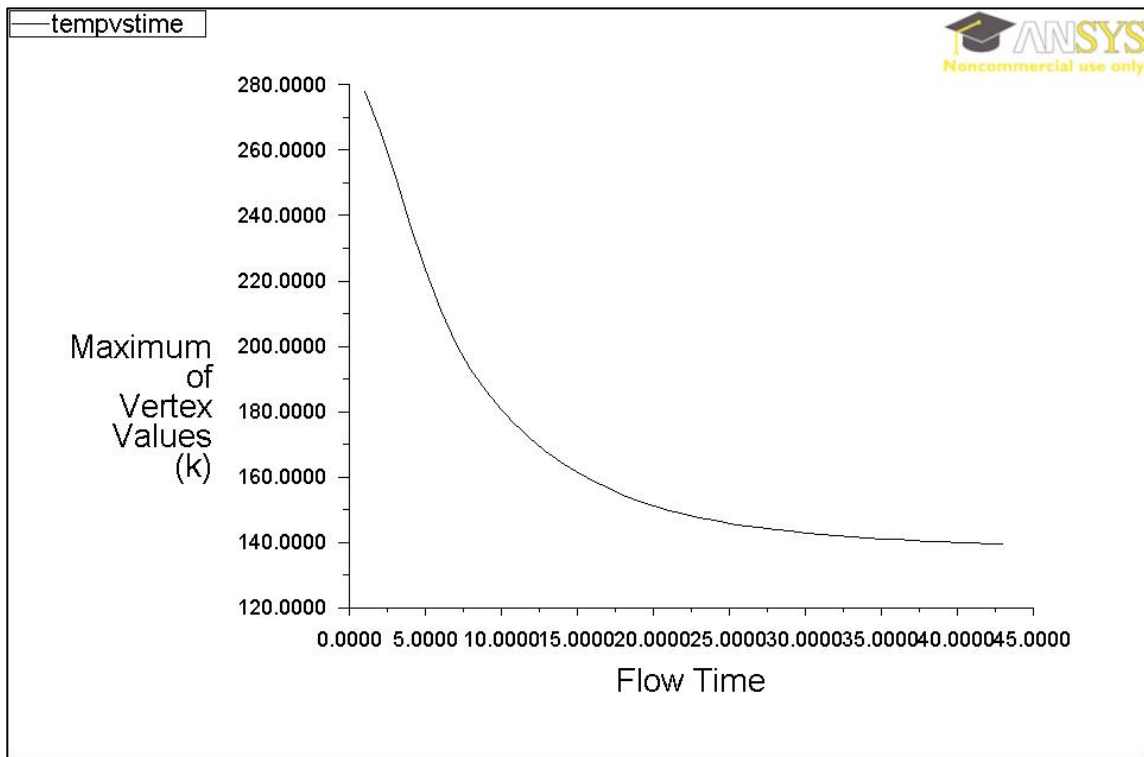


Figure 32. Maximum Temperature of the Propellant throughout the Burn Time in a Cold Thermal Environment. (in K)

Lastly, the same analysis is considered in a mid-range temperature seen by CubeSats of 273K. This temperature represents an approximate middle ground of the temperature that the CubeSat would see in orbit (16). Figure 33 and Figure 34 demonstrate the heat transfer that is present in this middle-ranged external thermal environment. This allows for the temperature of the propellant to reach a steady state at 287K. This temperature remains within the acceptable storage temperature for hydrazine. This mid-range thermal environment lends itself well to performing all of the burns that are necessary to complete the mission with minimal concerns.

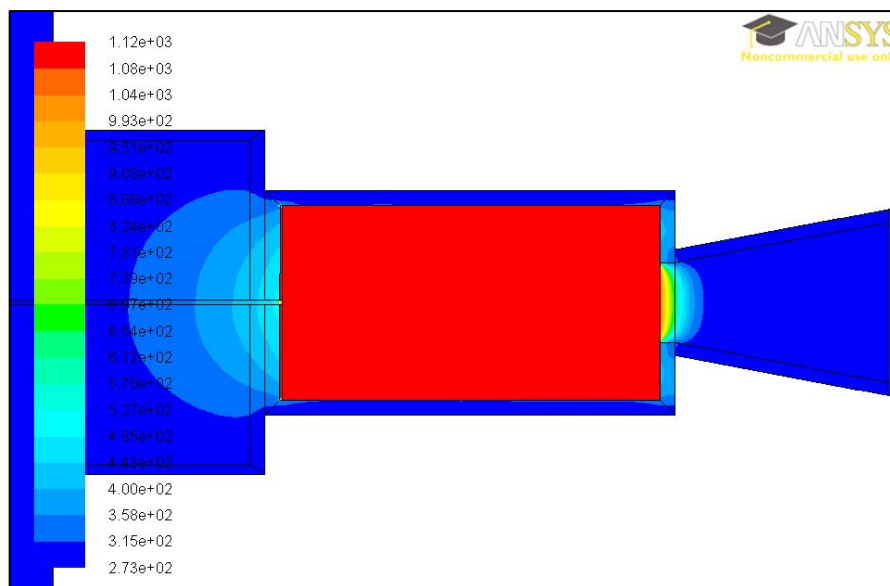


Figure 33. Contours of Total Temperature with Solid Stainless Steel Barrier after 43 seconds of Burn Time in a Mid-range Thermal Environment. (in K)

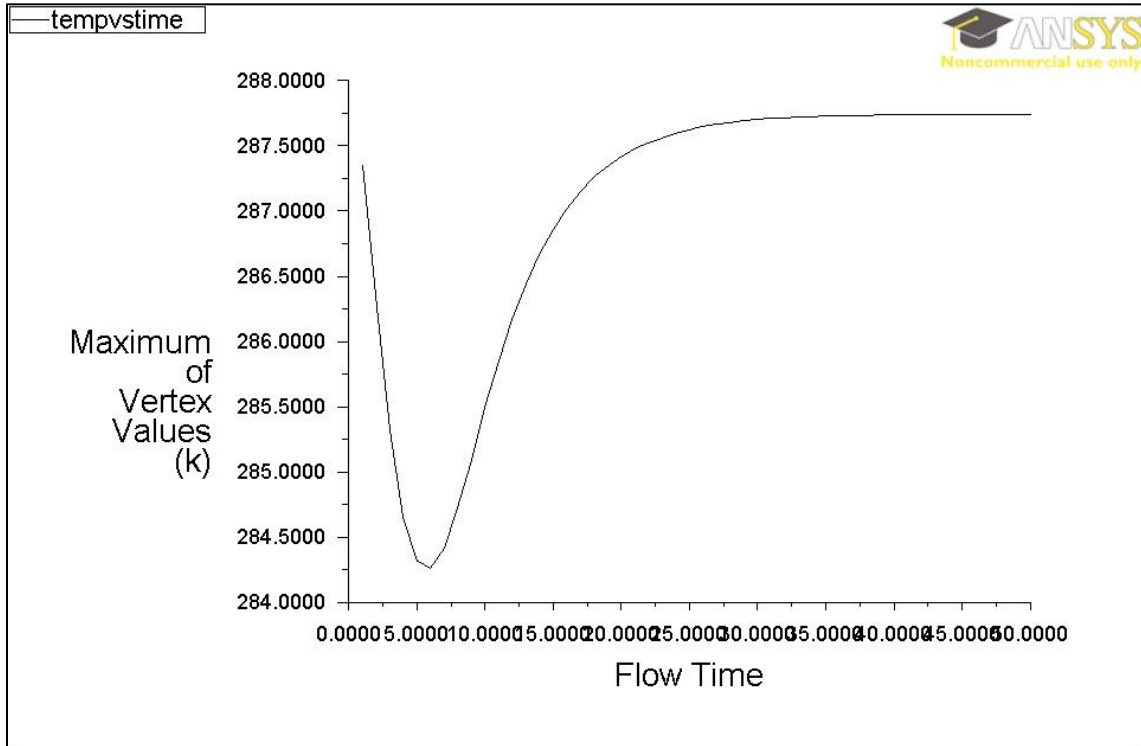


Figure 34. Maximum Temperature of the Propellant throughout the Burn Time in a Mid-range Thermal Environment. (in K)

Table 8 compares the temperatures for different burn times in different external thermal conditions. While in the extreme thermal environments, the propellant reaches their respective extreme temperatures in the tank in less than five seconds. This shows that at varying thermal environments, the propulsion system can successfully perform all of the burns needed for this mission.

Table 8. Maximum Temperature Comparisons for a Solid Stainless Steel Barrier.

Barrier Material	Time of Burn	Maximum Propellant Temp. (Sun)	Maximum Propellant Temp. (Dark)	Maximum Propellant Temp. (Mid)
Stainless Steel	1 sec	361.09K	278.08K	287.35K
Stainless Steel	2 sec	393.23K	n/a	n/a
Stainless Steel	3 sec	398.14K	n/a	n/a
Stainless Steel	4 sec	398.00K	n/a	n/a
Stainless Steel	5 sec	397.83K	223.40K	284.31K
Stainless Steel	12 sec	404.43K	171.19K	286.17K
Stainless Steel	20 sec	408.35K	151.21K	287.41K
Stainless Steel	30 sec	408.99K	142.87K	287.70K
Stainless Steel	40 sec	409.12K	139.96K	287.74K
Stainless Steel	43 sec	409.14K	139.48K	287.74K
Stainless Steel	50 sec	n/a	n/a	287.74K

This next section utilizes alumina silicate as the interior of the barrier due to its low thermal conductivity. This shows that while the heat does not transfer quickly through the barrier, there is a lot of concern for the rise in temperature from being in the worst-case radiation model. This radiation creates heat on the surface that is equivalent to 398K. Figure 35 shows the temperature contours that are present in this environment and the impact that it has on the temperature of the propellant. Figure 36 shows a close-up view of the propellant line out of the combustion chamber. This model shows that the heat transfer does not pass directly through the barrier. Instead it comes primarily from the radiation effects and moves along the structural stainless steel walls of the barrier toward the tank.

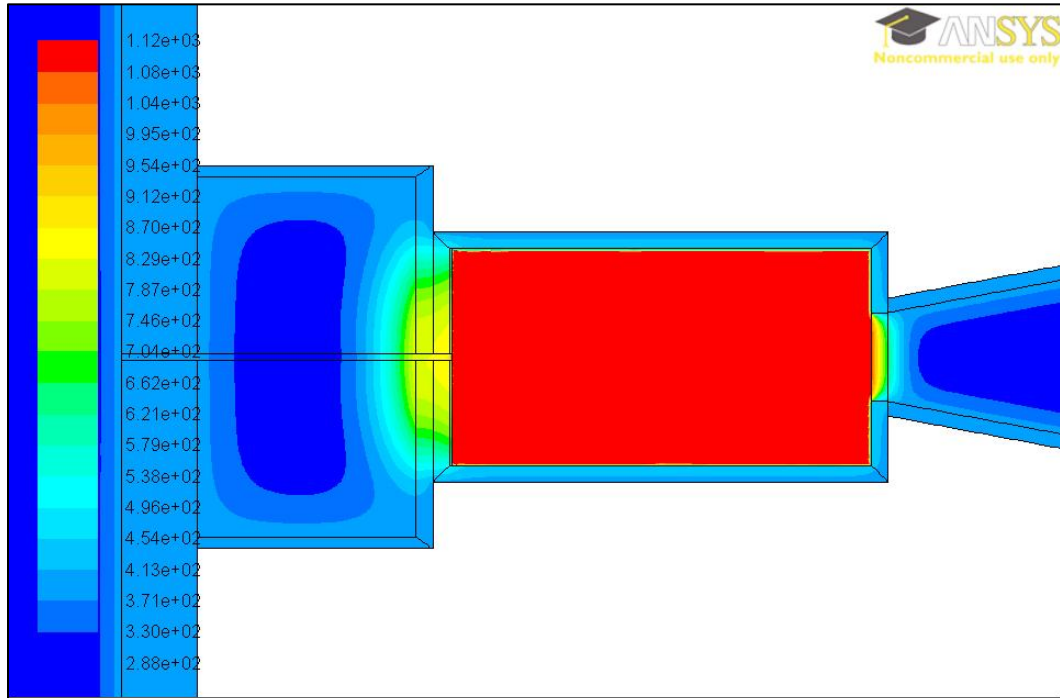


Figure 35. Contours of Total Temperature with Alumina Silicate Barrier after 43 seconds of Burn Time in a High Thermal Environment. (in K)

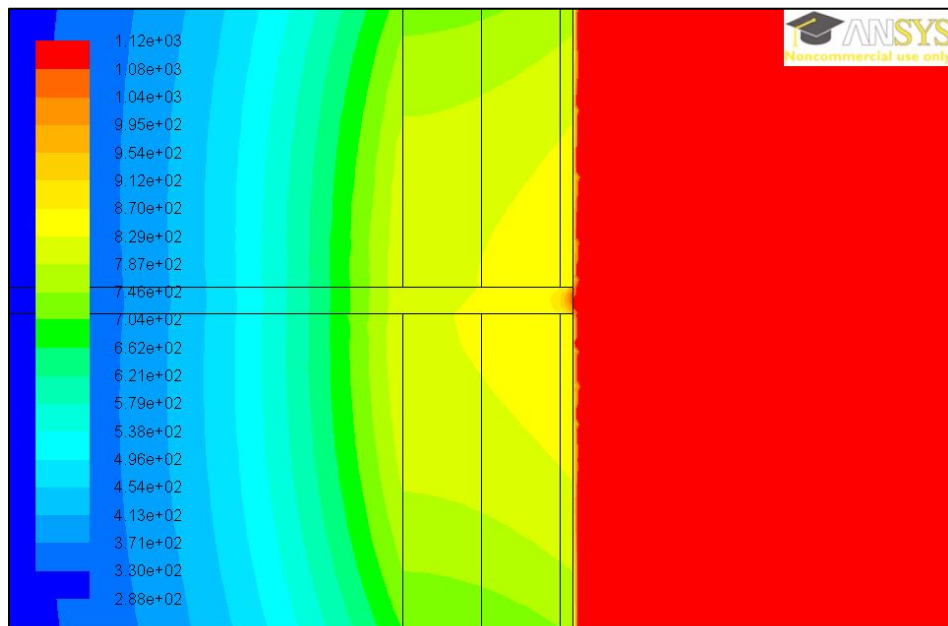


Figure 36. Zoomed View of Contours of Total Temperature with Alumina Silicate Barrier after 43 seconds of Burn Time in a High Thermal Environment. (in K)

Figure 37 considers the maximum temperature of the propellant in the tank and shows that after approximately 3 seconds, the temperature in the tank has increased to reach the external temperature from radiation. This indicates that because of the high thermal conductivity of aluminum, our main heat transfer into the tank is not from the reaction in the combustion chamber, but rather from the environmental heat. While this dramatic increase in temperature is not detrimental to the system, it can be reduced by changing the surface properties of the spacecraft to reduce the radiation.

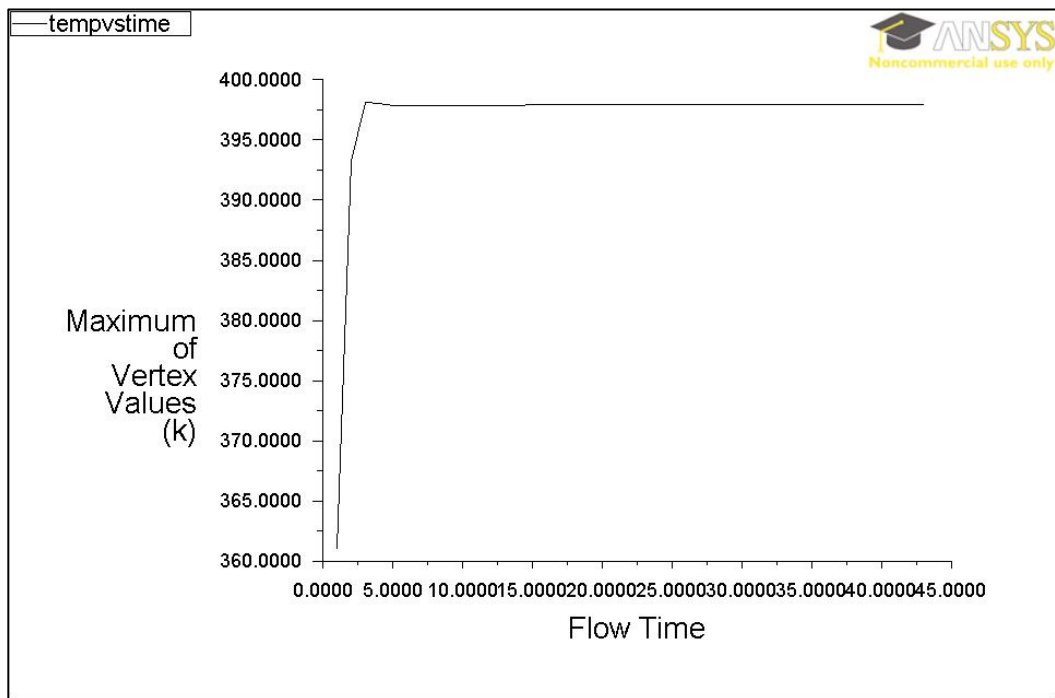


Figure 37. Maximum Temperature of the Propellant throughout the Burn Time in a High Thermal Environment. (in K)

These models were intentionally created to experience different thermal environments while in the orbit that a CubeSat would experience. The trends show that performing the burn in the right space environment is more important than the thermal conductivity of the materials being used. Figure 38 and Figure 39 show that with a barrier with low thermal conductivity, more concern comes from the large amount heat transfer that is

occurring through the walls of the propellant tank. In these models the low temperature is shown, and again the cold temperature transfers straight through the aluminum wall of the tank and into the propellant.

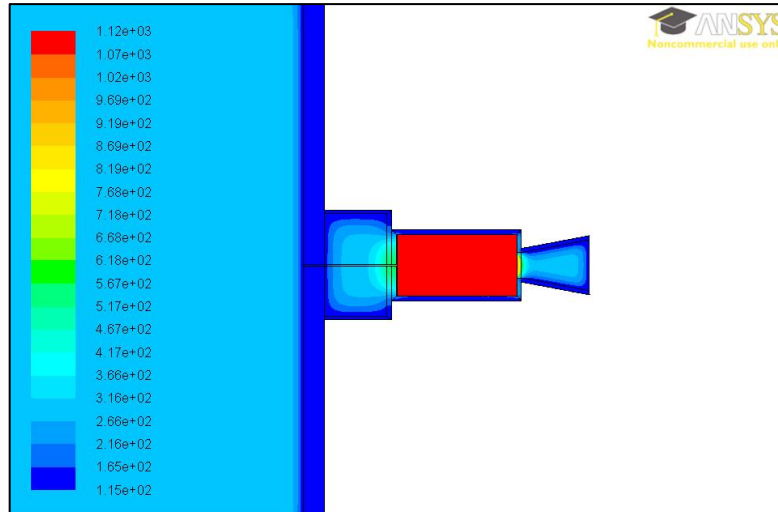


Figure 38. Contours of Total Temperature with Alumina Silicate Barrier after 43 seconds of Burn Time in a Low Thermal Environment. (in K)

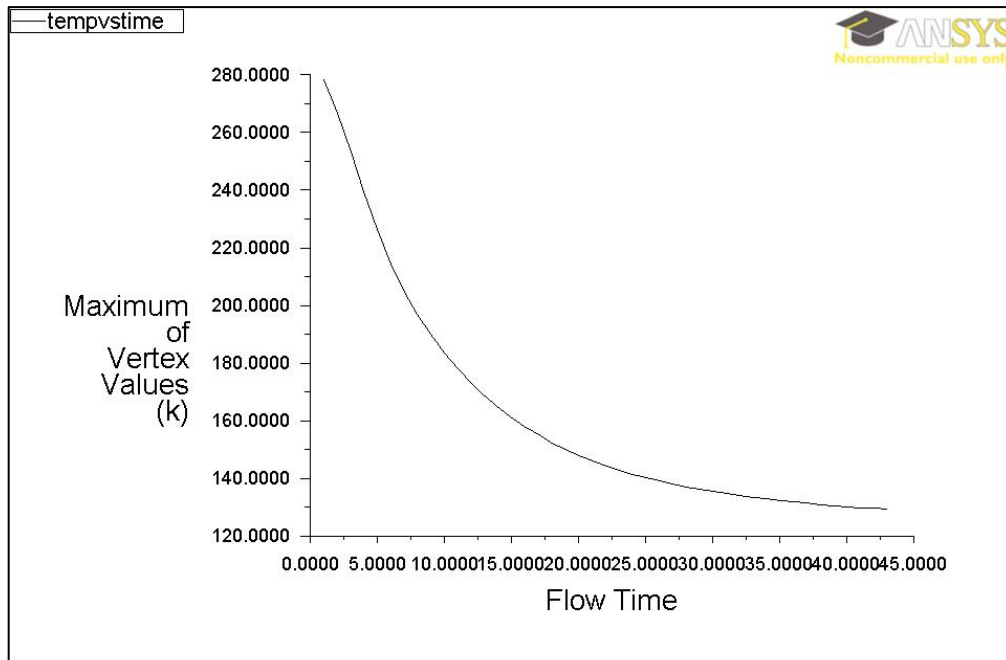


Figure 39. Maximum Temperature of the Propellant throughout the Burn Time in a Low Thermal Environment. (in K)

Lastly, Figure 40 demonstrates that having an ideal, mid-range thermal environment allows for a higher chance of a successful mission. In the figure, the curves show how the heat is moving away from the heat of the reaction. This model also shows the difference in the heat transfer in different materials that are configured together.

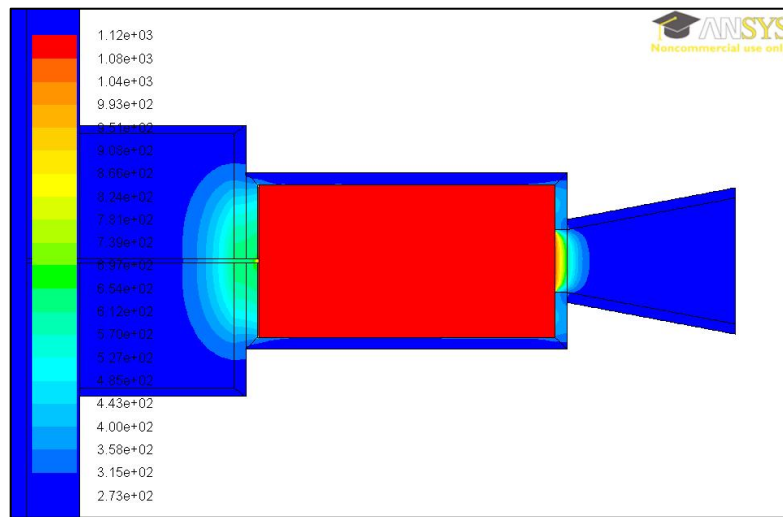


Figure 40. Contours of Total Temperature with Alumina Silicate Barrier after 43 seconds of Burn Time in a Mid-range Thermal Environment. (in K)

As a recap, Table 9 shows the comparison of the maximum temperature values across different burn times for variable external thermal environments. Some interesting comparisons can be made between the solid stainless steel and the solid alumina silicate. A fix that could be made to this system is integrating a heat source into the wall of the propellant tank. This would boost up the tank temperatures that would be on the verge of freezing. Unfortunately with a system that has materials with high insulation, the heat from the catalyst heater does not transfer down to the tank. If this option was considered, a separate heater would be needed near the exterior wall of the propellant tank.

Table 9. Maximum Temperature Comparisons for an Alumina Silicate Barrier.

Barrier Material	Time of Burn	Maximum Propellant Temp. (Sun)	Maximum Propellant Temp. (Dark)	Maximum Propellant Temp. (Mid)
SS Wall/AlSi Barr	1 sec	361.05K	278.34K	287.31K
SS Wall/AlSi Barr	2 sec	393.21K	n/a	n/a
SS Wall/AlSi Barr	3 sec	398.13K	n/a	n/a
SS Wall/AlSi Barr	4 sec	397.95K	n/a	n/a
SS Wall/AlSi Barr	5 sec	397.83K	226.35K	282.79K
SS Wall/AlSi Barr	12 sec	397.89K	173.09K	278.18K
SS Wall/AlSi Barr	20 sec	397.92K	147.95K	276.02K
SS Wall/AlSi Barr	30 sec	397.94K	135.42K	274.90K
SS Wall/AlSi Barr	40 sec	397.95K	130.17K	274.48K
SS Wall/AlSi Barr	43 sec	397.95K	129.23K	274.40K
SS Wall/AlSi Barr	50 sec	n/a	n/a	274.24K

This last model is the most realistic of the models that was analyzed. In this model, the area that is within the barrier is modeled as the vacuum of space. This means that there would be conditions that include virtually no conduction through that region. Additionally, the system is modeled in the three various radiation and external thermal environments- similar to the past models. Figure 41 and Figure 42 show what this model would look like and the route that the heat would transfer through, primarily moving through the walls and the pipe wall. It demonstrates that relatively no additional heat is transferred into the propellant tank from the reaction in the combustion chamber. This model shows that the heat transfer from the combustion chamber is not a concern unless the system is introduced to the worst-case radiation on the metal material surfaces.

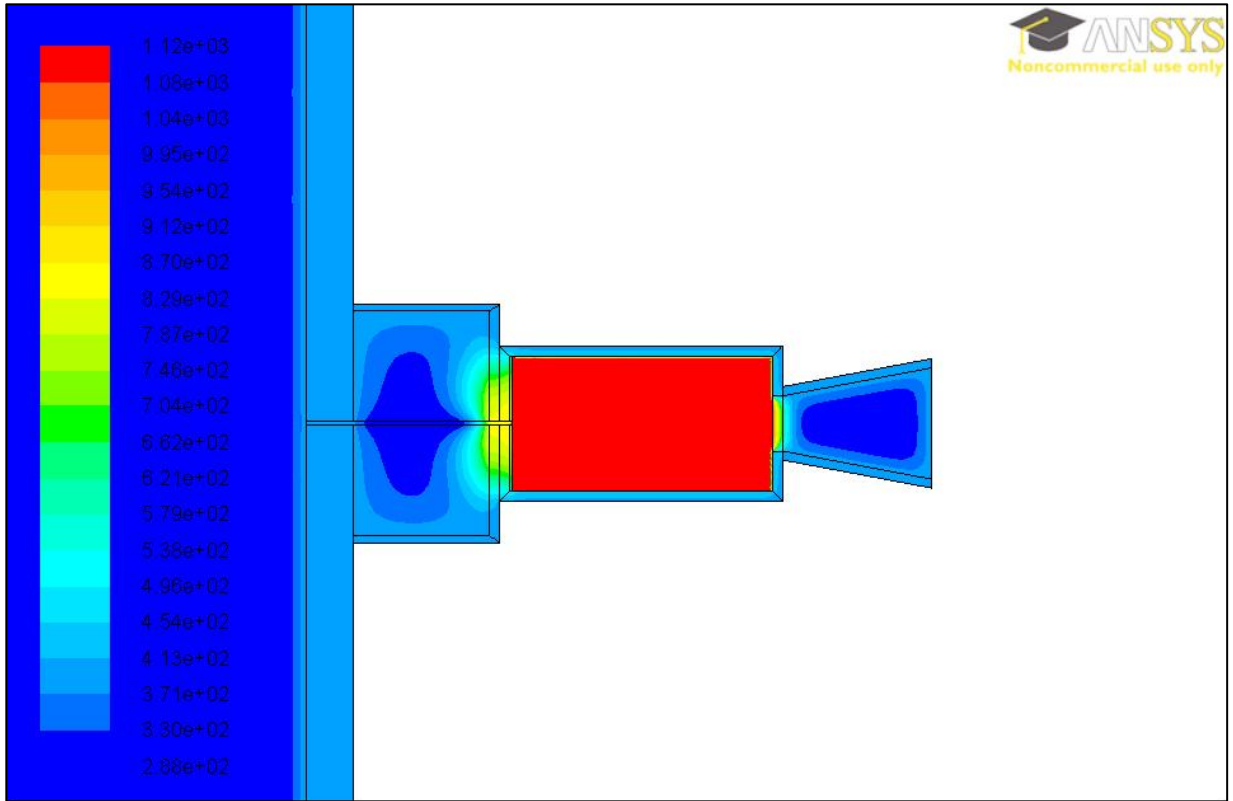


Figure 41. Contours of Total Temperature with Hollow Barrier after 43 seconds of Burn Time in a High Thermal Environment. (in K)

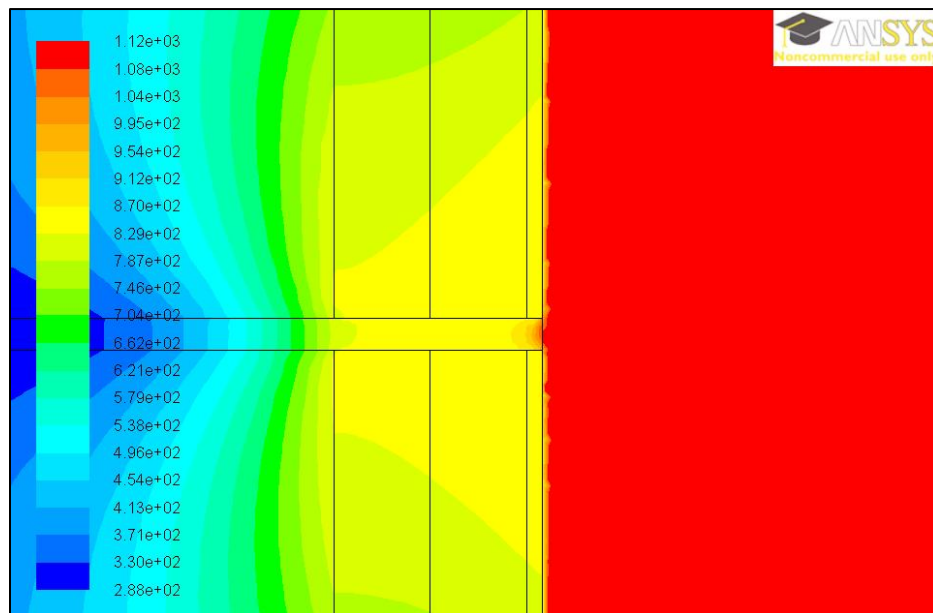


Figure 42. Zoomed View of Contours of Total Temperature with Hollow Barrier after 43 seconds of Burn Time in a High Thermal Environment. (in K)

Figure 43 shows the maximum tank temperature in this hollow barrier design and that it reaches a maximum value of 398K with these conditions. The temperature values increase dramatically over the first 3 seconds and then reach a steady state at the external temperature.

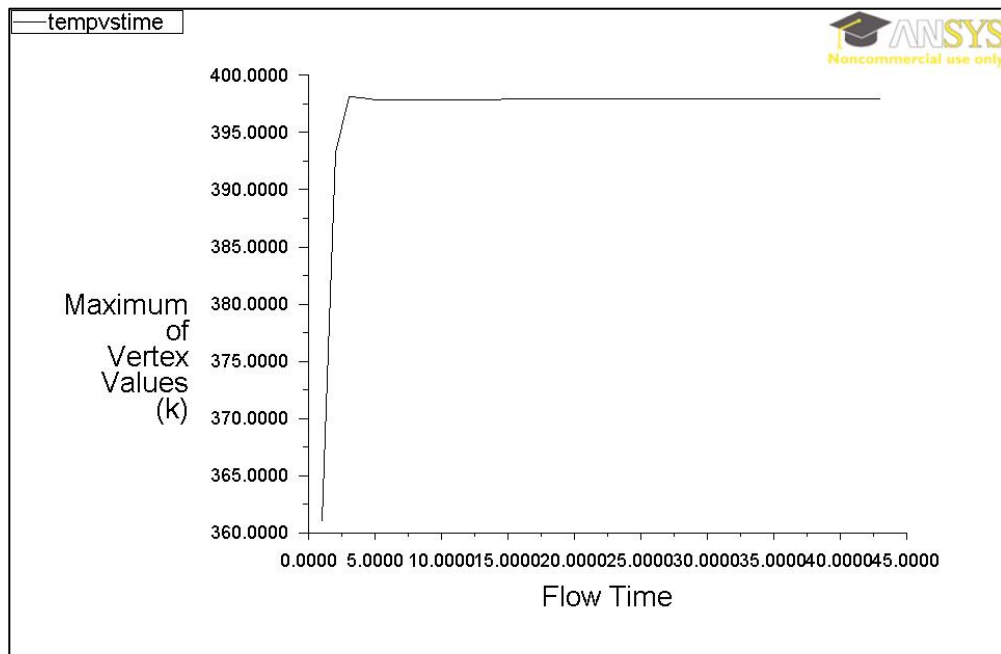


Figure 43. Maximum Temperature of the Propellant throughout the Burn Time in a High Thermal Environment. (in K)

Figure 44 allows for the examination of the transfer of the cold environment into the tank of the system. It appears that the wall of the propellant tank very quickly drops in temperature and this allows for this cold temperature to spread more rapidly through the entire system and the barrier. Figure 45 shows the quick drop in temperature over the time of the burn. This maximum temperature curve is very similar in shape to the curve in the low thermal environment alumina silicate case.

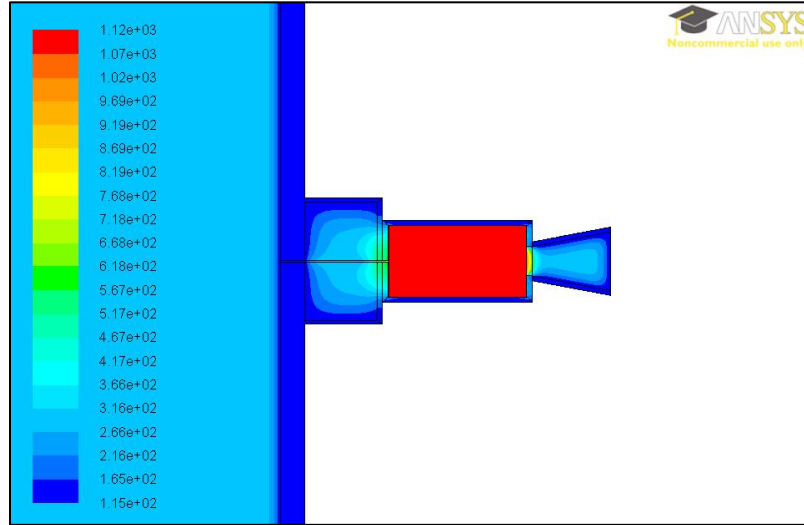


Figure 44. Contours of Total Temperature with Hollow Barrier after 43 seconds of Burn Time in a Low Thermal Environment. (in K)

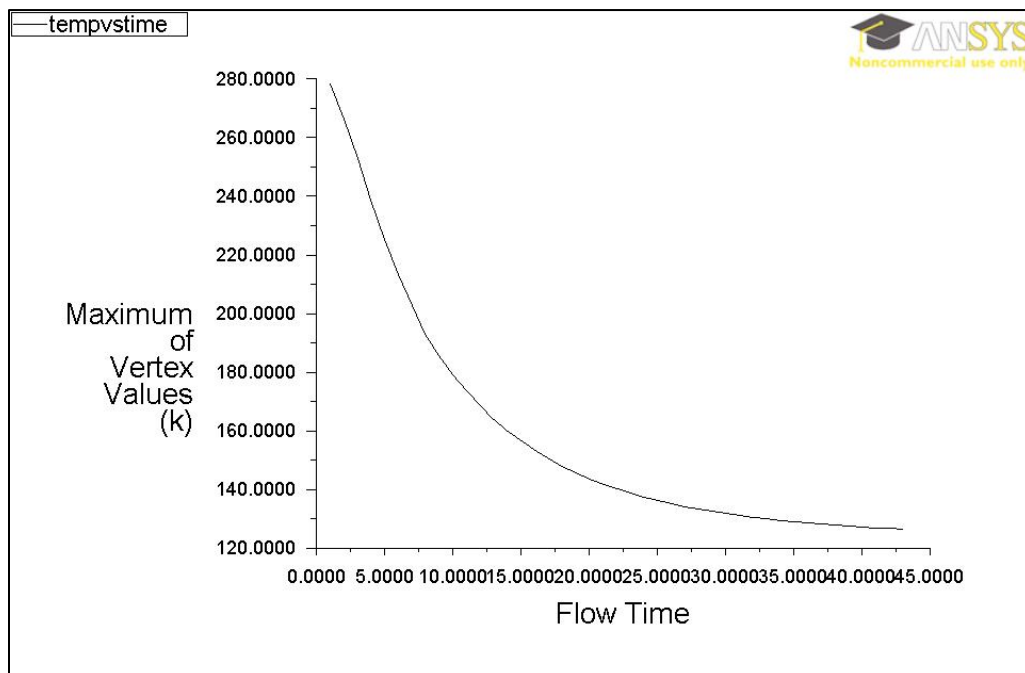


Figure 45. Maximum Temperature of the Propellant throughout the Burn Time in a Low Thermal Environment. (in K)

Figure 46 and Figure 47 provide the one last sample of the heat transfer through the system with a hollow barrier in a mid-range thermal environment. Almost identical to the alumina silicate case, the temperatures drop down slightly below the freezing

temperature of hydrazine. Solutions for nominal heating to the propellant should be looked into in order to allow this design to complete all of the burns that are necessary with no thermal complications.

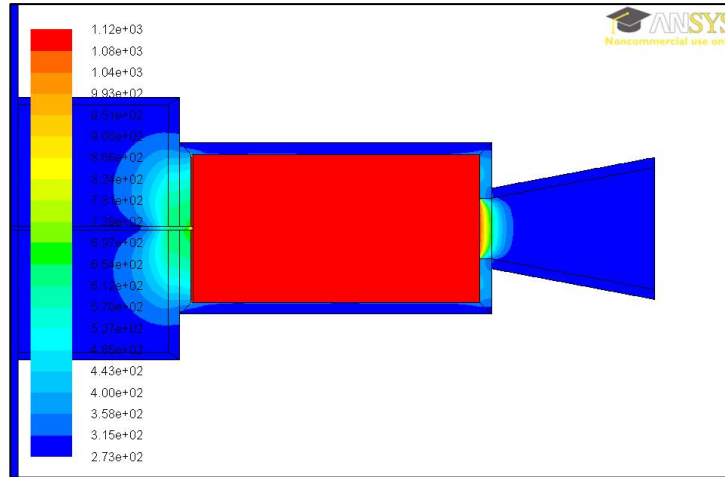


Figure 46. Contours of Total Temperature with Hollow Barrier after 43 seconds of Burn Time in a Mid-range Thermal Environment. (in K)

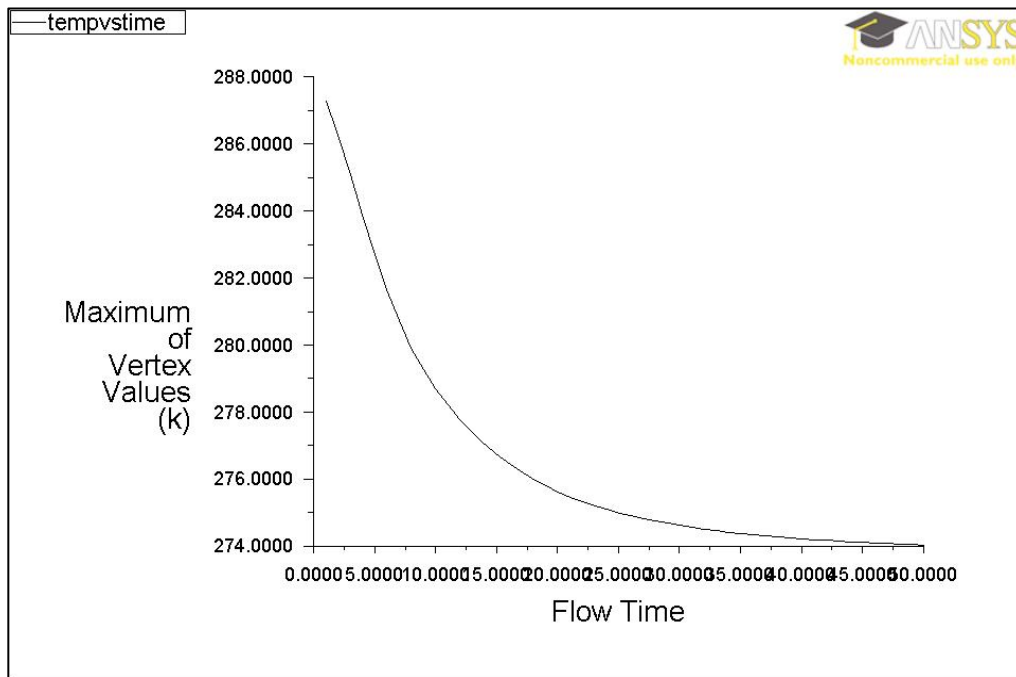


Figure 47. Maximum Temperature of the Propellant throughout the Burn Time in a Mid-range Thermal Environment. (in K)

The results from the case with a hollow barrier are collected and compared in Table 10. Almost identically to the Alumina Silica case, the burns can be achieved through the maximum external temperature. The propellant temperatures closely represent the external temperatures that are experienced. Therefore the propellant is more stable in less extreme heat environments. For the low thermal environment, additional heaters would be needed to heat the propellant approximately 150K. These are not only problems due to the complexity added, but also due to the power that would be needed to make these thermal adjustments to the system. While a heater would be needed to keep the propellant at the proper temperature in the last case, the amount of heat that needs to be added is approximately 1K.

Table 10. Maximum Temperature Comparisons for a Hollow Barrier.

Barrier Material	Time of Burn	Maximum Propellant Temp. (Sun)	Maximum Propellant Temp. (Dark)	Maximum Propellant Temp. (Mid)
SS Wall/Air Barr	1 sec	361.05K	278.21K	287.28K
SS Wall/Air Barr	2 sec	393.21K	n/a	n/a
SS Wall/Air Barr	3 sec	398.12K	n/a	n/a
SS Wall/Air Barr	4 sec	397.99K	n/a	n/a
SS Wall/Air Barr	5 sec	397.83K	225.42K	282.71K
SS Wall/Air Barr	12 sec	397.89K	168.51K	277.78K
SS Wall/Air Barr	20 sec	397.92K	143.60K	275.62K
SS Wall/Air Barr	30 sec	397.94K	131.79K	274.61K
SS Wall/Air Barr	40 sec	397.95K	127.21K	274.22K
SS Wall/Air Barr	43 sec	397.95K	126.42K	274.15K
SS Wall/Air Barr	50 sec	397.95K	n/a	274.03K

6.3 – Model 2: Recap of the overall results

A table is put together that combines all of the results of the cases throughout the varying thermal environments. Table 11 allows for the visualization of the trends in data that are present between the different models. A very short pulse can be achieved with

any of the setups, however a longer burns can potentially lead to thermal complications if not monitored carefully. Remaining aware of the internal and external temperature of the system at the start of each burn will help to increase mission success.

Designing a solid barrier piece out of completely alumina silicate with no stainless steel proves that it would be able to meet the requirements. The only issues that arise are the uncertainties associated with putting the alumina silicate material into the harsh space environment. Table 11 shows the overall results of this analysis under selected conditions. Appendix A includes all of the results collected over time.

Table 11. Overall Results of Burn Times Under Different Conditions.

Barrier Material	Time of Burn	Max. Propellant Temp. (Sun)	Max. Propellant Temp. (Dark)	Max. Propellant Temp. (Ave.)
Stainless Steel	1 sec	361.09K	278.08K	287.35K
Stainless Steel	12 sec	404.43K	171.19K	286.17K
Stainless Steel	43 sec	409.14K	139.48K	287.74K
Barrier Material	Time of Burn	Max. Propellant Temp. (Sun)	Max. Propellant Temp. (Dark)	Max. Propellant Temp. (Ave.)
SS Wall/Air Barr	1 sec	361.05K	278.21K	287.28K
SS Wall/Air Barr	12 sec	397.89K	168.51K	277.78K
SS Wall/Air Barr	43 sec	397.95K	126.42K	274.15K
Barrier Material	Time of Burn	Max. Propellant Temp. (Sun)	Max. Propellant Temp. (Dark)	Max. Propellant Temp. (Ave.)
SS Wall/AlSi Barr	1 sec	361.05K	278.34K	287.31K
SS Wall/AlSi Barr	12 sec	397.89K	173.09K	278.18K
SS Wall/AlSi Barr	43 sec	397.95K	129.23K	274.40K
Barrier Material	Time of Burn	Max. Propellant Temp. (Sun)	Max. Propellant Temp. (Dark)	Max. Propellant Temp. (Ave.)
Alumina Silicate	1 sec	288.29K	X	X
Alumina Silicate	12 sec	289.56K	X	X
Alumina Silicate	43 sec	291.59K	X	X

Overall the case with the Alumina Silicate and the hollow barrier react very similar in the varying temperatures. For the cold environments, a certain level of heat transfer is needed within the system to allow for the system temperature to equalize out. With the alumina silicate and the hollow barrier- there is almost no conduction through this area which means that the warmth from the reaction cannot transfer to the cold areas

of the tank. A potential solution to this could include the addition of a heater around the exterior of the propellant tank.

6.4 – Validation of Results

This section provides the validation for the thermal analysis results that have been provided, while also addresses concerns of the model used. One of the primary concerns was incorrect heat transfer throughout sections of the model. This was corrected by ensuring that all of the proper boundary conditions were identified and entered into the solver.

This issue was noticed due to the unsteady heat transfer moving away from the combustion chamber. Figure 48 shows the steady state heat transfer with a heat source made out of a solid material. This is compared to Figure 49 which is the same conditions, but where the heat source is modeled as a fluid. The wall conditions that occur vary greatly between the solid and fluid heat source. With the solid heat source, the distribution of heat transferring from the combustion chamber toward the tank happens steadily across the barrier. This is different than the case with fluid in the combustion chamber, where the majority of the heat only remains in the surrounding fluid areas.

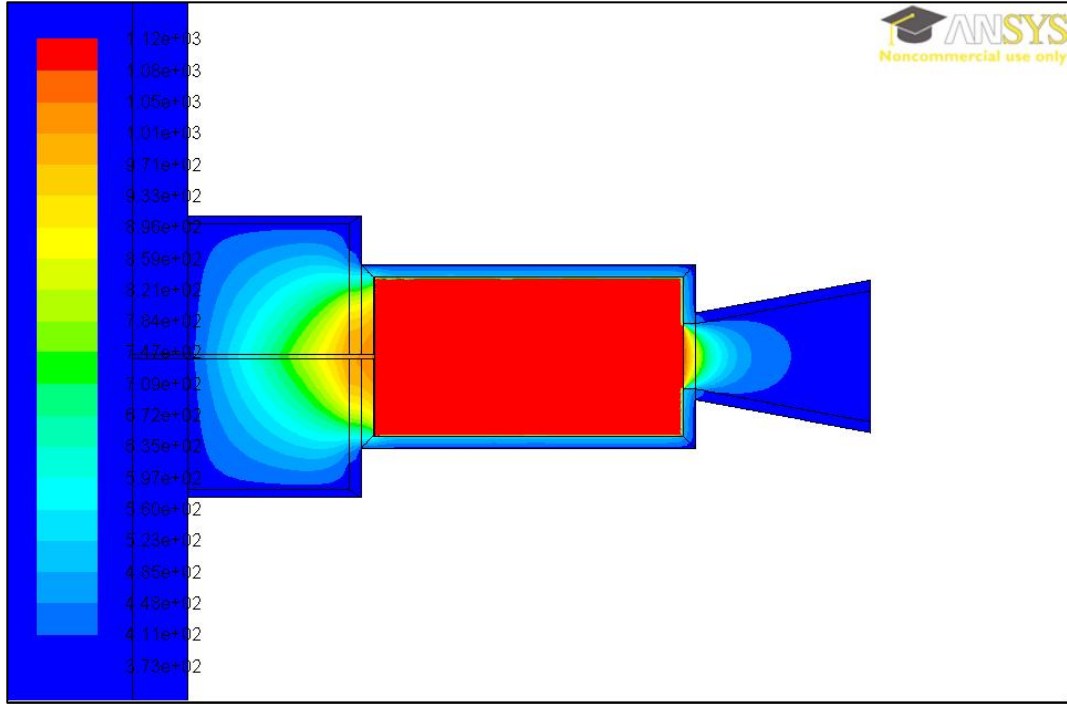


Figure 48. Steady State Heat Transfer through System with Solid Combustion Chamber.

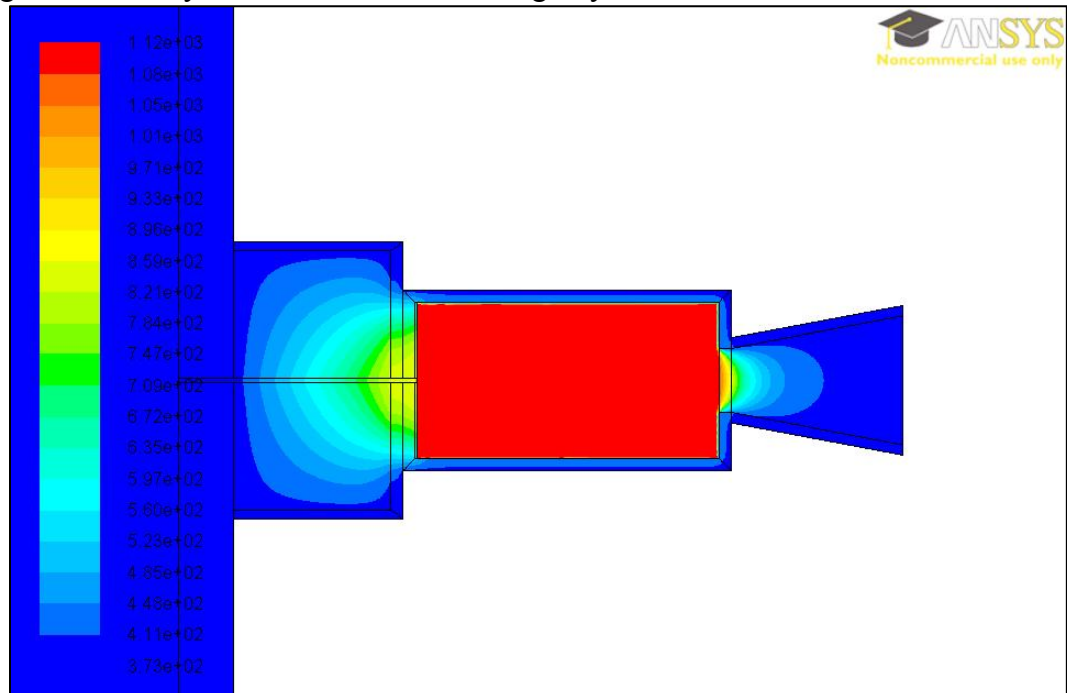


Figure 49. Steady State Heat Transfer through System with Solid Combustion Chamber.

Figure 50 zooms into this area near the wall and shows that a majority of the extreme heat actually decreases before reaching the solid walls.

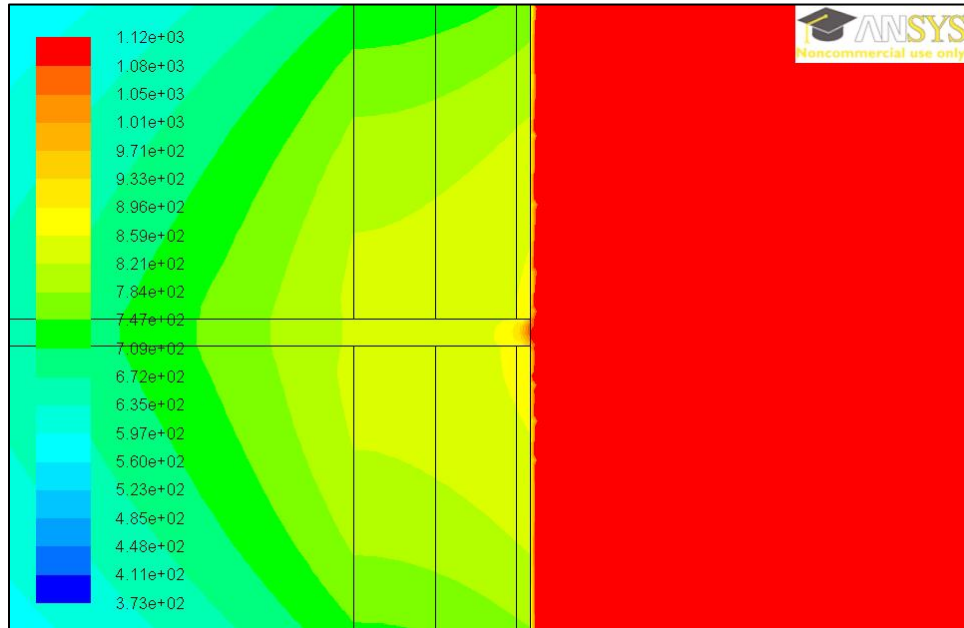


Figure 50. Zoomed View of Steady State Heat Transfer through System with Solid Combustion Chamber.

This section of validation compares the limited test fire data with a model designed to replicate the test environment. Table 12 shows the temperatures that were collected in the test fire from the outside wall of the combustion chamber. These were collected after a 1 second burst and a 2 second burst of the thruster. This test data was collected after the heater was started up to 250 °C, while the analysis data starts from the storage temperature.

Table 12. Comparison of Test Fire Data and Thermal Analysis Model.

Time of Burn	Test Fire Data	Analysis Data
1 second	611K	495K
2 second	624K	703K

Figure 51 shows the model that was used to collect the data to compare against the test data. Due to the fact that this model was made as a complete vacuum, it would make sense for it to provide more conservative data once the thruster is operating.

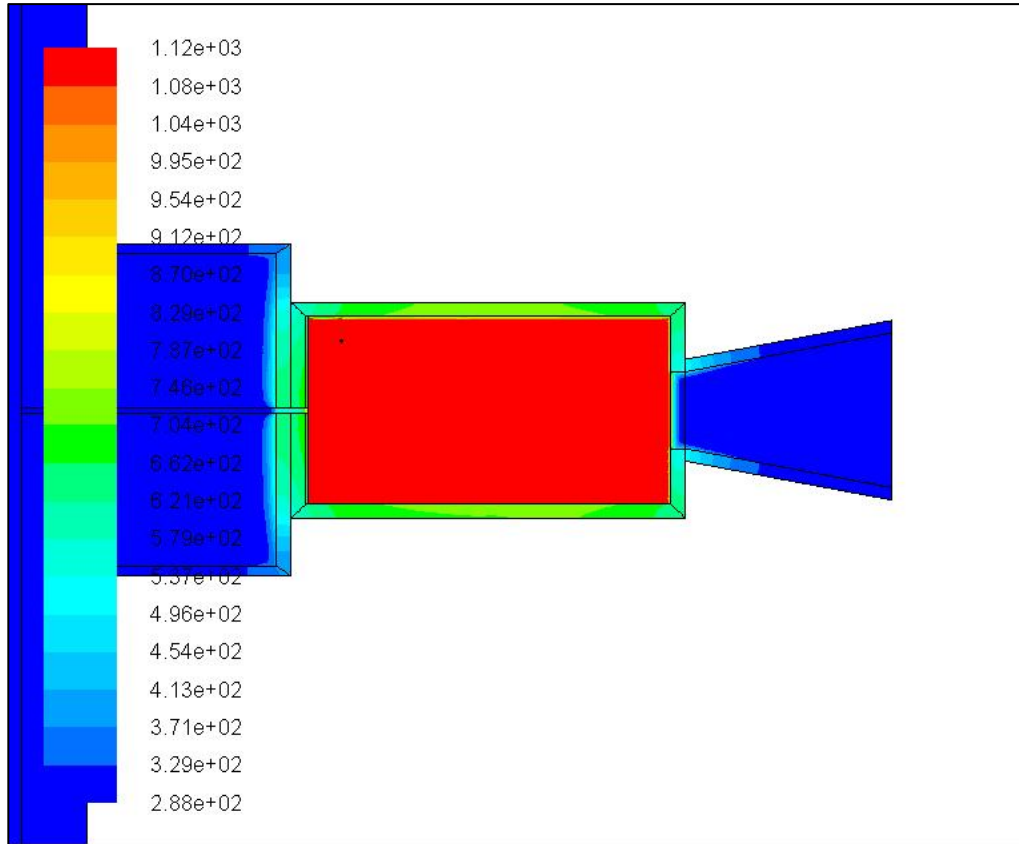


Figure 51. Model Representing the Hot Fire Test after 2 seconds of Burn Time.

7 – Conclusion

The thermal analysis of the hydrazine monopropellant micropropulsion system has produced promising results. It was determined that a solid stainless steel barrier would allow for a large amount of heat transfer if placed in a thermally extreme environment. While the burns were still possible with these conditions, the propellant temperature would need to be monitored more closely. This led to the conclusion that in order to help minimize possibilities for mission failure, there should be a hollow cavity within the design of the system. However, this still leaves the option of operating the thruster with a duty cycle that includes shorter bursts of thrust followed by a period of time with no burn. This duty cycle would be determined based on the external conditions present at the time of the burn.

Once this hollow section was added to the design, further thermal analysis and correction of boundary conditions were made. This allowed for the model to better represent the actual environment that would be present for the spacecraft while in low Earth orbit. The system could now take into account the low conductivity of the environment in space, as well as the potential heat source that would come from the radiation effects on the spacecraft.

The results from this setup proved that the heat from the combustion chamber was no longer impacting the heat of the propellant tank. The system was now primarily affected by the input of heat from radiation onto the walls of the spacecraft. Due to the fact that this analysis was done considering worst-case radiation onto a conservative heat transfer model, this analysis is more damaging than what the system would actually be exposed to in flight.

The amount of external heat that is in contact with the system has a much higher impact on the changing temperature of the propellant than the configuration of the barrier. This indicates that if propellant temperatures lower than 200°C are needed, finding ways to reduce the radiation heat input should be a higher priority than trying to change the system.

However, even if this was the heat of radiation that was impacting the walls, there are many proven solutions to this problem. These solutions can include covering the surface of the spacecraft in an outer shell or coating, making the tank out of a material that has lower thermal conductivity, or even just including a layer of insulating material around the interior or exterior of the tank as a thermal standoff. The use of any sort of thermal insulator would be enough to decrease the impacts of the environmental heat on the system.

Unfortunately, there were some key assumptions that had to be made in this analysis. However, the results proved to be very strong to demonstrate that the low thermal conduction of the hollow barrier, or the insulating material alumina silicate, makes this system extremely successful in creating a thermal standoff. It also dramatically decreases the amount of heat that is transferred from the combustion chamber into the propellant tank. While there is still further testing and analysis that should be performed on this system in the future, these results produce a fundamental idea of the impact of the heat of a reaction on a small system. These results create the confidence that the hollow thermal standoff will serve as intended and protect the CubeSat from experiencing auto-ignition while in flight in any standard low Earth orbit environment.

7.1 – Future Work

7.1.1 – Hot-fire Testing of the System

Further development and validation would be achieved through conducting minimal hot-fire tests of this system. At this time, the actual thermal data for this design is very limited and allows for less certainty of accurate results. Having more data points at different times of the burn and on numerous points across the thruster would allow for basic validation of these results.

7.1.2 – Model the System through another Thermal Analysis Program

Due to technical issues on a lot of the computers throughout the engineering departments, there was not full access to the thermal programs that would have been preferred. This meant that the only models could be done in ANSYS ICEM and ANSYS FLUENT. These programs were not specifically meant for a spacecraft application, and therefore do not have the capabilities that are available on other programs. This means that creative solutions needed to be found to model the environment and part of the system.

If no further hot-fire tests of the system can be completed, it would be recommended to run a parallel analysis with the MSC Software. The use of MSC Patran and MSC Sinda will provide further validation of the results, while also further encompassing some of the boundary conditions needed for this problem.

Bibliography

1. The CubeSat Program, Cal Poly SLO. CubeSat Design Specification (CDS) Rev. 12. *Cubesat Web site*. [Online] August 1, 2009. [Cited: April 29, 2013.]
http://www.cubesat.org/images/developers/cds_rev12.pdf.
2. Mueller, Juergen, Hofer, Richard and Ziemer, John. SURVEY OF PROPULSION TECHNOLOGIES APPLICABLE TO CUBESATS. *NASA JPL Web site*. [Online] [Cited: November 26, 2012.] <http://trs-new.jpl.nasa.gov/dspace/bitstream/2014/41627/1/10-1646.pdf>.
3. Bidy, Chris. Presentations- Developers Workshop 2009. *CubeSat Web site*. [Online] 2009.
http://www.cubesat.org/images/cubesat/presentations/DevelopersWorkshop2009/1_New_Tech_1/6_Biddy-Monopropellant_Propulsion.pdf.
4. AK Steel Corporation. Product Data Sheet- 316 Stainless Steel. *AK Steel Corporation Web site*. [Online] 2007.
http://www.aksteel.com/pdf/markets_products/stainless/austenitic/316_316L_Data_Sheet.pdf.
5. Aerospace Specifications Metals Inc. . Aluminum 2024 Data Sheet. *ASM Web site*. [Online]
<http://asm.matweb.com/search/SpecificMaterial.asp?bassnum=MA2024T4>.
6. Aluminum 6061-T6 Data Sheet. *ASM Web site*. [Online]
<http://asm.matweb.com/search/SpecificMaterial.asp?bassnum=MA6061t6>.
7. Artemis Society International. All About Hydrazine. *The Artemis Project*. [Online] September 1999. <http://www.asi.org/adb/04/03/09/hydrazine-info.html>.

8. Schmitz, Bruce W. and Wilson, Walter W. Long-Life Monopropellant Hydrazine Engine Development Program . *Defense Technical Information Center*. [Online] September 1971. <http://www.dtic.mil/dtic/tr/fulltext/u2/731287.pdf>.
9. Han, Dong In, Han, Cho Young and Shin, Hyun Dong. Empirical and Computational Performance Prediction for Monopropellant Hydrazine Thruster Employed for Satellite. *AIAA Archives Web site*. [Online] June 14, 2009. <http://arc.aiaa.org/doi/pdf/10.2514/1.43739>.
10. ANSYS, Inc. . Heat Transfer Theory. *Fluent Theory Guide*. [Online] January 23, 2009. <http://www.sharcnet.ca/Software/Fluent12/html/th/node107.htm>.
11. ANSYS, Inc. Heat Transfer Modeling Lecture. *Introduction to ANSYS FLUENT*. [Online] December 2010. http://www.ssadeghi.ir/images/docs/ssadeghi.ir_heat_transfer_modeling_lecture.pdf.
12. ANSYS, Inc. . Solving a Conjugate Heat Transfer Problem using ANSYS FLUENT. *ANSYS Web site*. [Online] February 14, 2011. <http://minortfugm.files.wordpress.com/2013/02/05-conjugate-heat-transfer.pdf>.
13. Cengel, Yunus A. *Heat and Mass Transfer- A Pratical Approach*. New York : McGraw-Hill Companies, Inc. , 2007.
14. NASA GRC. Estimating the Temperature of a Flat Plate in Low Earth Orbit. *Glenn Learning Technologies Project (LTP)*. [Online] December 2008. http://www.grc.nasa.gov/WWW/k-12/Numbers/Math/Mathematical_Thinking/estimating_the_temperature.htm.

15. Kopp, Greg and Lean, Judith L. A New Lower Value of Total Solar Irradiance: Evidence and Climate Significance. *Wiley Online Library*. [Online] January 14, 2011. <http://onlinelibrary.wiley.com/doi/10.1029/2010GL045777/pdf>.
16. Friedel, Jonas and McKibbin, Sean. Thermal Analysis of the CubeSat CP3 Satellite. *Cal Poly Digital Commons*. [Online] June 7, 2011. <http://digitalcommons.calpoly.edu/cgi/viewcontent.cgi?article=1054&context=aerospace>.
17. Labs, Shawn. Propulsion Subsystem Thermal Modeling for the FalconSat-5 Microspacecraft. *Undergraduate Research Journal at UCCS*. July 2009, Vol. 2.2.
18. Schmuland, Derek T., Masse, Robert K. and Sota, Charles G. Aerojet- Documents. *Aerojet Rocketdyne*. [Online] July 2011. <http://www.rocket.com/files/aerojet/documents/CubeSat/SSC11-X-4.pdf>.
19. Bidy, Chris and Svitek, Tomas. Stellar Exploration, Inc.- Papers. *Stellar Exploration, Inc. Web site*. [Online] July 2009. <ftp://apollo.ssl.berkeley.edu/pub/cinema/02.%20Systems/2.%20Studies/2.%20Propulsion/1U%20monopropellant.pdf>.
20. Zircar Ceramics. Alumina Silicate Insulation Type AXL & AXHTM. *Zircar Ceramics Web site*. [Online] 2011. <http://www.zircarceramics.com/pages/rigidmaterials/specs/axl.htm>.

APPENDIX A- Full Table of Result Values

Table 13. Complete Thermal Analysis Results from 2-D Models.

Barrier Material	Time of Burn	Maximum Propellant Temp. (Sun)	Maximum Propellant Temp. (Dark)	Maximum Propellant Temp. (Mid)
Stainless Steel	1 sec	361.09K	278.08K	287.35K
Stainless Steel	2 sec	393.23K	n/a	n/a
Stainless Steel	3 sec	398.14K	n/a	n/a
Stainless Steel	4 sec	398.00K	n/a	n/a
Stainless Steel	5 sec	397.83K	223.40K	284.31K
Stainless Steel	12 sec	404.43K	171.19K	286.17K
Stainless Steel	20 sec	408.35K	151.21K	287.41K
Stainless Steel	30 sec	408.99K	142.87K	287.70K
Stainless Steel	40 sec	409.12K	139.96K	287.74K
Stainless Steel	43 sec	409.14K	139.48K	287.74K
Stainless Steel	50 sec	n/a	n/a	287.74K
Barrier Material	Time of Burn	Maximum Propellant Temp. (Sun)	Maximum Propellant Temp. (Dark)	Maximum Propellant Temp. (Mid)
SS Wall/Air Barr	1 sec	361.05K	278.21K	287.28K
SS Wall/Air Barr	2 sec	393.21K	n/a	n/a
SS Wall/Air Barr	3 sec	398.12K	n/a	n/a
SS Wall/Air Barr	4 sec	397.99K	n/a	n/a
SS Wall/Air Barr	5 sec	397.83K	225.42K	282.71K
SS Wall/Air Barr	12 sec	397.89K	168.51K	277.78K
SS Wall/Air Barr	20 sec	397.92K	143.60K	275.62K
SS Wall/Air Barr	30 sec	397.94K	131.79K	274.61K
SS Wall/Air Barr	40 sec	397.95K	127.21K	274.22K
SS Wall/Air Barr	43 sec	397.95K	126.42K	274.15K
SS Wall/Air Barr	50 sec	397.95K	n/a	274.03K

Barrier Material	Time of Burn	Maximum Propellant Temp. (Sun)	Maximum Propellant Temp. (Dark)	Maximum Propellant Temp. (Mid)
SS Wall/AlSi Barr	1 sec	361.05K	278.34K	287.31K
SS Wall/AlSi Barr	2 sec	393.21K	n/a	n/a
SS Wall/AlSi Barr	3 sec	398.13K	n/a	n/a
SS Wall/AlSi Barr	4 sec	397.95K	n/a	n/a
SS Wall/AlSi Barr	5 sec	397.83K	226.35K	282.79K
SS Wall/AlSi Barr	12 sec	397.89K	173.09K	278.18K
SS Wall/AlSi Barr	20 sec	397.92K	147.95K	276.02K
SS Wall/AlSi Barr	30 sec	397.94K	135.42K	274.90K
SS Wall/AlSi Barr	40 sec	397.95K	130.17K	274.48K
SS Wall/AlSi Barr	43 sec	397.95K	129.23K	274.40K
SS Wall/AlSi Barr	50 sec	n/a	n/a	274.24K
Barrier Material	Time of Burn	Maximum Propellant Temp. (Sun)	Maximum Propellant Temp. (Dark)	Maximum Propellant Temp. (Mid)
Barrier with AlSi&Air	1 sec	301.30K	n/a	n/a
Barrier with AlSi&Air	5 sec	334.79K	n/a	n/a
Barrier with AlSi&Air	12 sec	355.60K	n/a	n/a
Barrier with AlSi&Air	20 sec	364.70K	n/a	n/a
Barrier with AlSi&Air	30 sec	370.17K	n/a	n/a
Barrier with AlSi&Air	40 sec	373.34K	n/a	n/a
Barrier with AlSi&Air	43 sec	374.06K	n/a	n/a
Barrier with AlSi&Air	50 sec	375.49K	n/a	n/a
Barrier Material	Time of Burn	Maximum Propellant Temp. (Sun)	Maximum Propellant Temp. (Dark)	Maximum Propellant Temp. (Mid)
Alumina Silicate	1 sec	288.29K	n/a	n/a
Alumina Silicate	5 sec	288.84K	n/a	n/a
Alumina Silicate	12 sec	289.56K	n/a	n/a
Alumina Silicate	20 sec	290.20K	n/a	n/a
Alumina Silicate	30 sec	290.86K	n/a	n/a
Alumina Silicate	40 sec	291.43K	n/a	n/a
Alumina Silicate	43 sec	291.59K	n/a	n/a
Alumina Silicate	50 sec	291.93K	n/a	n/a

APPENDIX B- ANSYS Input Values

Genera 1			
	<i>Solver</i>		
		Type	Pressure-Based
		Time	Transient
		Velocity Formulation	Absolute
		2D Space	Planar
	<i>Gravity</i>		
		On/Off	On
	<i>Gravitational Acceleration (m/s²)</i>		
		x-direction	0
		y-direction	-9
Models (Any models not indicated in table should be "Off")			
	<i>Energy</i>	On	
	<i>Viscous</i>	Laminar	
Materials			
	<i>Material</i>	<i>Hydrazine</i>	
		Density	1011 kg/m ³
		Specific Heat	polynomial
		Thermal Conductivity	0.0454 W/m-K
		Viscosity	0.0000172 kg/m-s
	<i>Material</i>	<i>Stainless Steel 316</i>	
		Density	7990 kg/m ³
		Specific Heat	502 J/kg-K
		Thermal Conductivity	16.2 W/m-K
	<i>Material</i>	<i>Aluminum2024</i>	
		Density	2780 kg/m ³
		Specific Heat	875 J/kg-K
		Thermal Conductivity	121 W/m-K
	<i>Material</i>	<i>Space Environment</i>	

		Density	1.225 kg/m ³
		Specific Heat	1006.43 J/kg-K
		Thermal Conductivity	0.0001 W/m-K
		Viscosity	1.7894e-05 kg/m-s
	<i>Material</i>	<i>Alumina Silicate AXHTM</i>	
		Density	2600 kg/m ³
		Specific Heat	1050 J/kg-K
		Thermal Conductivity	0.14 W/m-K
Operating Conditions			
		Operating Pressure	551,580Pa
		Gravity	9.5 m/s ²
Mesh Interfaces			
	<i>Iterface</i>	Interior wall of combustion chamber	
		<i>ccwall_int</i>	<i>heat_ccwall2,</i> <i>prop_ccwall_int</i>
	<i>Iterface</i>	Pipe	
		<i>pipe</i>	<i>prop_barr, prop_barrwall,</i> <i>prop_cc, prop_ccwall,</i> <i>prop_tankwall</i>
	<i>Iterface</i>	Inlet into combustion chamber	
		<i>cc_inlet</i>	<i>pipe_outlet, prop_ccwall2</i>
	<i>Iterface</i>	Outlet from combustion chamber	
		<i>cc_outlet</i>	<i>ccwall_int2, nozzle_inlet</i>
	<i>Iterface</i>	Interface between barrier and combustion chamber	
		<i>interface_cb</i>	<i>barr_ccwall</i>
	<i>Iterface</i>	Interface between tank interior and tank wall	
		<i>interface_tt</i>	<i>pipe_inlet, tank_int2</i>
	<i>Iterface</i>	Interface between barrier and tank	
		<i>interface_tb</i>	<i>barr_tank, barr_tankwall</i>
	<i>Iterface</i>	Interface between combustion chamber and nozzle	
		<i>interface_cn</i>	<i>nozz_split</i>
Reference Values			
	<i>Compute from</i>	<i>prop_in_cc</i>	

	<i>Reference Zone</i>	<i>prop_in_tank</i>	
Solution Methods			
	<i>Pressure-Velocity Coupling</i>		
		Scheme	PISO
	<i>Spatial Discretization</i>		
		Gradient	Least Squares Cell Based
		Pressure	Second Order
		Momentum	Second Order Upwind
		Energy	Second Order Upwind
	<i>Transient Formulation</i>		Second Order Implicit
	<i>Non-Iterative Time Advancement</i>		On
Solution Controls			
	<i>Non-Iterative Solver Relaxation Factors</i>		
		Pressure	1
		Momentum	1
		Energy	0.9
Solution Initialization			
	<i>Reference Frame</i>		Relative to Cell Zone
	<i>Initial Values</i>		
		Gauge Pressure	0 Pa
		x-Velocity	0 m/s
		y-Velocity	0 m/s
		Temperature	288.15 K

APPENDIX C- Stellar Exploration, Inc. Propulsion Module

Table 14. Spacecraft Specifications.

Spacecraft Mass (kg)	50
Required Total Delta-V (m/s)	15
Required Min Propellant Mass (g)	400
Assumed Isp (s)	210

Table 15. Thruster Specifications.

Blow Down Ratio	5
Initial Propellant Volume (ml)	203
Initial mass of propellant (g)	205
Initial Gas Volume (ml)	50
Initial Gas Pressure (kPa)	1200

$$\text{Lohms} = KV/I*(H/S)^{1/2}$$

- K= constant for unit correction
- V= viscosity correction factor
- S= specific gravity
- H= differential pressure (psi)
- I= flow rate (ml/sec)

Atomizer

Lohms	35000
S	0.797
V	0.86
K	75700

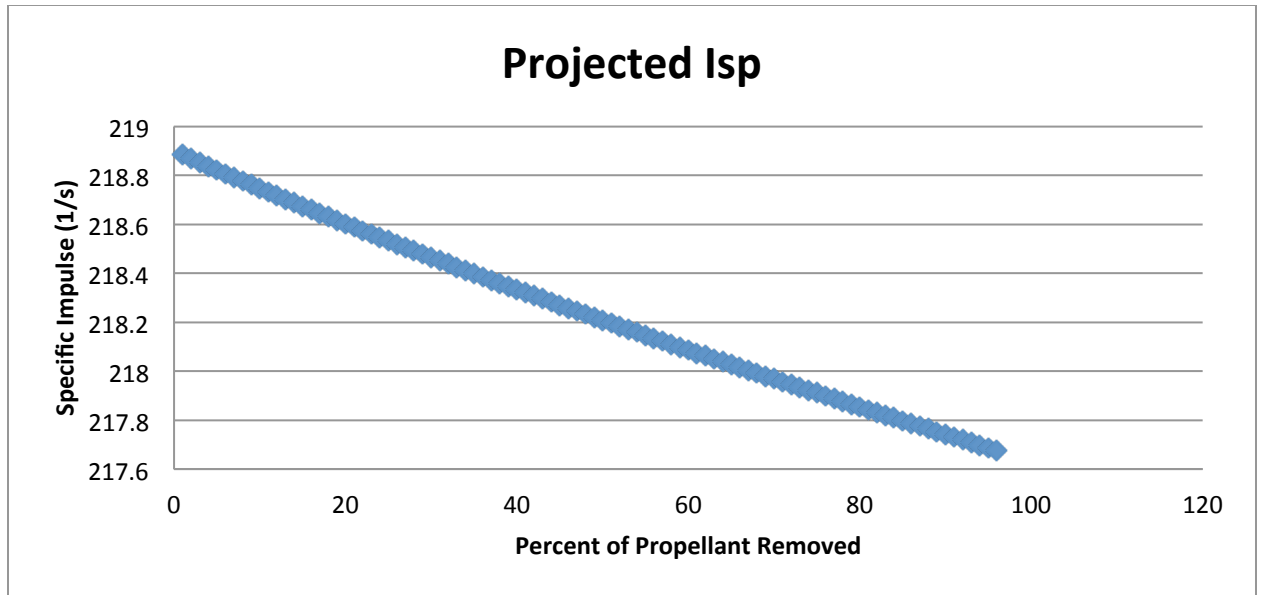


Figure 52. Projected Isp.

Table 16. Projected Values for Thruster Performance.

Time (sec)	Wp(t) N	mp (t) removed (g)	Gas Volume (ml)	Tank Pressure (kPa)	Blow Down Ratio	Isp (s)	Thrust (N)
1	2.007	0.46	50.47	1188.89	1.01	218.89	0.99
2	2.002	0.46	50.93	1178.03	1.02	218.88	0.99
3	1.997	0.46	51.40	1167.42	1.03	218.87	0.98
4	1.993	0.46	51.86	1157.04	1.04	218.86	0.98
5	1.989	0.45	52.32	1146.89	1.05	218.85	0.98
6	1.984	0.45	52.77	1136.96	1.06	218.84	0.97
7	1.980	0.45	53.23	1127.25	1.06	218.83	0.97
8	1.975	0.45	53.68	1117.73	1.07	218.82	0.96
9	1.971	0.45	54.13	1108.42	1.08	218.81	0.96
10	1.967	0.44	54.58	1099.30	1.09	218.80	0.95
11	1.962	0.44	55.03	1090.36	1.10	218.79	0.95
12	1.958	0.44	55.47	1081.61	1.11	218.7	0.95

						8	
13	1.954	0.44	55.92	1073.03	1.12	218.77	0.94
14	1.949	0.44	56.36	1064.61	1.13	218.76	0.94
15	1.945	0.44	56.80	1056.36	1.14	218.75	0.94
16	1.941	0.43	57.24	1048.27	1.14	218.74	0.93
17	1.937	0.43	57.67	1040.33	1.15	218.73	0.93
18	1.932	0.43	58.11	1032.54	1.16	218.72	0.92
19	1.928	0.43	58.54	1024.90	1.17	218.71	0.92
20	1.924	0.43	58.97	1017.39	1.18	218.70	0.92
21	1.920	0.43	59.40	1010.02	1.19	218.69	0.91
22	1.916	0.42	59.83	1002.78	1.20	218.68	0.91
23	1.911	0.42	60.26	995.67	1.21	218.67	0.91
24	1.907	0.42	60.69	988.69	1.21	218.66	0.90
25	1.903	0.42	61.11	981.83	1.22	218.66	0.90
26	1.899	0.42	61.53	975.08	1.23	218.65	0.90
27	1.895	0.42	61.95	968.45	1.24	218.64	0.89
28	1.891	0.42	62.37	961.93	1.25	218.63	0.89
29	1.887	0.41	62.79	955.52	1.26	218.62	0.89
30	1.883	0.41	63.21	949.22	1.26	218.61	0.89
31	1.879	0.41	63.63	943.02	1.27	218.60	0.88
32	1.875	0.41	64.04	936.92	1.28	218.59	0.88
33	1.871	0.41	64.45	930.92	1.29	218.58	0.88
34	1.867	0.41	64.86	925.01	1.30	218.5	0.87

						7	
35	1.863	0.41	65.27	919.20	1.31	218.56	0.87
36	1.859	0.40	65.68	913.47	1.31	218.55	0.87
37	1.855	0.40	66.09	907.84	1.32	218.55	0.87
38	1.851	0.40	66.50	902.29	1.33	218.54	0.86
39	1.847	0.40	66.90	896.82	1.34	218.53	0.86
40	1.843	0.40	67.31	891.44	1.35	218.52	0.86
41	1.839	0.40	67.71	886.14	1.35	218.51	0.85
42	1.835	0.40	68.11	880.91	1.36	218.50	0.85
43	1.831	0.40	68.51	875.76	1.37	218.49	0.85
44	1.827	0.40	68.91	870.69	1.38	218.48	0.85
45	1.824	0.39	69.31	865.69	1.39	218.48	0.84
46	1.820	0.39	69.71	860.76	1.39	218.47	0.84
47	1.816	0.39	70.10	855.90	1.40	218.46	0.84
48	1.812	0.39	70.50	851.11	1.41	218.45	0.84
49	1.808	0.39	70.89	846.38	1.42	218.44	0.84
50	1.804	0.39	71.28	841.72	1.43	218.43	0.83
51	1.801	0.39	71.67	837.13	1.43	218.42	0.83
52	1.797	0.39	72.06	832.59	1.44	218.41	0.83
53	1.793	0.39	72.45	828.12	1.45	218.41	0.83
54	1.789	0.38	72.84	823.70	1.46	218.40	0.82
55	1.785	0.38	73.23	819.35	1.46	218.39	0.82
56	1.782	0.38	73.61	815.05	1.47	218.3	0.82

						8	
57	1.778	0.38	74.00	810.81	1.48	218.37	0.82
58	1.774	0.38	74.38	806.62	1.49	218.36	0.81
59	1.770	0.38	74.77	802.49	1.50	218.36	0.81
60	1.767	0.38	75.15	798.41	1.50	218.35	0.81
61	1.763	0.38	75.53	794.38	1.51	218.34	0.81
62	1.759	0.38	75.91	790.40	1.52	218.33	0.81
63	1.756	0.38	76.29	786.47	1.53	218.32	0.80
64	1.752	0.37	76.67	782.59	1.53	218.31	0.80
65	1.748	0.37	77.05	778.76	1.54	218.30	0.80
66	1.745	0.37	77.42	774.97	1.55	218.30	0.80
67	1.741	0.37	77.80	771.23	1.56	218.29	0.80
68	1.737	0.37	78.17	767.53	1.56	218.28	0.79
69	1.734	0.37	78.55	763.88	1.57	218.27	0.79
70	1.730	0.37	78.92	760.27	1.58	218.26	0.79
71	1.727	0.37	79.29	756.70	1.59	218.26	0.79
72	1.723	0.37	79.66	753.18	1.59	218.25	0.79
73	1.719	0.37	80.03	749.70	1.60	218.24	0.78
74	1.716	0.37	80.40	746.25	1.61	218.23	0.78
75	1.712	0.36	80.77	742.85	1.62	218.22	0.78
76	1.709	0.36	81.14	739.48	1.62	218.21	0.78
77	1.705	0.36	81.50	736.15	1.63	218.21	0.78
78	1.701	0.36	81.87	732.86	1.64	218.2	0.78

						0	
79	1.698	0.36	82.24	729.61	1.64	218.19	0.77
80	1.694	0.36	82.60	726.39	1.65	218.18	0.77
81	1.691	0.36	82.96	723.20	1.66	218.17	0.77
82	1.687	0.36	83.33	720.05	1.67	218.17	0.77
83	1.684	0.36	83.69	716.94	1.67	218.16	0.77
84	1.680	0.36	84.05	713.86	1.68	218.15	0.77
85	1.677	0.36	84.41	710.81	1.69	218.14	0.76
86	1.673	0.36	84.77	707.79	1.70	218.14	0.76
87	1.670	0.36	85.13	704.81	1.70	218.13	0.76
88	1.666	0.35	85.49	701.86	1.71	218.12	0.76
89	1.663	0.35	85.84	698.94	1.72	218.11	0.76
90	1.659	0.35	86.20	696.04	1.72	218.10	0.76
91	1.656	0.35	86.56	693.18	1.73	218.10	0.75
92	1.653	0.35	86.91	690.35	1.74	218.09	0.75
93	1.649	0.35	87.27	687.55	1.75	218.08	0.75
94	1.646	0.35	87.62	684.77	1.75	218.07	0.75
95	1.642	0.35	87.97	682.02	1.76	218.06	0.75
96	1.639	0.35	88.33	679.30	1.77	218.06	0.75
97	1.635	0.35	88.68	676.61	1.77	218.05	0.74
98	1.632	0.35	89.03	673.94	1.78	218.04	0.74
99	1.629	0.35	89.38	671.30	1.79	218.03	0.74
100	1.625	0.35	89.73	668.69	1.79	218.0	0.74

						3	
101	1.622	0.35	90.08	666.10	1.80	218.0 2	0.74
102	1.618	0.34	90.43	663.53	1.81	218.0 1	0.74
103	1.615	0.34	90.77	660.99	1.82	218.0 0	0.74
104	1.612	0.34	91.12	658.47	1.82	218.0 0	0.73
105	1.608	0.34	91.47	655.98	1.83	217.9 9	0.73
106	1.605	0.34	91.81	653.51	1.84	217.9 8	0.73
107	1.602	0.34	92.16	651.07	1.84	217.9 7	0.73
108	1.598	0.34	92.50	648.65	1.85	217.9 6	0.73
109	1.595	0.34	92.84	646.24	1.86	217.9 6	0.73
110	1.592	0.34	93.19	643.87	1.86	217.9 5	0.73
111	1.588	0.34	93.53	641.51	1.87	217.9 4	0.72
112	1.585	0.34	93.87	639.17	1.88	217.9 3	0.72
113	1.582	0.34	94.21	636.86	1.88	217.9 3	0.72
114	1.578	0.34	94.55	634.57	1.89	217.9 2	0.72
115	1.575	0.34	94.89	632.30	1.90	217.9 1	0.72
116	1.572	0.34	95.23	630.04	1.90	217.9 0	0.72
117	1.568	0.34	95.57	627.81	1.91	217.9 0	0.72
118	1.565	0.33	95.91	625.60	1.92	217.8 9	0.72
119	1.562	0.33	96.25	623.40	1.92	217.8 8	0.71
120	1.559	0.33	96.58	621.23	1.93	217.8 8	0.71
121	1.555	0.33	96.92	619.08	1.94	217.8 7	0.71
122	1.552	0.33	97.25	616.94	1.95	217.8	0.71

						6	
123	1.549	0.33	97.59	614.82	1.95	217.85	0.71
124	1.546	0.33	97.92	612.72	1.96	217.85	0.71
125	1.542	0.33	98.26	610.64	1.97	217.84	0.71
126	1.539	0.33	98.59	608.57	1.97	217.83	0.71
127	1.536	0.33	98.92	606.53	1.98	217.82	0.70
128	1.533	0.33	99.26	604.50	1.99	217.82	0.70
129	1.529	0.33	99.59	602.48	1.99	217.81	0.70
130	1.526	0.33	99.92	600.49	2.00	217.80	0.70
131	1.523	0.33	100.25	598.51	2.00	217.79	0.70
132	1.520	0.33	100.58	596.54	2.01	217.79	0.70
133	1.517	0.33	100.91	594.59	2.02	217.78	0.70
134	1.513	0.33	101.24	592.66	2.02	217.77	0.70
135	1.510	0.33	101.57	590.75	2.03	217.77	0.69
136	1.507	0.32	101.89	588.84	2.04	217.76	0.69
137	1.504	0.32	102.22	586.96	2.04	217.75	0.69
138	1.501	0.32	102.55	585.09	2.05	217.74	0.69
139	1.497	0.32	102.88	583.23	2.06	217.74	0.69
140	1.494	0.32	103.20	581.39	2.06	217.73	0.69
141	1.491	0.32	103.53	579.56	2.07	217.72	0.69
142	1.488	0.32	103.85	577.75	2.08	217.72	0.69
143	1.485	0.32	104.18	575.95	2.08	217.71	0.69
144	1.482	0.32	104.50	574.17	2.09	217.7	0.68

						0	
145	1.479	0.32	104.82	572.40	2.10	217.69	0.68
146	1.475	0.32	105.14	570.64	2.10	217.69	0.68
147	1.472	0.32	105.47	568.90	2.11	217.68	0.68
148	1.469	0.32	105.79	567.17	2.12	217.67	0.68
149	1.466	0.32	106.11	565.45	2.12	217.67	0.68
150	1.463	0.32	106.43	563.75	2.13	217.66	0.68
151	1.460	0.32	106.75	562.05	2.14	217.65	0.68
152	1.457	0.32	107.07	560.38	2.14	217.64	0.68
153	1.454	0.32	107.39	558.71	2.15	217.64	0.68
154	1.451	0.32	107.71	557.05	2.15	217.63	0.67
155	1.447	0.32	108.03	555.41	2.16	217.62	0.67
156	1.444	0.31	108.35	553.78	2.17	217.62	0.67
157	1.441	0.31	108.66	552.16	2.17	217.61	0.67
158	1.438	0.31	108.98	550.56	2.18	217.60	0.67
159	1.435	0.31	109.30	548.96	2.19	217.60	0.67
160	1.432	0.31	109.61	547.38	2.19	217.59	0.67
161	1.429	0.31	109.93	545.81	2.20	217.58	0.67
162	1.426	0.31	110.24	544.25	2.20	217.57	0.67
163	1.423	0.31	110.56	542.70	2.21	217.57	0.67
164	1.420	0.31	110.87	541.16	2.22	217.56	0.66
165	1.417	0.31	111.19	539.63	2.22	217.55	0.66
166	1.414	0.31	111.50	538.12	2.23	217.5	0.66

						5	
167	1.411	0.31	111.81	536.61	2.24	217.54	0.66
168	1.408	0.31	112.13	535.12	2.24	217.53	0.66
169	1.405	0.31	112.44	533.63	2.25	217.53	0.66
170	1.402	0.31	112.75	532.16	2.25	217.52	0.66
171	1.399	0.31	113.06	530.69	2.26	217.51	0.66
172	1.396	0.31	113.37	529.24	2.27	217.51	0.66
173	1.393	0.31	113.68	527.79	2.27	217.50	0.66
174	1.390	0.31	113.99	526.36	2.28	217.49	0.65
175	1.387	0.31	114.30	524.93	2.29	217.49	0.65
176	1.384	0.31	114.61	523.52	2.29	217.48	0.65
177	1.381	0.31	114.92	522.11	2.30	217.47	0.65
178	1.378	0.31	115.23	520.71	2.30	217.47	0.65
179	1.375	0.30	115.53	519.33	2.31	217.46	0.65
180	1.372	0.30	115.84	517.95	2.32	217.45	0.65
181	1.369	0.30	116.15	516.58	2.32	217.44	0.65
182	1.366	0.30	116.46	515.22	2.33	217.44	0.65
183	1.363	0.30	116.76	513.87	2.34	217.43	0.65
184	1.360	0.30	117.07	512.52	2.34	217.42	0.65
185	1.357	0.30	117.37	511.19	2.35	217.42	0.64
186	1.354	0.30	117.68	509.87	2.35	217.41	0.64
187	1.351	0.30	117.98	508.55	2.36	217.40	0.64
188	1.348	0.30	118.29	507.24	2.37	217.4	0.64

						0	
189	1.345	0.30	118.59	505.94	2.37	217.39	0.64
190	1.342	0.30	118.89	504.65	2.38	217.38	0.64
191	1.339	0.30	119.20	503.37	2.38	217.38	0.64
192	1.336	0.30	119.50	502.09	2.39	217.37	0.64
193	1.333	0.30	119.80	500.83	2.40	217.36	0.64
194	1.330	0.30	120.10	499.57	2.40	217.36	0.64
195	1.327	0.30	120.41	498.32	2.41	217.35	0.64
196	1.324	0.30	120.71	497.07	2.41	217.34	0.64
197	1.321	0.30	121.01	495.84	2.42	217.34	0.63
198	1.318	0.30	121.31	494.61	2.43	217.33	0.63
199	1.316	0.30	121.61	493.39	2.43	217.32	0.63
200	1.313	0.30	121.91	492.18	2.44	217.32	0.63
201	1.310	0.30	122.21	490.97	2.44	217.31	0.63
202	1.307	0.30	122.51	489.77	2.45	217.30	0.63
203	1.304	0.30	122.80	488.58	2.46	217.30	0.63
204	1.301	0.30	123.10	487.40	2.46	217.29	0.63
205	1.298	0.29	123.40	486.22	2.47	217.29	0.63
206	1.295	0.29	123.70	485.05	2.47	217.28	0.63
207	1.292	0.29	124.00	483.89	2.48	217.27	0.63
208	1.289	0.29	124.29	482.74	2.49	217.27	0.63
209	1.287	0.29	124.59	481.59	2.49	217.26	0.63
210	1.284	0.29	124.88	480.44	2.50	217.2	0.62

						5	
211	1.281	0.29	125.18	479.31	2.50	217.2 5	0.62
212	1.278	0.29	125.48	478.18	2.51	217.2 4	0.62
213	1.275	0.29	125.77	477.06	2.52	217.2 3	0.62
214	1.272	0.29	126.06	475.95	2.52	217.2 3	0.62
215	1.269	0.29	126.36	474.84	2.53	217.2 2	0.62
216	1.267	0.29	126.65	473.73	2.53	217.2 1	0.62
217	1.264	0.29	126.95	472.64	2.54	217.2 1	0.62
218	1.261	0.29	127.24	471.55	2.54	217.2 0	0.62
219	1.258	0.29	127.53	470.47	2.55	217.1 9	0.62
220	1.255	0.29	127.83	469.39	2.56	217.1 9	0.62
221	1.252	0.29	128.12	468.32	2.56	217.1 8	0.62
222	1.249	0.29	128.41	467.25	2.57	217.1 7	0.62
223	1.247	0.29	128.70	466.19	2.57	217.1 7	0.62
224	1.244	0.29	128.99	465.14	2.58	217.1 6	0.61
225	1.241	0.29	129.28	464.10	2.59	217.1 6	0.61
226	1.238	0.29	129.57	463.05	2.59	217.1 5	0.61
227	1.235	0.29	129.86	462.02	2.60	217.1 4	0.61
228	1.233	0.29	130.15	460.99	2.60	217.1 4	0.61
229	1.230	0.29	130.44	459.97	2.61	217.1 3	0.61
230	1.227	0.29	130.73	458.95	2.61	217.1 2	0.61
231	1.224	0.29	131.02	457.94	2.62	217.1 2	0.61
232	1.221	0.29	131.31	456.93	2.63	217.1	0.61

						1	
233	1.218	0.29	131.60	455.93	2.63	217.10	0.61
234	1.216	0.29	131.89	454.93	2.64	217.10	0.61
235	1.213	0.28	132.18	453.94	2.64	217.09	0.61
236	1.210	0.28	132.46	452.96	2.65	217.09	0.61
237	1.207	0.28	132.75	451.98	2.66	217.08	0.61
238	1.205	0.28	133.04	451.00	2.66	217.07	0.60
239	1.202	0.28	133.32	450.03	2.67	217.07	0.60
240	1.199	0.28	133.61	449.07	2.67	217.06	0.60
241	1.196	0.28	133.90	448.11	2.68	217.05	0.60
242	1.193	0.28	134.18	447.16	2.68	217.05	0.60
243	1.191	0.28	134.47	446.21	2.69	217.04	0.60
244	1.188	0.28	134.75	445.26	2.70	217.04	0.60
245	1.185	0.28	135.04	444.33	2.70	217.03	0.60
246	1.182	0.28	135.32	443.39	2.71	217.02	0.60
247	1.180	0.28	135.60	442.46	2.71	217.02	0.60
248	1.177	0.28	135.89	441.54	2.72	217.01	0.60
249	1.174	0.28	136.17	440.62	2.72	217.00	0.60
250	1.171	0.28	136.45	439.71	2.73	217.00	0.60
251	1.169	0.28	136.74	438.80	2.73	216.99	0.60
252	1.166	0.28	137.02	437.89	2.74	216.99	0.60
253	1.163	0.28	137.30	436.99	2.75	216.98	0.59
254	1.160	0.28	137.58	436.10	2.75	216.9	0.59

						7	
255	1.158	0.28	137.87	435.20	2.76	216.9 7	0.59
256	1.155	0.28	138.15	434.32	2.76	216.9 6	0.59
257	1.152	0.28	138.43	433.44	2.77	216.9 5	0.59
258	1.149	0.28	138.71	432.56	2.77	216.9 5	0.59
259	1.147	0.28	138.99	431.68	2.78	216.9 4	0.59
260	1.144	0.28	139.27	430.82	2.79	216.9 4	0.59
							188.9 5